INSTITUTO POLITÉCNICO DE BRAGANÇA
Escola Superior de Tecnologia e de Gestão

Hemodynamic study in a real intracranial aneurysm: an *in vitro* and *in silico* approach

Andrews Victor Almeida de Souza

Dissertation presented to Escola Superior de Tecnologia e Gestão of Instituto Politécnico de Bragança to obtain the Master Degree in Industrial Engineering

Supervised by:

Professor Doutor João Eduardo Pinto Castro Ribeiro

Professor Mestre Fernando da Silva Araújo

Bragança

July 2020

INSTITUTO POLITÉCNICO DE BRAGANÇA Escola Superior de Tecnologia e de Gestão

CEFET/RJ

Hemodynamic study in a real intracranial aneurysm: an *in vitro* and *in silico* approach

Andrews Victor Almeida de Souza

Dissertation presented to Escola Superior de Tecnologia e Gestão de Bragança in double degree program with Centro Federal de Educação Tecnológica Celso Suckow da Fonseca (CEFET/RJ)- Campus Angra dos Reis to obtain the Master Degree in Industrial Engineering

Supervised by:

Professor Doutor João Eduardo Pinto Castro Ribeiro

Professor Mestre Fernando da Silva Araújo

Bragança

July 2020

Agradecimentos

Primeiramente gostaria de agradecer a Deus, que me deu vida, saúde e força para concluir esse trabalho.

Gostaria de agradecer imensamente ao meu orientador Professor João Ribeiro, por toda a ajuda ao longo desses últimos anos, por todo o valor que reconheceu em mim, por sua orientação conselhos e amizade. Muito obrigado. Agradeço também meu coorientador Professor Fernando Araújo por todo o incentivo ao longo desse trabalho.

Quero também agradecer a toda a equipe de mecânica dos fluidos da Universidade de Extremadura, em especial para meu supervisor de estágio Conrado Ferrera, por toda a sua dedicação em ensinar, a sua ajuda nos ensaios experimentais foi determinante para a conclusão dessa dissertação.

Agora, quero deixar o meu profundo agradecimento aos meus pais, por todo sacrifício que fazem para que isto seja possível, pelo exemplo de vida, educação, carinho, por ter me acompanhado por todos esses anos incentivando nos momentos difíceis e dando todo o suporte necessário.

E agradecer a pessoa mais especial na minha vida, que é aquele me ajuda me apoia em todos os momentos. Sabrina só você sabe o quanto foi difícil a nossa caminhada até aqui, mas, hoje posso dizer que valeu a pena todo o nosso esforço. Tenho muito orgulho de ter uma mulher como você ao meu lado. Te amo!

Resumo

O aneurisma intracraniano (AI) é uma patologia cerebrovascular com altas taxas de mortalidade e morbidade quando se rompe. Sabe-se que alterações na carga hemodinâmica intra-aneurismática exerce um fator significativo no desenvolvimento e ruptura de AI, porém, esses fatores não estão totalmente compreendidos. Nesse sentido, o objetivo principal deste trabalho é o de estudar o comportamento hemodinâmico durante o escoamento de fluidos análogos do sangue no interior de um AI e determinar a sua influência na evolução da patologia. Para tal, foram realizados estudos experimentais e numéricos, utilizando um modelo de AI real obtido por meio de uma angiografia computadorizada.

Na abordagem experimental foi necessário, na fase inicial, desenvolver e fabricar biomodelos a partir de imagens médicas de um aneurisma real. No fabrico dos biomodelos foram utilizadas duas técnicas: a prototipagem rápida e o vazamento por gravidade. Os materiais utilizados para a obtenção dos biomodelos foram de baixo custo. Após a fabricação, os biomodelos foram comparados entre si quanto à sua transparência e estrutura final e verificou-se serem adequados para testes de visualizações do fluxo. Os estudos numéricos foram realizados com recurso ao software Ansys Fluent, utilizando a dinâmica dos fluidos computacional (CFD), através do método dos volumes finitos.

Posteriormente, foram realizados testes de escoamento experimentais e numéricos, utilizando caudais determinados a partir da curva de velocidades do ensaio doppler de um paciente. Os testes experimentais e numéricos, em regime permanente, possibilitaram a visualização do comportamento tridimensional do fluxo no interior do aneurisma, identificando as zonas de vórtices criadas ao longo do ciclo cardíaco. Correlacionando os resultados obtidos nas duas análises, foi possível identificar que as áreas de vórtices são caracterizadas por uma baixa velocidade e com o aumento do caudal os vórtices posicionam-se mais próximos da parede. Essas características apresentadas estão associadas com a ruptura de aneurisma intracraniano. Verificou-se, também, uma boa correlação qualitativa entre os resultados numéricos e experimentais.

Palavras chaves: aneurisma intracraniano; biomodelos; fabricação; hemodinânica, ensaios experimentais, simulação numérica, CFD.

Abstract

Intracranial aneurysm (IA) is a cerebrovascular disease with high rates of mortality and morbidity when it ruptures. It is known that changes in the intra-aneurysmal hemodynamic load play a significant factor in the development and rupture of IA. However, these factors are not fully understood. In this sense, the main objective of this work is to study the hemodynamic behavior during the blood analogues flow inside an AI and to determine its influence on the evolution of this pathology. To this end, experimental and numerical studies were carried out, using a real AI model obtained using computerized angiography.

In the experimental approach, it was necessary, in the initial phase, to develop and manufacture biomodels from medical images of real aneurysms. Two techniques were used to manufacture the biomodels: rapid prototyping and gravity casting. The materials used to obtain the biomodels were of low cost. After manufacture, the biomodels were compared to each other for their transparency and final structure and proved to be suitable for testing flow visualizations. Numerical studies were performed with the aid of the Ansys Fluent software, using computational fluid dynamics (CFD), using the finite volume method.

Subsequently, flow tests were performed experimentally and numerically using flow rates calculated from the velocity curve of a patient's doppler test. The experimental and numerical tests, in steady-state, made it possible to visualize the three-dimensional behavior of the flow inside the aneurysm, identifying the vortex zones created throughout the cardiac cycle. Correlating the results obtained in the two analyzes, it was possible to identify that the areas of vortexes are characterized by low speed and with increasing the fluid flow, the vortexes are positioned closer to the wall. These characteristics are associated with the rupture of an intracranial aneurysm. There was also a good qualitative correlation between numerical and experimental results.

Key words: intracranial aneurysm; biomodels; manufacturing; hemodynamics, experimental tests, numerical simulation, CFD.

Table of Contents

Agradecimentos ..... **ii**

Resumo ..... **iii**

Abstract ..... **iv**

Table of Contents ..... **v**

List of Figures ..... **viii**

List of Tables ..... **xi**

List of Abbreviations and Symbols ..... **xii**

Chapter 1 ..... **1**

Introduction **1**

1.1 Intracranial Aneurysm 3

1.2 Hemodynamic Fundamentals 4

1.2.1 Blood viscosity 5

1.2.2 Reynolds number 6

1.2.3 Blood pressure 7

1.2.4 Wall Shear Stress - WSS 7

1.2.5 Blood flow classification 8

1.3 Types of studies 9

1.3.1 *In vivo* 9

1.3.2 *In sílico* 10

1.3.3 *In vitro* 11

1.4 Motivation and Goals 12

1.5 Structure 13

References 15

Chapter 2 ..... **25**

Characterization of shear strain on PDMS: Numerical and experimental approaches [1] **25**

Abstract 25

2.1 Introduction 26
2.2 Numerical Constitutive Models 27
2.3 Materials and Methods 31
2.3.1 Experimental tests 31
2.3.2 Numerical Simulation 36
2.4 Results and Discussion 38
2.4.1 Experimental 38
2.4.1 Numerical 41
2.4.2 Comparison 43
2.5 Conclusions 45
Chapter 3 50
Manufacturing process of a brain aneurysm bio model in PDMS using rapid prototyping [1] 50
Abstract 50
3.1 Introduction 51
3.2 Manufacturing Process 51
3.3 Rapid Prototyping 53
3.4 *In Vitro* PDMS Biomodel 53
3.5 Conclusions 54
References 55
Chapter 4 57
3D Manufacturing of intracranial aneurysm biomodels for flow visualizations: a low cost fabrication process [1] 57
Abstract 57
4.1 Introduction 58
4.2 Materials and Methods 60
4.2.1 Obtaining the digital model 61
4.2.2 Rapid prototyping of the 3D aneurysm mold 61
4.2.3 Lost wax process and PDMS biomodels 62

4.2.4 Flow visualizations setup and numerical simulations 64
4.3 Results 66
4.3.1 Comparison of geometric structure 66
4.3.2 Comparison of optical channel transparency 68
4.4 Experimental and Numerical Comparison of the Biomodels 70
4.4.1 Experimental procedure 70
4.4.2 Numerical simulation and qualitative comparison with the experimental 70
4.5 Conclusions 72
References 73
Chapter 5 78
Analysis of fluid flow inside an intracranial aneurysm: an *in vitro* and *in silico* approach[1] 78
5.1 Introduction 78
5.2 Materials and Methods 81
5.2.1 Patient Geometry 81
5.2.2 Numerical method 82
5.2.3 Experimental Method 84
5.2.4 Particle selection process 86
5.3 Results and discussion 87
5.4 Conclusions 92
Chapter 6 98
Conclusion and Future Directions 98
6.1 Conclusions 98
6.2 Future Directions 99
Appendix A 101
List of Publications 101

List of Figures

Figure 1.1. Main causes of death in Portugal. Percentage evolution during the period 1988-2015 [1]. 1
Figure 1.2- Major causes of death in Europe among men (a) and women (b). World Health Organization (WHO) mortality database [3] 2
Figure 1.3- Shapes of aneurysms: (a) saccular aneurysm and (b) fusiform aneurysm. Adapted from [20]. 3
Figure 1.4- Formation and rupture of intracranial aneurysm [40]. 5
Figure 1.5- Flow classification scheme. 8
Figure 1.6 - Numerical simulation processing steps involved in an IA study. 10
Figure 1.7 - Stages of the biomodels manufacturing process. 11
Figure 2.1 – Bubbles measurement in the specimen. 32
Figure 2.2 - (a) specimen positioned on the tensile machine. (b) PDMS stress-strain curve. 33
Figure 2.3 – The speciment used in the simple shear test. 33
Figure 2.4 – Experimental setup of 3D Digital Image Correlation. 34
Figure 2.5 - Stress-Strain curve solution for different constitutive hyperelastic mathematical models. 37
Figure 2.6 – Discretization of nodes and elements for Ansys APDL simulation. 38
Figure 2.7 – Force displacement curve for the shear test. 39
Figure 2.8 - Image of 2mm PDMS thickness: a) before deformation; b) beginning of rupture; c) after rupture 39
Figure 2.9 - Image of 4mm PDMS thickness: a) before deformation; b) beginning of rupture; c) after rupture 40
Figure 2.10 – (a) Shear strain field for a 2mm thickness PDMS plate; (b) Shear strain field for a 4mm thickness PDMS plate. 40
Figure 2.11 - Shear strain field obtained by numerical simulation using the Mooney Rivlin constitutive model. (a) 2mm and (b) 4mm of PDMS thickness. 42
Figure 2.12 - Shear strain obtained numerically and experimentally along the y-direction for 2 mm of PDMS. 44
Figure 2.13 - Shear strain obtained numerically and experimentally along the y-direction for 4 mm of PDMS. 44
Figure 3.1 – Mask image processing step. 52

Figure 3.2 – Final model of the aneurysm. 52
Figure 3.3 – (a)STL format; (b) 3D Systems ProJet 1200 printer; (c) Mold matrix Visijet FTX Green. 53
Figure 3.4 - Biomodel in PDMS; (b) Biomodel immersed in pure acetone; (c) Final PDMS biomodel with a cerebral aneurism to perform fluid and pre-clinical experiments..... 54
Figure 4.1 - Segmentation process of the arteries with an aneurysm to obtain the digital model. (a) Willys circle arteries; (b) aneurysm location; (c) vascular aneurysm anatomy obtained; (d) final aneurysm STL model. 61
Figure 4.2 - Models obtained by rapid prototyping and lost wax. (a) model obtained by rapid prototyping of VisiJet FTX Green resin (microsla); (b) bipartite silicone mold; (c) paraffin sacrifice mold, glycerin-based soap and beeswax, respectively (full scale). 62
Figure 4.3 - Processing steps to obtain the final biomodel with paraffin. (a) Paraffin; (b) Biomodel after the cure of PDMS; (c) Final PDMS biomodel. 63
Figure 4.4 - Processing steps to obtain the final biomodel with beeswax. (a) Beewax; (b) Biomodel after the cure of PDMS; (c) Final PDMS biomodel. 63
Figure 4.5 - Processing steps to obtain the final biomodel with glycerine-based soap. (a) glycerine-based soap; (b) Biomodel after the cure of PDMS; (c) Final PDMS biomodel. 64
Figure 4.6 - Experimental setup to perform the flow experiments with the developed PDMS biomodels. 65
Figure 4.7 - Flow inlet and outlet representation. 66
Figure 4.8 - Schematic representation of the locations analysed: (a) in the STL model; (b) microscope image obtained to measure the location C. 66
Figure 4.9 - Distortion of the grid lines shown through the PDMS biomodel manufactured by the lost wax casting process. (a) detail of the particle visualization test; (b) distortion when the channel is filled with PMMA water/glycerol solution and (c) when it is filled with only water. 69
Figure 4.10 Experimental flow analysis with flow rate of: (a) Q = 5 mL/min; (b) Q = 10 mL/min; (c) Q = 15 mL/min; (d) Q = 20 mL/min. 71
Figure 4.11 - Numerical flow analysis with flow rate of: (a) Q = 5 mL/min; (b) Q = 10 mL/min; (c) Q = 15 mL/min; (d) Q = 20 mL/min. 71
Figure 5.1 - ICA aneurysm……..... 81
Figure 5.2 - Details of the grid emplyed in the numerical simulations. ((Front (left) and top (right)) ...……83

Figure 5.3 - Aneurysm biomodel…….84

Figure 5.4 - Experimental setup……...85

Figure 5.5 - Aneurysm top view. Experimental setup to get high angle shots…….…….86

Figure 5.6 - Flow trajectories for different particle size (Top (20 µm), Bottom (60 µm)). Re=11 (Left) and Re=150 (Right)……....88

Figure 5.7 - Top (red), intermediate (blue) and bottom (green) ICA sections…….……88

Figure 5.8 - Numerical and experimental results for non-realistic flow rates……...89

Figure 5.9 - Numerical and experimental results for diastolic flow rate…….90

Figure 5.10 - Numerical and experimental results for intermediate flow rate…….….91

Figure 5.11 - Numerical and experimental results for systolic flow rate…….…….91

List of Tables

Table 2.1 Displacements for the numerical simulations 37
Table 2.2 Average, maximum and minimum shear strain values obtained by simulation 43
Table 4.1 Rapid prototyping specifications for the stereolithografy process 62
Table 4.2 Dimensions and the average error of real PDMS biomodel (mm) obtained with the three different lost core materials 67
Table 4.3 Dimensions and average error of the reduced PDMS biomodel (mm) obtained with the three different lost core materials. 67
Table 4.4 Physical properties of the materials used in this study. 68

List of Abbreviations and Symbols

Abbreviations

ACA	Anterior Cerebral Artery
C	Constants
CFD	Computational Fluid Dynamics
CNC	Computer Numerical Control
CT	Computed Tomography
DIC	Digital Image Correlation
DICOM	Digital Imaging and Communications in Medicine
EC	Endothelial Cell
FDM	Fused Deposition Modeling
FEM	Finite Element Method
HUB	Hospital Universitario de Badajoz
IA	Intracranial Aneurysm
ICA	Internal Carotid Artery
MCA	Middle Cerebral Artery
MJM	Multijet Modeling
MR	Magnetic Resonance
OECD	Organization for Economic anD Development
PC-MRI	Phase Contrast – Magnetic Resonance
PDMS	Polydimethylsiloxane
PIV	Particle Image Velocimetry
PMMA	Polydimethylmethacrylate
PTV	Particle Tracking Velocimetry
RANS	Reynolds Avereged Navier-Stokes
RP	Rapid Prototyping
STL	Stereolithography
TDP	Three Dimensional Priting
WHO	World Health Organization
WSS	Wall Shear Stress
w/w	weight for weight

Symbols:

D	Diameter	m
d_p	Particle diameter	m
F^T	Transposed strain gradient	-
I	Strain Invariant	-
L_f	Characteristics length	m
P	First stress tensor of Piola-Kirchhoff	-
p	Multiple of Lagrange	-
Q	Flow rate	mL/min
Re	Reynolds number	-
Stk	Stokes number	-
T	Room temperature	^oC
v	Velocity	m/s
$\dot{\gamma}$	Strain rate	s^{--1}
λ	Principal strain	-
μ	Dynamic viscosity	Pa . s
ρ	Density	kg/m^3
τ_w	Shear stress	Pa
Ψ	Strain energy	-

Chapter 1

Introduction

Cardiovascular diseases (CVD) remain as the main cause of mortality in Portugal in spite of a reduction observed in the last decades (Fig. 1.1)

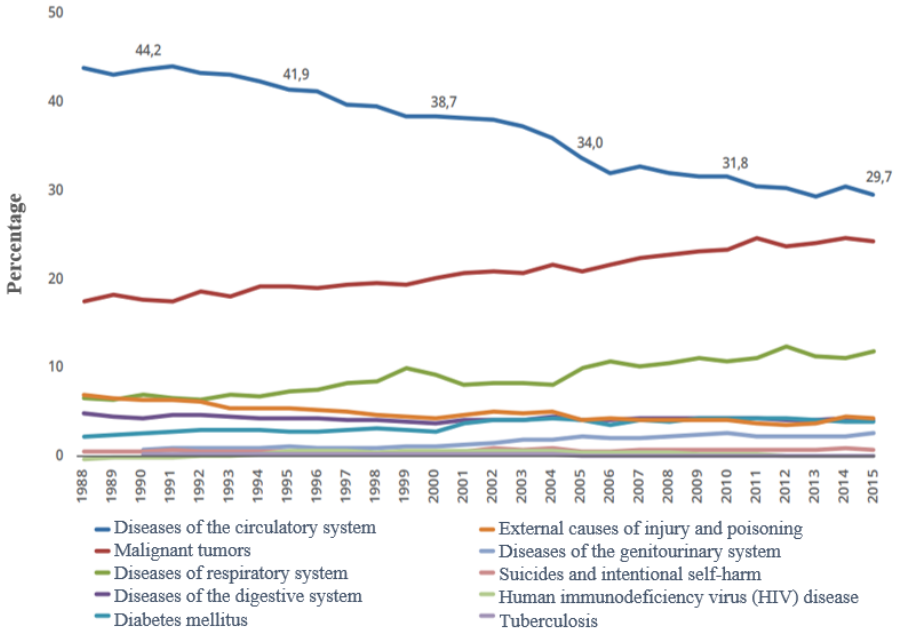

Figure 1.1. Main causes of death in Portugal. Percentage evolution during the period 1988-2015 [1].

CVD are the leading cause of mortality among women and the second largest for men in Portugal. 34% of women and 27% of men death per 100,000 inhabitants according to the Organization for Economic Cooperation and Development (OECD) data [2].

Regarding Europe, these diseases cause more than 4 million deaths per year, which represents 45% of the total. Europe's trend is similar to Portugal's, being higher the number of deaths from CVD in women (2.2 million) than in men (1.8 million) which represent 49% in women and 40% in men [3], as shown in Figure 1.2

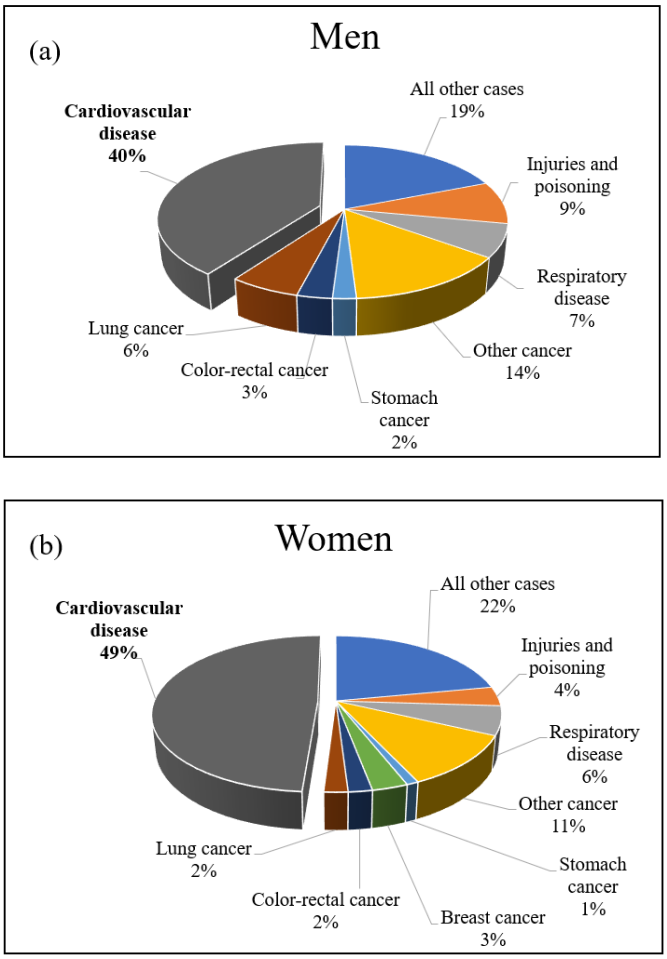

Figure 1.2- Major causes of death in Europe among men (a) and women (b). World Health Organization (WHO) mortality database [3].

CVDs cover the pathologies of the entire circulatory system and include both the coronary heart and the cerebrovascular diseases. These last diseases are the biggest contributors to the death rates, representing 1.8 million and 1.0 million deaths, respectively [3].

In particular, we need to mention the intracranial aneurysm (IA), the abdominal one, and the stenosis. The aneurysms are abnormal dilation of the blood vessels and present either saccular or fusiform form [4,5]. If the vessels are affected by atherosclerosis, they suffer the opposite process (narrowing) and a stenosis is formed [6,7]. Among the aforementioned pathologies when an IA ruptures, it causes a hemorrhagic stroke, which has one of the highest mortality rates in European countries [8]. Recent studies in IAs [9-12] have allowed some progress in the diagnosis, the identification of several risk factors, and the development of surgical procedures [13].

However significant improvement is still necessary. This improvement is related to a better understanding of the factors which trigger their appearance, growth, and rupture. This dissertation focuses on the hemodynamic study of a real IA both experimental and numerically. For this reason, the following will present some basic concepts of the main aspects that will be analysed in this dissertation.

1.1 Intracranial Aneurysm

The IA appears in a weakened and protruding area in an artery wall. The wall dilates and takes the form of a thin balloon. It is often located in the arteries of the Willis circle [14,15].

IAs can be classified, according to their format, into saccular aneurysms, and fusiform aneurysms. About 90% of aneurysms are saccular [16], as can be seen in Figure 1.3a. They have a neck that connects with the blood vessel and a larger rounded part called the dome. Their preferable location are both in the curved arteries and bifurcation vicinities [17]. Fusiform aneurysms (Figure 1.3b) are less frequent [18] do not have a neck and tend to expand on both sides of the artery. Often do not occur in the cerebral arteries and are commonly found in the abdominal aorta or the popliteal artery behind the knees [19].

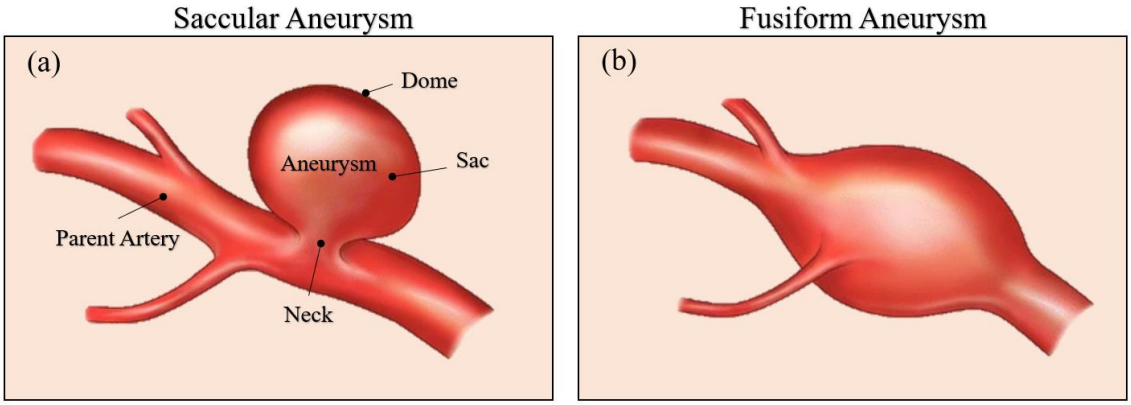

Figure 1.3- Shapes of aneurysms: (a) saccular aneurysm and (b) fusiform aneurysm. Adapted from [20].

It is estimated that approximately 3-5% of the population has an IA [21]. Its rupture cause 85% of subarachnoid hemorrhages [22]. The mortality associated with these

ruptures oscillates in a 50%-60% range and the dependence rate among survivors range from 30% to 40% [23].

Although approximately 50% to 80% of the IA do not break down during their lifetime [24], the abovementioned reasons make the IA one of the most feared cerebrovascular diseases. For this reason, it is a big dilemma, the treatment of an unbroken intracranial aneurysm. According to the latest Brain Aneurysm Foundation norm [25], an IA should be treated right after its detection. Nevertheless, the treatment involves high expenses and serious risk [26-28].

As previously mentioned, there is a need for understanding the mechanisms not only for the formation and growth of IA, but also for its breaking up [26]. There are complex biological and physical relations which determine the degradation and the weakening of the blood vessel wall [19,29]. These relations arise as a result of changes in hemodynamic load and biomechanical stress. However, these interactions are not yet fully understood [30].

1.2 Hemodynamic Fundamentals

It is been supposed that hemodynamic factors play a key role in the formation, growth, and rupture of IA for a long time [31]. One of the first reviews pointed hemodynamic stresses as the responsible for degenerative lesions in the vessel wall [32]. These lesions could trigger the AI appearance and genetic factors, or hypertension can aggravate them. Ferguson *et al.* [33,34] suggested the transition from laminar flow to turbulence inside the IA as a significant stress source on the wall. That leads to a degeneration of the vessel's internal elastic lamina and contributes to the progression and rupture of the aneurysm. Subsequent studies established the shear stress on the wall (WSS) as the primary hemodynamic parameter which affects aneurysm rupture [35-37]. However, this rupture still arises questions which factor has a bigger effect: WSS high values or lower ones [38].

Figure 1.4 shows a well-established fact. Endothelial cells (ECs) sense flow changes and respond to WSS through the cell surface and its intracellular mechanosensors [39]. ECs can transmit flow signals to adjacent cells like smooth muscle cells. If there are any abnormalities in the flow, it results in a ECs pathological responses that can lead to the onset and rupture of the aneurysm [26-40]. Therefore, understanding the behavior of

blood flow in AI, using experimental and numerical tools is of utmost importance. It is crucial to establish how the different hemodynamic forces and flow patterns affect ECs and, consequently, the walls of arterial vessels. WSS and other important concepts are extensively explained in the present section.

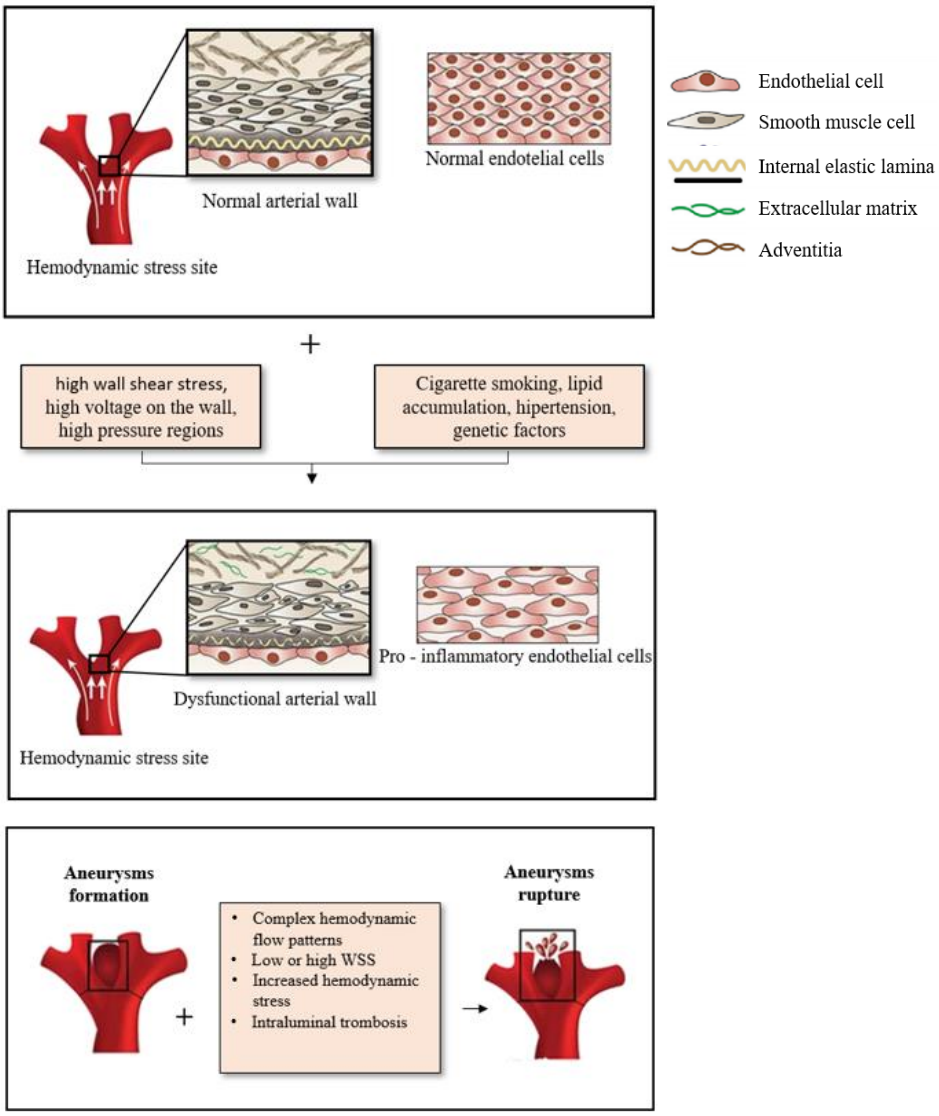

Figure 1.4- Formation and rupture of intracranial aneurysm [40].

1.2.1 Blood viscosity

According to Newton's law of viscosity (equation 1.1), a fluid is considered Newtonian when the resulting strain rate ($\dot{\gamma}$) is proportional to the applied shear stress (τ_w), being μ the fluid's dynamic viscosity [41].

$$\tau_w = \mu \cdot \dot{\gamma} \tag{1.1}$$

Dynamic viscosity is a property of the fluid, which represents the ease with which the fluid flows. This viscosity remains constant in Newtonian fluids (i.e., water) for fixed pressure and temperature conditions. Fluids that do not fulfill equation 1 are called non-Newtonian. Blood does not have a linear relationship between shear stress and the strain rate. So its dynamic viscosity is not constant [41].

The non-linear blood's behavior arises depending on the vessel diameter and the flow rate. The viscosity decreases with the diameter in small vessels, such as capillaries, at high flow speeds; conversely, the blood viscosity remains almost constant in large diameter arteries [41,4]. The cerebral arteries caliber, allows considering blood as Newtonian to perform either in vitro or in silico IAs studies.

1.2.2 Reynolds number

The Reynolds number (Re) is a crucial dimensionless number to identify a fluid's flow regime (laminar, turbulent, and transitional). It is calculated as the ratio between the inertial and viscous forces exerted on an element of the fluid:

$$Re = \frac{inertial\ forces}{viscous\ forces} = \frac{\rho v D}{\mu} \tag{1.2}$$

where ρ is the density of the fluid, v the flow speed, D the diameter of the blood vessel and μ the fluid's dynamic viscosity.

Re ranges from 1 (small arterioles) to 4000 (aorta). Laminar flow (Re <2000) is described by a parabolic velocity profile where the fastest molecules are in the center of the vessel, and the velocity decreases towards the walls. Turbulent flow (Re> 4000) occurs at very high blood speeds. In the transition region (2000 <Re <4000), the flow can vary chaotically between laminar and turbulent [42].

In the case of aneurysms, critical Re, which indicates the value at which a laminar flow becomes turbulent, may vary according to the geometry of the blood vessel. The study carried out by Ferguson [43] demonstrated, using the Evans blue indicator, that the Re in bifurcations varied according to the angle and whether it had an aneurysm or not. In his experiment, he observed that the critical Re dropped from 2500, in the straight tube,

to 1200 in the 180º bifurcation, while, with the presence of the aneurysm at the apex of the 90º bifurcation the value of the critical Re dropped from 2500 to 400 [43].

1.2.3 Blood pressure

The cardiac cycle is an important parameter in the hemodynamic study in IA. During diastole, the ventricles fill with blood, and in systole the ventricles contract and pump blood out of the heart and into the main arteries [4]. Consequently, blood flow is unstable, showing pulsatile conditions in all arteries that present pulsatile profiles and depend on the local pressure wave [4,44].

In an aneurysm, the flow patterns are altered according to the cardiac cycle. A higher flow rate is directed within the aneurysmal sac and vortexes are formed during systole. On the other hand, the flow can leave the sac or redistribute itself to stagnation or vortex area during diastole [45,40].

1.2.4 Wall Shear Stress - WSS

As mentioned in section 1.2.1, Newtonian fluids fulfill equation (1.1). Near the wall the WSS can be calculated as:

$$\tau_w = -\mu \cdot \left(\frac{\partial v}{\partial y}\right)_{y=0} \tag{1.3}$$

where μ is the dynamic viscosity, v is the blood velocity parallel to the wall and, y is the distance from the arterial wall. As above-mentioned WSS is one of the most used parameters in the hemodynamic study of IA. However, controversial results of low and high WSS are correlated with aneurysm rupture and growth [30]. Some research has found that ruptured aneurysms were more likely to have a high WSS [46]. Cebral *et al.* [47,48] associated the high WSS in stiffened and very thin areas of the wall with the rupture of AI. Other researchers reported that the degradation of the wall is caused by low WSS [49-51].

Many studies compare ruptured and non-ruptured aneurysms. The non-ruptured geometries were reconstructed from ruptured IAs scanned images [52-55]. As it is not possible to reach an exact reconstruction of the unruptured IA, the resulting WSS values are altered. Therefore, it is necessary to establish a research standard and carry out further studies using unbroken IA models. It is mandatory to assess in detail the different flow

patterns within the aneurysmal sac and correlate their effects with the WSS values.

1.2.5 Blood flow classification

Visualizing the local streamlines (experimentally or numerically) [56] allows us to classify the blood flow patterns. Figure 1.5 shows the main classification scheme for the blood flow.

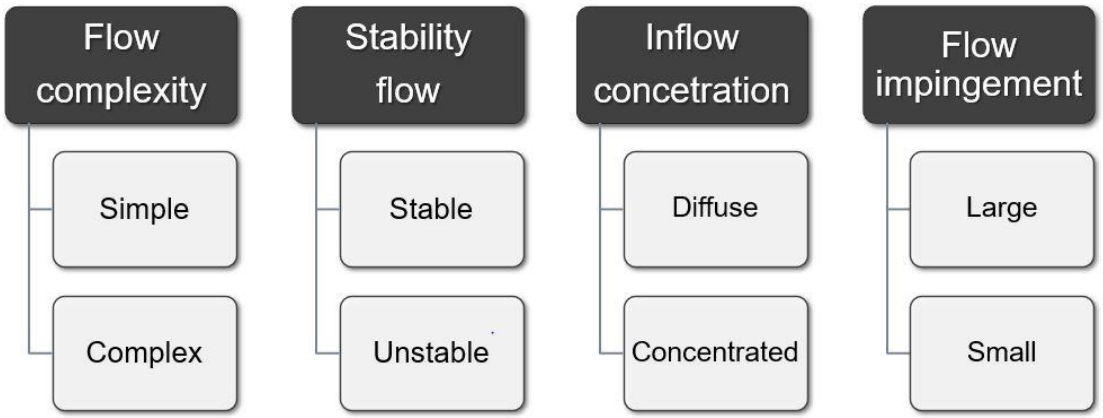

Figure 1.5- Flow classification scheme.

- Flow Complexity: It reflects the recirculation present in the IA during the cardiac cycle. A simple flow pattern indicates a single zone of recirculation in the aneurysmal sac and complex patterns indicate more than one region of recirculation.
- Stability flow: this parameter indicates the persistence of the flow behavior in the cardiac cycle. A steady flow does not show changes during the cardiac cycle, that is, the recirculation structures remain in the same place throughout the cycle. However, vortex structures can appear or disappear in the aneurysm in the same cycle in an unstable flow.
- Inflow concentration: Concentrated flows are the ones where a thin jet enters the aneurysmal sac in the main direction of the flow. Diffuse ones indicate a thicker inlet flow which disperse quickly as penetrating the aneurysm.
- Flow impingement: It is related to the region where the incoming current collides the aneurysm wall and its redirected. This region is usually associated with a high WSS area. If this zone covers less than 50% of the IA area, a small impact is considered, being great otherwise.

Studies by Cebral *et al* [56,57] have shown that ruptured AIs are more likely to have complex flow patterns, unstable flow, concentrated inlet jets, and small impact regions.

1.3 Types of studies

In the previous section, we have stated that a study of the local hemodynamic is crucial to understand the evolution of pathologies such as aneurysm [58,59,26]. There are three ways to deal with this problem: *in vivo*, *in silico*, and *in vitro*.

In vivo studies can accurately represent physiological conditions and are effective in validating new devices and treatments. However, in addition to ethical issues, they are expensive and have low reproducibility [60].

Computer Technology advance has allowed many researchers to use numerical tools, such as computational fluid dynamics (CFD), to investigate blood flow characteristics in IA. Nevertheless, this type of study needs experimental validation [61,62].

Due to the actual issues concerning *in vivo* studies, *in vitro* analyses are necessary to validate and complemented with numerical studies. Furthermore, they provide different experimental methods of flow visualization to analyse qualitatively and quantitatively the different hemodynamic factors that related to the pathologies of the circulatory system [63,64].

1.3.1 *In vivo*

Currently, the most used non-invasive *in vivo* techniques for flow measurements are computed tomography (CT) [65], ultrasound [66], doppler [67], and phase-contrast magnetic resonance (PC-MRI) [68]. CT is widely used to assess the anatomy of the artery [69] but the amount of radiation limits its use for research purposes. Doppler measurements can catch the temporal evolution of the velocity in a plane [70] buts it cannot work through air or bones (restricting its use in lung, ribs, and skull) [71]. Magnetic resonance allows the acquisition of three-dimensional anatomy and analysis of the speed field, but its low spatiotemporal resolution is limited and tends to underestimate both WSS and flow rate [72,73].

Despite the actual limitations, some authors have employed *in vivo* non-invasive techniques to capture complex flow patterns in aneurysms [74,75]. Their results have

been mainly used to get boundary conditions applicable to both *in vitro* and *in sílico* numerical studies as the flow velocity curves [76,26].

1.3.2 *In sílico*

IA research has benefited from the computer technology advance. Both the price reduction and the increase in computing capabilities have allowed extensively research through CFD since the 90s [77]. CFD is currently the most used numerical tool in the study of blood flow in IA and allows qualitative and quantitative studies of parameters such as pressure, wall shear stress and flow velocities [26].

The main advantages of the CFD method, when compared to other research methods, are the reduction of delivery times, the ability to study large systems, and the greater detail of the results [78]. The disadvantages of the method are: high cost with licenses and commercial software [78] and the need for experimental validation [26].

We can split any CFD study into three stages (Figure. 1.6): obtaining the geometry, meshing it, and, finally, the numerical solution.

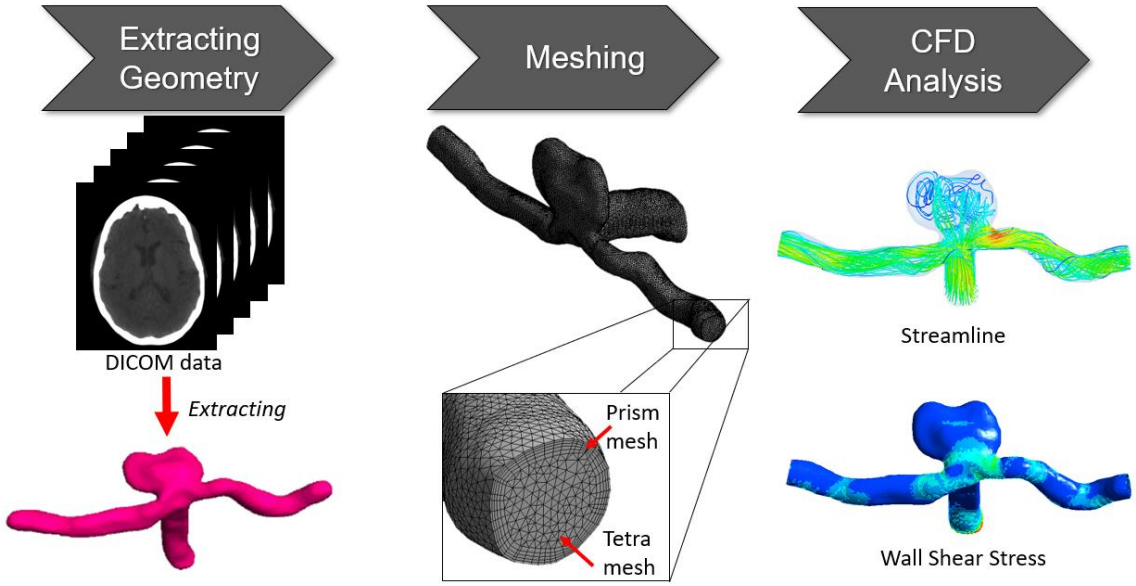

Figure 1.6 - Numerical simulation processing steps involved in an IA study.

The first step in this analysis is the geometry generation. Starting from medical images, a geometry is extracted in STL format using segmentation tools, such as Mimics or ScanIp software [79]. This geometry is exported to a CFD software (i.e. Ansys Fluent) where an appropriate mesh will be generated. Then we impose on this mesh, appropriate boundary conditions, and the properties of the fluid. After this stage, the governing

equations are solved, which are: continuity equation (conservation of mass) and Navier-Stokes equations (amount of movement). The results obtained can be presented in different ways. For example, both streamlines and the wall shear stress, widely used in the IA analysis, can be studied in different ways depending on the analysis.

1.3.3 *In vitro*

In vitro experiments use a physical representation of the artery and impose appropriate flow boundary conditions to analyse the main local hemodynamic parameters of cardiovascular pathologies.

First IA *in vitro* studies appeared in the 1970s [43,33]. Many researchers have developed different *in vitro* techniques to study the hemodynamic of IAs since then: video microscopy and image analysis, laser-doppler [80], and particle-based methods, such as particle tracking velocimetry (PTV) [81] and particle image velocimetry (PIV) [82]. Currently, the PIV is the most preferred technique to validate CFD studies. However, its use is limited to a single plane which hinders the 3D analysis of the AI flow [76].

The main advantages of the *in vitro* study are easy speed control, no ethical problems, and the possibility of validating numerical studies. The disadvantages are: the limitations of manufacturing the biomodels and the difficulty of measuring some variables such as WSS [62,83].

To perform *in vitro* experiments, the construction of blood vessel biomodels (flow phantom) is necessary. Manufacturing usually takes place in three stages, as shown in Figure 1.7.

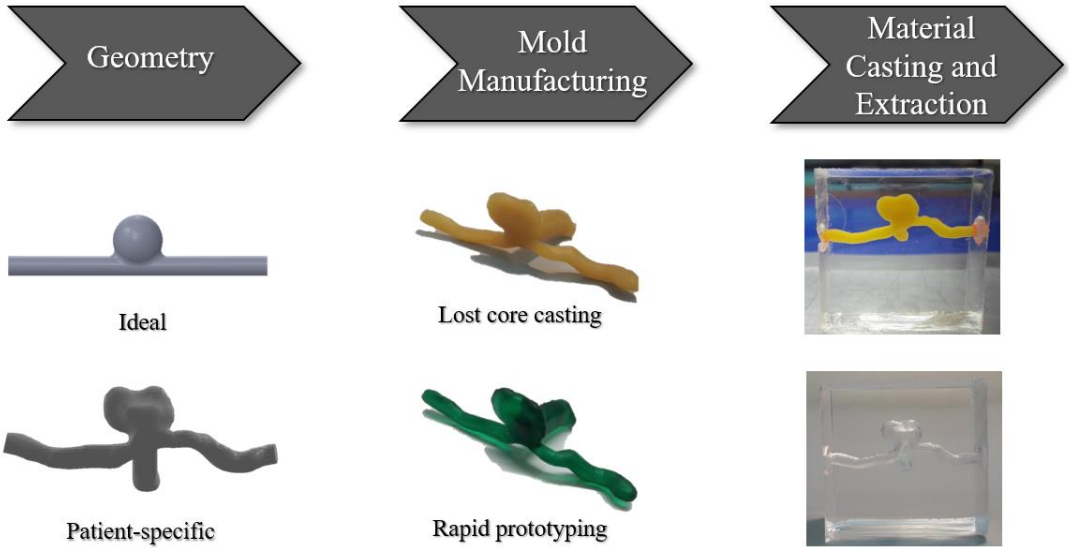

Figure 1.7 - Stages of the biomodels manufacturing process.

The process starts defining the 3D blood vessel model. This model can be idealized or represent a real geometry from a specific patient. Idealized models are built from average values of the specific dimensions of the patient, which include: the constant diameter, the angle adjustment, and the reduced or eliminated curvature [84,85]. These models are generally used to study morphological patterns, to have a generalizable understanding of certain flow phenomena, and to investigate the effectiveness of materials and fluids used in experimental procedures [86,87]. On the other hand, patient-specific models are obtained from radiological techniques such as angiography [88]. Medical images are segmented and the results are converted to the STereoLithography (STL) format, which will be used in the next stage of rapid prototyping [62].

Then, a mold of the vessel lumen is manufactured. Two techniques are mainly used: rapid prototyping and lost core casting. Rapid prototyping converts STL models into physical objects [89]. It employed different printing techniques:stereolithography (SLA)[90], multijet modeling (MJM) [91], fused deposition modeling (FDM)[92], etc. The printed materials are ABS [93,94], plaster powder [88] and resin [95]. Lost core casting alternatively uses split silicone casts to mold different materials, such as wax, sucrose, chocolate, and low-temperature iron [62].

Finally, the manufactured vessel lumen mold is coated with a material, usually in liquid form. This material must be transparent and have a low refractive index. The most used ones are polydimethylsiloxane (PDMS) [96,97], glass [98] and acrylic polydimethylmethacrylate (PMMA) [99]. However, PDMS is preferred over the rest in researching because of its properties (transparency, ease of manufacture, and low cost [100]). Once the material has cured, the last step consists of removing the lumen mold. Three alternatives can be selected: mechanically, melting, or using solvents [62].

In this work, an *in vitro* experimental study will be widely used, not only to validate the numerical studies, but as a tool to visualize the different flow patterns within the aneurysmal sac that are correlated with the development of IA.

1.4 Motivation and Goals

Despite advances in hemodynamic experimental studies in IA, they still present great difficulties. There is a need to use biomodels suitable for specific tests and equipment for visualizing the flow. PIV is the most used technique for validating

numerical studies, however, this method is not enough to characterize the hemodynamics inside the IA, as it does not capture the three-dimensional flow behavior. In addition to these limitations, there is also a lack of simple and low-cost manufacturing methods for biomodels. These limitations mean that many hemodynamic studies in IA are carried out in a restrictive way, using only the numerical method, which generates results that, usually, must be validate.

Therefore, the general objective of this work is to manufacture IA biomodels suitable for experimental hemodynamic tests *in vitro*, using low cost materials and implement fluid flow numerical simulations in models of real aneurysms. This general objective is subdivided into the following specific objectives:

1. Mechanical characterization of the material used in the manufacture of the biomodel.
2. Use the lost core casting technique, with low-cost materials and evaluate the different methods of removing the lost core.
3. Test different fluids with rheological properties close to the blood and with a refractive index similar to the material used in the biomodels.
4. Characterize the manufactured biomodels as to their transparency and relative error.
5. Design and implement an experimental configuration to visualize the high-speed flow inside the biomodel.
6. Perform the tracking of particles obtained through a video using the ImageJ software to show the flow trajectories.
7. Make a qualitative analysis by comparing the flow lines obtained in experimental tests with those obtained in numerical simulations.

1.5 Structure

This dissertation is divided into six chapters. The first chapter has addressed the importance of hemodynamic studies to understand the phenomena that lead to the formation, growth, and rupture of AI. It provides the theoretical concepts of fluid mechanics and the main types of blood flow studies used in AI. In this chapter, the motivation for carrying out this work and the objectives to be achieved are also reported.

As the intracranial aneurysms are subject to shearing efforts, exerted by blood, in the second chapter two approaches will be presented, numerical and experimental, in order to characterize these effects in the PDMS which is the material used in the biomodels. The experimental method was implemented with a simple shear test associated with the 3D digital image correlation and a finite element software was used to implement the numerical simulations. The results obtained in this stage are important to carry out studies of the fluid-structure interaction in flexible biomodels of intracranial aneurysm.

The third chapter reports the process to manufacture intracranial aneurysm biomodels of specific patient geometry obtained from a computerized angiography. The lost core was produced using rapid prototyping technology, using stereolithography and the chosen material was FTX Green. This material has a high surface finish, however, its biomodel removal process takes time and requires the use of acetone to dissolve it.

The fourth chapter describes, in detail, a new fast manufacturing process that uses low-cost and easy-to-remove materials. In this chapter, new materials are presented for the lost core, which until now, had not been used for this purpose. The biomodels obtained were tested, compared and discussed which ones are most suitable for hemodynamic studies, using optical techniques to visualize the fluid flow.

The fifth chapter presents the combination of experimental *in vitro* and numerical CFD tests on the biomodels manufactured in chapter 4. An experimental setup was built and optimized for carrying out microparticle flow tests inside the biomodel. The tests were recorded with a high-speed camera and the results were processed with the ImageJ software. The results show the three-dimensional behavior of the aneurysm, such as helical flows and vortex, which allows a qualitative validation of the implemented numerical models.

In the sixth and last chapter, conclusions regarding the stages of the work developed are presented and some proposals for future work are described.

References

[1] DGS, *Programa nacional para as doenças cérebro-cardiovasculares*. 2017.

[2] OECD, *Portugal: country health profile*. 2017.

[3] N. Townsend, L. Wilson, P. Bhatnagar, K. Wickramasinghe, M. Rayner, and M. Nichols, "Cardiovascular disease in Europe : epidemiological update 2016," *Eur. Heart J.*, vol. 37, pp. 3232–3245, 2016.

[4] L. Campo-dea, S. N. Oliveira, and F. T. Pinho, "A Review of Computational Hemodynamics in Middle Cerebral Aneurysms and Rheological Models for Blood Flow," vol. 67, no. 1, pp. 1–16, 2016.

[5] C. Rodriguez-Régent *et al.*, "Non-invasive diagnosis of intracranial aneurysms," *Diagn. Interv. Imaging*, vol. 95, no. 12, pp. 1163–1174, 2014.

[6] E. Doutel, S. I. S. Pinto, J. B. L. M. Campos, and J. M. Miranda, "Link between deviations from Murray ' s Law and occurrence of low wall shear stress regions in the left coronary artery," *J. Theor. Biol.*, vol. 402, pp. 89–99, 2016.

[7] Y. Sun and X. Guan, "Autophagy: A new target for the treatment of atherosclerosis," *Front. Lab. Med.*, vol. 2, no. 2, pp. 68–71, 2018.

[8] M. Nichols, N. Townsend, P. Scarborough, and M. Rayner, "Cardiovascular disease in Europe 2014 : epidemiological update," *Eur. Heart J.*, vol. 35, pp. 2950–2959, 2014.

[9] S. Rashad *et al.*, "Impact of bifurcation angle and inflow coefficient on the rupture risk of bifurcation type basilar artery tip aneurysms," *J Neurosurg*, vol. 128, pp. 723–730, 2018.

[10] G. Zhou, Y. Zhu, Y. Yin, M. Su, and M. Li, "Association of wall shear stress with intracranial aneurysm rupture : systematic review and meta- analysis," *Sci. Rep.*, vol. 7, pp. 1–8, 2017.

[11] S. Rashad, T. Hassan, W. Aziz, and A. Marei, "Carotid artery occlusion for the treatment of symptomatic giant carotid aneurysms: a proposal of classification and surgical protocol," *Neurosurg Rev.*, vol. 37, pp. 501–511, 2014.

[12] L. Xu, F. Liang, L. Gu, and H. Liu, "Flow instability detected in ruptured versus

unruptured cerebral aneurysms at the internal carotid artery," *J. Biomech.*, vol. 72, pp. 187–199, 2018.

[13] E. M. Database, "Procedural clinical complications, case-fatality risks, and risk factors in endovascular and neurosurgical treatment of unruptured intracranial aneurysms a systematic review and meta-analysis," vol. 76, no. 3, pp. 282–293, 2019.

[14] B. Weir, "Unruptured intracranial aneurysms : review," *J Neurosurg*, vol. 96, pp. 3–42, 2002.

[15] D. M. Sforza, C. M. Putman, J. R. Cebral, and F. Dynamics, "Hemodynamics of Cerebral Aneurysms," *Annu Rev Fluid Mech*, vol. 41, pp. 91–107, 2009.

[16] A. Keedy, "An overview of intracranial aneurysms," vol. 9, no. 2, pp. 141–146, 2006.

[17] G. N. Foutrakis, H. Yonas, and R. J. Sclabassi, "Saccular aneurysm formation in curved and bifurcating arteries," *AJNR Am J Neuroradiol*, vol. 20, pp. 1309–1317, 1999.

[18] E. A. Barletta *et al.*, "Fusiform aneurysms : A review from its pathogenesis to treatment options," *Surg. Neurol. Int.*, vol. 9, no. 189, 2018.

[19] J. C. Lasheras, "The Biomechanics of Arterial Aneurysms," *Annu. Rev. ofFluid Mech.*, vol. 39, pp. 293–321, 2007.

[20] K. W. G. Carolan-rees, "Pipeline TM embolization device for the treatment of complex intracranial aneurysms," *Appl Heal. Econ Heal. Policy*, vol. 11, pp. 5–13, 2013.

[21] L. Allard, G. Soulez, B. Chayer, F. Treyve, Z. Qin, and G. Cloutier, "Multimodality vascular imaging phantoms: A new material for the fabrication of realistic 3D vessel geometries," *Med. Phys.*, vol. 36, no. 8, pp. 3758–3763, 2009.

[22] S. Sathyan *et al.*, "Association of Versican (VCAN) gene polymorphisms rs251124 and rs2287926 (G428D), with intracranial aneurysm," *Meta Gene*, vol. 2, pp. 651–660, 2014.

[23] P. S. Amenta *et al.*, "Analysis of nonmodifiable risk factors for intracranial

aneurysm rupture in a large, retrospective cohort," *Neurosurgery*, vol. 70, no. 3, pp. 693–701, 2012.

[24] J. L. Brisman, J. K. Song, and D. W. Newell, "Cerebral Aneurysms," *New Engl. J. os Med.*, vol. 355(9), pp. 928–939, 2006.

[25] C. David, C. Buckley, and J. C. Rogers, *Brain aneurysms detection and treatment*. 2017.

[26] K. M. Saqr *et al.*, "What does computational fluid dynamics tell us about intracranial aneurysms? A meta-analysis and critical review," *J. Cereb. Blood Flow Metab.*, vol. 40, no. 5, pp. 1021–1039, 2019.

[27] M. H. M. Vlak, A. Algra, R. Brandenburg, and G. J. E. Rinkel, "Prevalence of unruptured intracranial aneurysms , with emphasis on sex , age , comorbidity , country , and time period : a systematic review and meta-analysis," *Lancet Neurol.*, vol. 10, no. 7, pp. 626–636, 2011.

[28] D. O. Wiebers, J. C. Torner, and I. Meissner, "Impact of Unruptured Intracranial Aneurysms on Public Health in the United States," *Stroke*, vol. 23, pp. 1416–1419, 1992.

[29] G. Tromp, S. Weinsheimer, A. Ronkainen, and H. Kuivaniemi, "Molecular basis and genetic predisposition to intracranial aneurysm," *Ann. Med.*, vol. 46, no. 8, pp. 597–606, 2014.

[30] J. R. Cebral and M. Raschi, "Suggested connections between risk factors of intracranial aneurysms: A review," *Ann. Biomed. Eng.*, vol. 41, no. 7, pp. 1366–1383, 2013.

[31] N. Hashimoto *et al.*, "Animal model Of cerebral aneurysms : Pathology and pathogenesis of induced cerebral aneurysms in rats," *Neurol. Res.*, vol. 6, no. 1–2, pp. 33–40, 1984.

[32] N. Zealand, "Review Article Etiology of intracranial berry aneurysms," *J Neurosurg*, vol. 70, pp. 823–831, 1989.

[33] G. G. Ferguson, "Turbulence in human intracranial saccular aneurysms," *J Neurosurg*, vol. 33, pp. 485–497, 1970.

[34] G. G. Ferguson, “Physical factors in the initiation, growth, and rupture of human intracranial saccular aneurysms,” *J Neurosurg*, vol. 37, pp. 666–677, 1972.

[35] H. J. Steiger and H. Reulen, “Low frequency flow fluctuations in saccular aneurysms,” *Acta Neurochir*, vol. 83, pp. 131–137, 1986.

[36] D. W. Liepsch, H. J. Steiger, A. Poll, H. B. Wallis, and R. Mirage, “Hemodynamic stress in lateral saccular aneurysms,” *Biorheology*, vol. 24, pp. 689–710, 1987.

[37] C. Kim, C. Piitzold, Y. Tokuriki, Y. Takebe, and K. Hori, “In vivo study of flow pattern at human carotid bifurcation with regard to aneurysm development,” *Acta Neurochir*, vol. 115, pp. 112–117, 1992.

[38] Y. Murayama, S. Fujimura, T. Suzuki, and H. Takao, “Computational fluid dynamics as a risk assessment tool for aneurysm rupture,” *Neurosurg. Focus*, vol. 47, no. 1, p. 12, 2019.

[39] P. F. Davies, “Flow-mediated endothelial mechanotransduction,” *Physiol Rev*, vol. 75, no. 3, pp. 519–560, 2011.

[40] P. Texakalidis *et al.*, “Literature review aneurysm formation , growth , and rupture : the biology and physics of cerebral aneurysms,” *World Neurosurg.*, vol. 130, pp. 277–284, 2019.

[41] D. Katritsis, L. Kaiktsis, A. Chaniotis, J. Pantos, E. P. Efstathopoulos, and V. Marmarelis, “Wall Shear Stress : theoretical considerations and methods of measurement,” vol. 49, no. 5, pp. 307–329, 2007.

[42] E. D. Costa, “Hemodynamics in the left coronary artery – numerical and in vitro approaches,” Faculty of Engineering, University of Porto, Portugal, 2016.

[43] M. Roach, R. Scott, and G. G. Ferguson, “The hemodynamic importance of the geometry of bifurcations in the circle of willis (glass model studies),” *Stroke*, vol. 3, pp. 255–268, 1972.

[44] N. Xiao, J. D. Humphrey, and C. A. Figueroa, “Multi-scale computational model of three-dimensional hemodynamics within a deformable full-body arterial network,” *J. Comput. Phys.*, vol. 244, pp. 22–40, 2013.

[45] L. Counord, P. Flaud, and J. Duffaux, “In vitro study of haemodynamics in a giant

saccular aneurysm model : influence of flow dynamics in the parent vessel and effects of coil embolisation," *Neuroradiology*, vol. 36, pp. 530–536, 1994.

[46] S. Hodis, S. Uthamaraj, G. Lanzino, D. F. Kallmes, and D. Dragomir-daescu, "Computational fluid dynamics simulation of an anterior communicating artery ruptured during angiography," *J. Neurointerv. Surg.*, vol. 6, p. 14, 2013.

[47] J. R. Cebral *et al.*, "Analysis of hemodynamics and wall mechanics at sites of cerebral aneurysm rupture," *J NeuroIntervent Surg*, vol. 7, pp. 530–536, 2015.

[48] J. R. Cebral, F. Mut, J. Weir, and C. Putman, "Quantitative Characterization of the Hemodynamic Environment in Ruptured and Unruptured Brain Aneurysms," *AJNR Am J Neuroradiol*, vol. 32, no. 1, pp. 145–151, 2011.

[49] J. Xiang, J. Yu, K. V Snyder, E. I. Levy, A. H. Siddiqui, and H. Meng, "Hemodynamic – morphological discriminant models for intracranial aneurysm rupture remain stable with increasing sample size," *J. Neurointerv. Surg.*, vol. 8, pp. 104–110, 2016.

[50] L. Goubergrits, J. Schaller, U. Kertzscher, and N. Van Den Bruck, "Statistical wall shear stress maps of ruptured and unruptured middle cerebral artery aneurysms," *J. R. Soc. Interface*, vol. 9, no. September 2011, pp. 677–688, 2012.

[51] S. Omodaka *et al.*, "Local hemodynamics at the rupture point of cerebral aneurysms determined by computational fluid dynamics analysis," *Cerebrovasc Dis*, vol. 34, pp. 121–129, 2012.

[52] W. Brinjikji, B. J. Chung, C. Jimenez, C. Putman, D. F. Kallmes, and J. R. Cebral, "Hemodynamic differences between unstable and stable unruptured aneurysms independent of size and location : a pilot study," *J. Neurointerv. Surg.*, vol. 9, pp. 376-380., 2017.

[53] Y. Zhang *et al.*, "Clinical , morphological , and hemodynamic independent characteristic factors for rupture of posterior communicating artery aneurysms," *J Neurointerv Surg*, vol. 8, pp. 808–812, 2016.

[54] J. J. Schneiders *et al.*, "Additional value of intra-aneurysmal hemodynamics in discriminating ruptured versus unruptured intracranial aneurysms," *AJNR Am J Neuroradiol*, vol. 36, pp. 1920–1926, 2015.

[55] M. Ramachandran *et al.*, “Assessment of image-derived risk factors for natural course of unruptured cerebral aneurysms,” *J Neurosurg*, vol. 124, pp. 288–295, 2016.

[56] J. R. Cebral, F. Mut, J. Weir, and C. M. Putman, “Association of hemodynamic characteristics and cerebral aneurysm rupture,” *Am. J. Neuroradiol.*, vol. 32, no. 2, pp. 264–270, 2011.

[57] J. R. Cebral, M. A. Castro, J. E. Burgess, R. S. Pergolizzi, M. J. Sheridan, and C. M. Putman, “Characterization of cerebral aneurysms for assessing risk of rupture by using patient-specific computational hemodynamics models,” *Am. J. Neuroradiol.*, vol. 26, no. 10, pp. 2550–2559, 2005.

[58] N. Chalouhi, B. L. Hoh, and D. Hasan, “Review of cerebral aneurysm formation, growth, and rupture,” *Stroke*, vol. 44, no. 12, pp. 3613–3622, 2013.

[59] S. Fukuda and Y. Shimogonya, “The role of hemodynamic factors on the development, enlargement, and rupture of cerebral aneurysms: A combination of computational fluid dynamics analysis and an animal model study,” *Japanese J. Neurosurg.*, vol. 23, no. 8, pp. 661–666, 2014.

[60] W. M. P. F. Bosman *et al.*, “Aortic customize: An in vivo feasibility study of a percutaneous technique for the repair of aortic aneurysms using injectable elastomer,” *Eur. J. Vasc. Endovasc. Surg.*, vol. 40, no. 1, pp. 65–70, 2010.

[61] E. Doutel, J. Carneiro, J. B. L. M. Campos, and J. M. Miranda, “Experimental and numerical methodology to analyze flows in a coronary bifurcation,” *Eur. J. Mech. B/Fluids*, vol. 67, pp. 341–356, 2018.

[62] S. G. Yazdi, P. H. Geoghegan, P. D. Docherty, M. Jermy, and A. Khanafer, “A review of arterial phantom fabrication methods for Flow measurement using PIV techniques,” *Ann. Biomed. Eng.*, vol. 46, no. 11, pp. 1697–1721, 2018.

[63] Y. Hoi, S. H. Woodward, M. Kim, D. B. Taulbee, and H. Meng, “Validation of CFD simulations of cerebral aneurysms with implication of geometric variations,” *J. Biomech. Eng.*, vol. 128, no. 6, pp. 844–851, 2006.

[64] E. Doutel, N. Viriato, J. Carneiro, J. B. L. M. Campos, and J. M. Miranda, “Geometrical effects in the hemodynamics of stenotic and non-stenotic left

coronary arteries—numerical and in vitro approaches," *Int. j. numer. method. biomed. eng.*, pp. 0–2, 2019.

[65] K. Stepniak, A. Ursani, N. Paul, and H. Naguib, "Development of a phantom network for optimization of coronary artery disease imaging using computed tomography," *Biomed. Phys. Eng. Express*, vol. 5, no. 4, 2019.

[66] S. Sjostrand, A. Widerstrom, A. R. Ahlgren, and M. Cinthio, "Design and fabrication of a conceptual arterial ultrasound phantom capable of exhibiting longitudinal wall movement," *IEEE Trans. Ultrason. Ferroelectr. Freq. Control*, vol. 64, no. 1, pp. 11–18, 2017.

[67] B. Dunmire, K. W. Beach, K. H. Labs, M. Plett, and D. E. Strandness, "Cross-beam vector Doppler ultrasound for angle-independent velocity measurements," *Ultrasound Med. Biol.*, vol. 26, no. 8, pp. 1213–1235, 2000.

[68] R. S. Reneman, T. Arts, and A. P. G. Hoeks, "Wall shear stress - An important determinant of endothelial cell function and structure - In the arterial system in vivo: Discrepancies with theory," *J. Vasc. Res.*, vol. 43, no. 3, pp. 251–269, 2006.

[69] E. W. Rogers, H. Feigenbaum, A. E. Weyman, R. W. Godley, and S. T. Vakili, "Evaluation of left coronary artery anatomy in vitro by cross-sectional echocardiography," *Circulation*, vol. 62, no. 4, pp. 782–787, 1980.

[70] C. Barfod, N. Akgören, M. Fabricius, U. Dirnagl, and M. Lauritzen, "Laser-Doppler measurements of concentration and velocity of moving blood cells in rat cerebral circulation," *Acta Physiol. Scand.*, vol. 160, no. 2, pp. 123–132, 1997.

[71] M. Jahed, F. Ghalichi, and M. Farhoudi, "Comparison of blood velocity between Transcranial Doppler and numerical method in the patient-specific Circle of Willis with aneurysm," *Biomed. Mater. Eng.*, vol. 30, no. 4, pp. 427–438, 2019.

[72] V. L. Rayz *et al.*, "Computational Modeling of Flow-Altering Surgeries in Basilar Aneurysms," *Ann. Biomed. Eng.*, vol. 43, no. 5, pp. 1210–1222, 2015.

[73] C. Roloff, D. Stucht, O. Beuing, and P. Berg, "Comparison of intracranial aneurysm flow quantification techniques: Standard PIV vs stereoscopic PIV vs tomographic PIV vs phase-contrast MRI vs CFD," *J. Neurointerv. Surg.*, vol. 11, no. 3, pp. 275–282, 2019.

[74] S. Meckel *et al.*, “In vivo visualization and analysis of 3-D hemodynamics in cerebral aneurysms with flow-sensitized 4-D MR imaging at 3 T,” *Neuroradiology*, vol. 50, no. 6, pp. 473–484, 2008.

[75] H. Isoda *et al.*, “In vivo hemodynamic analysis of intracranial aneurysms obtained by magnetic resonance fluid dynamics (MRFD) based on time-resolved three-dimensional phase-contrast MRI,” *Neuroradiology*, vol. 52, no. 10, pp. 921–928, 2010.

[76] M. C. Brindise *et al.*, “Multi-modality cerebral aneurysm haemodynamic analysis: In vivo 4D flow MRI, in vitro volumetric particle velocimetry and in silico computational fluid dynamics,” *J. R. Soc. Interface*, vol. 16, no. 158, 2019.

[77] J. N. Maraire and I. A. Awad, “Intracranial Cavernous Malformations: Lesion Behavior and Management Strategies,” *Neurosurgery*, vol. 37, no. 4, pp. 591–605, Oct. 1995.

[78] H. K. Versteeg and W. Malalasekera, *An Introduction to Computational Fluid Dynamics*, vol. 2. 2007.

[79] A. V. Souza, J. E. Ribeiro, and R. Lima, *Manufacturing Process of a Brain Aneurysm Biomodel in PDMS Using Rapid Prototyping*, vol. 34. 2019.

[80] H. J. Steiger, D. W. Liepsch, A. Poll, and H. J. Reulen, “Hemodynamic stress in terminal saccular aneurysms: A laser-doppler study,” *Heart Vessels*, vol. 4, no. 3, pp. 162–169, 1988.

[81] C. Roloff *et al.*, “Investigation of the velocity field in a full-scale model of a cerebral aneurysm,” *Int. J. Heat Fluid Flow*, vol. 43, pp. 212–219, 2013.

[82] Á. Ugron, M. I. Farinas, L. Kiss, and G. Paál, “Unsteady velocity measurements in a realistic intracranial aneurysm model,” *Exp. Fluids*, vol. 52, no. 1, pp. 37–52, 2012.

[83] F. Gaidzik, D. Stucht, C. Roloff, O. Speck, D. Thévenin, and G. Janiga, “Transient flow prediction in an idealized aneurysm geometry using data assimilation,” *Comput. Biol. Med.*, vol. 115, 2019.

[84] D. Pinho, D. Bento, J. Ribeiro, R. Lima, and M. Vaz, “An In Vitro Experimental Evaluation of the Displacement Field in an Intracranial Aneurysm Model,” *P.*

Flores, F. Viadero (Eds.), New Trends Mech. Mach. Sci. Mech. Mach. Sci. Springer Int., vol. 24, pp. 261–268, 2015.

[85] M. Matsuura, S. Tupin, and M. Ohta, "Compliance effect on the flow condition in vascular in vitro experiments," *ASME Int. Mech. Eng. Congr. Expo. Proc.*, vol. 3, pp. 1–7, 2018.

[86] A. Y. Usmani and K. Muralidhar, "Flow in an intracranial aneurysm model: effect of parent artery orientation," *J. Vis.*, vol. 21, no. 5, pp. 795–818, 2018.

[87] J. Clauser *et al.*, "A Novel Plasma-Based Fluid for Particle Image Velocimetry (PIV): In-Vitro Feasibility Study of Flow Diverter Effects in Aneurysm Model," *Ann. Biomed. Eng.*, vol. 46, no. 6, pp. 841–848, 2018.

[88] P. H. Geoghegan, N. A. Buchmann, C. J. T. Spence, S. Moore, and M. Jermy, "Fabrication of rigid and flexible refractive-index-matched flow phantoms for flow visualisation and optical flow measurements," *Exp. Fluids*, vol. 52, no. 5, pp. 1331–1347, 2012.

[89] S. H. Huang, P. Liu, A. Mokasdar, and L. Hou, "Additive manufacturing and its societal impact: A literature review," *Int. J. Adv. Manuf. Technol.*, vol. 67, no. 5–8, pp. 1191–1203, 2013.

[90] P. F. Costa *et al.*, "Mimicking arterial thrombosis in a 3D-printed microfluidic: In vitro vascular model based on computed tomography angiography data," *Lab Chip*, vol. 17, no. 16, pp. 2785–2792, 2017.

[91] R. Jewkes, H. E. Burton, and D. M. Espino, "Towards additive manufacture of functional, spline-based morphometric models of healthy and diseased coronary arteries: In vitro proof-of-concept using a porcine template," *J. Funct. Biomater.*, vol. 9, no. 15, 2018.

[92] W. Choi, J. H. Park, H. Byeon, and S. J. Lee, "Flow characteristics around a deformable stenosis under pulsatile flow condition," *Phys. Fluids*, vol. 30, no. 1, 2018.

[93] R. Yip, R. Mongrain, A. Ranga, J. Brunette, and R. Cartier, "Development of Anatomically Correct Mock-Ups of the Aorta for Piv Investigations," *Proc. Can. Eng. Educ. Assoc.*, no. 1, pp. 1–10, 2011.

[94] R. O. Rodrigues, D. Pinho, D. Bento, R. Lima, and J. Ribeiro, “Wall expansion assessment of an intracranial aneurysm model by a 3D Digital Image Correlation System,” *Measurement*, vol. 88, pp. 262–270, 2016.

[95] T. A. S. Kaufmann *et al.*, “Flow distribution during cardiopulmonary bypass in dependency on the outflow cannula positioning,” *Artif. Organs*, vol. 33, no. 11, pp. 988–992, 2009.

[96] M. H. Babiker *et al.*, “An in vitro study of pulsatile fluid dynamics in intracranial aneurysm models treated with embolic coils and flow diverters,” *IEEE Trans. Biomed. Eng.*, vol. 60, no. 4, pp. 1150–1159, 2013.

[97] M. H. Babiker *et al.*, “Influence of stent configuration on cerebral aneurysm fluid dynamics,” *J. Biomech.*, vol. 45, no. 3, pp. 440–447, 2012.

[98] M. Minakawa, I. Fukuda, J. Yamazaki, K. Fukui, H. Yanaoka, and T. Inamura, “Effect of cannula shape on aortic wall and flow turbulence: Hydrodynamic study during extracorporeal circulation in mock thoracic aorta,” *Artif. Organs*, vol. 31, no. 12, pp. 880–886, 2007.

[99] G. Porenta *et al.*, “Assessment of coronary stenoses by Doppler wires: A validation study using in vitro modeling and computer simulations,” *Ultrasound Med. Biol.*, vol. 25, no. 5, pp. 793–801, 1999.

[100] A. Victor, J. Ribeiro, and F. F. Araújo, “Study of PDMS characterization and its applications in biomedicine: A review,” *J. Mech. Eng. Biomech.*, vol. 4, no. 1, pp. 1–9, 2019.

Chapter 2

Characterization of shear strain on PDMS: Numerical and experimental approaches [1]

Abstract

Polydimethylsiloxane (PDMS) is one of the most popular elastomers and has been used in different fields, especially in biomechanics research. Among the many interesting features of this material, its hyperelastic behaviour stands out, which allows the use of PDMS in various applications, like the ones that mimic soft tissues. However, the hyperelastic behaviour is not linear and needs detailed analysis, especially the characterization of shear strain. In this work, two approaches, numerical and experimental, were proposed to characterize the effect of shear strain on PDMS. The experimental method was implemented as a simple shear testing associated with 3D digital image correlation and was made using two specimens with two thicknesses of PDMS (2 and 4 mm). A commercial finite element software (ANSYS®) was used to implement the numerical simulations, in which four different simulations using the Mooney-Rivlin, Yeoh, Gent, and Polynomial hyperelastic constitutive models were performed. These approaches showed that the maximum value of shear strain occurred in the central region of the PDMS, and higher values emerged for the 2 mm PDMS thickness. Qualitatively, in the central area of the specimen, the numerical and experimental results have similar behaviours and the values of shear strain are close. For higher values of displacement and thicknesses, the numerical simulation results move further away from experimental values.

Keywords: polydimethylsiloxane; hyperelasticity; shear strain; 3D digital correlation; numerical simulation; finite element method; hyperelastic constitutive models.

[1] Souza, A. et al., 2020. Characterization of shear strain on PDMS: Numerical and experimental approaches. Applied Sciences, Vol. 10, Issue 9, 3322.

2.1 Introduction

In recent decades, elastomers have been studied by many researchers due to their interesting characteristics, such as chemical stability, flexibility, and corrosion resistance. Among them, polydimethylsiloxane (PDMS) is one of the most studied because it has many applications in several industrial areas, from mechanics and electronics to the biomedical area, because it is an optically transparent material [1], biocompatible [2], chemically and thermally stable, highly flexible and viscoelastic [3]. PDMS has a high range of applications in mechanical sensors [4], flexible electronic components [5], electrochemical sensors [6] and the biomedical field [7] and it is also frequently found in microfluidic circuits [8], among others. In many of these applications, the elements are subjected to shear stresses, such as sealing gaskets [9], microfluidic channels [10], aneurysm studies [11], tactile sensors [12], robotics [13] and electronic components [14]. Among these, an area that recently gained significant interest was the flexible microfluids and milifluids, where it is possible to analyze the interaction between fluid and structure, which is an emerging area that may affect several areas of research, such as electronics, biology and medicine [15]. These channels are subject to shear forces. Rodrigues et al [11] carried out studies on flexible PDMS models to study the interaction between fluids (blood analog) and the structure of the intracranial aneurysm. From this study, it was found that the displacement value on the channel wall was very low, thus showing the need to determine values for shear and tensile tests for small deformations. Therefore, there is a need to study and characterize the mechanical behaviour of PDMS under shear stress action and, in this sense, research work has been developed [16,17] that refers to the implementation of tensile tests on simple lap joints associated with digital image correlation (DIC) as well as the determination of their shear modulus [18].

To characterize the mechanical behaviour of a material when it is subject to a shear loading, it is usually required to perform shear tests. Typically, shear tests were implemented using specimens that are fixed in two holding grips and incremental displacement values are applied in one of the holding grips. Usually, the main objective of this test is to determine the shear strength, which corresponds to the maximum shear stress that the material can withstand before rupture. However, in the study of materials with high elasticity, as in the case of the hyperelastic materials, there is a great interest in understanding how its deformation occurs when subjected to shear forces. In this case, it is necessary to accompany the deformation during the test before breaking visually.

Experimental optical techniques are an interesting alternative. These techniques have the advantage of accessing displacement and strain fields, are non-contact techniques, have high resolution and can use white light or laser illumination. Optical methods, such as DIC [19], geometric or interferometric Moiré [20], and speckle or holographic interferometry [21], are available with resolution up to the laser wavelength. Despite high resolution of all interferometric techniques, image decorrelation for high deformation values frequently occurs. This phenomenon usually occurs in tests of hyperelastic materials, as such, they are inadequate for studying these materials. In contrast, DIC allows the measurement of displacement and strain fields for high deformation values.

The experimental characterization of the mechanical behaviour of hyperelastic materials, when subjected to the action of shear forces, has the advantage of allowing more accurate and realistic results; however, its implementation requires laboratory facilities and costly equipment. On the other hand, there has been an exponential growth in the use of numerical tools based on the finite element method (FEM) [22,23]. The appearance of computational tools applied to hyperelastic materials is due to lower costs of the method and the increase in the calculation capacity of the computers. For numerical simulation with hyperelastic materials, it is necessary to use constitutive models that are adequate to the material under study and tensile tests (uni or biaxial) are usually required to better characterize this material [24]. Considering the advantages of each approach, both experimental and numerical, some researchers have developed hybrid methods that use experimental information in numerical simulations [25].

The purpose of this work is to characterize the mechanical behaviour of PDMS through an experimental method using 3D DIC and comparing it with four different numerical constitutive models. For this, two models with varying thicknesses of simple lap joints with PDMS were developed, and the results of the experimental tests were compared with the numerical simulation. Thus, the information contained in this work will serve to support the development of devices made in PDMS that are subject to shear loads, as for example in recent applications in flexible microfluids [15].

2.2 Numerical Constitutive Models

Currently, FEM has been used to study the mechanical behaviour of hyperelastic materials. These studies are based on mechanical models obtained from experimental

uniaxial tests. To numerically reproduce the nonlinear hyperelastic behaviour of this material, it is necessary to develop new and more accurate constitutive models. The developments of hyperelastic models are supported in two different theories, the micromechanical and macro mechanical models. Micromechanical models are developed from chemical manufacture and are based on the concept of the unit cell. The second theory, phenomenological models are based on the material behaviour observed during experimental tests. For developing these models, it is necessary to know the mechanical behaviour of the material through the experimental tensile test [26].

Hyperelastic materials are known to have a nonlinear relationship between stress and strain. Thus, hyperelastic material behaviour is usually defined based on strain energy or stored energy.

Hyperelastic materials are commonly defined as having nonlinear mechanical properties, presenting high deformation rates. The theory of hyperelastic material behaviour, also known as Green elastic material, is defined as a function of the Helmholtz free energy, also called the strain energy or stored energy (Ψ). This describes the behaviour of this class of materials in terms of mechanical energy and can be defined according to the following equation:

$$P = \frac{\partial \Psi}{\partial F} \tag{2.1}$$

or, more generally:

$$P = -pF^T + \frac{\partial \Psi}{\partial F} \tag{2.2}$$

where P is the first stress tensor of Piola-Kirchhoff, F^T is the transposed strain gradient and p is a multiple of Lagrange obtained according to the stress state T.

Helmholtz free energy (Ψ) is a thermodynamic potential that measures the useful work for a closed thermodynamic system with constant temperature and volume [27].

A model of hyperelastic materials depends on the definition of the strain energy function, which assumes different shapes, according to the material or class of materials

considered. This function is obtained from symmetry and thermodynamic energy considerations [27].

For simplicity, it is assumed that the material is isotropic and incompressible. As an isotropic material, the strain energy function (Ψ) depends on the strain invariants:

$$\Psi_{isotropic} = \Psi(I_1, I_2, I_3) \tag{2.3}$$

where the invariants are defined as:

$$I_1 = \sum_{i=1}^{3} \lambda_i^2$$

$$I_2 = \sum_{i,j=1}^{3} \lambda_i^2 \lambda_j^2 \quad i \neq j \tag{2.4}$$

$$I_3 = \prod_{i=1}^{3} \lambda_i^2$$

where λ_1, λ_2 and λ_3 are the principal strains.

If the material is too incompressible, the third invariant, I_3, is 1 and Equation 2.5 is defined as:

$$\Psi_1 = \Psi(I_1, I_2) \tag{2.5}$$

The constitutive equations of hyperelastic models are determined from the Cauchy tensor equation and the calibration of the main experimental tensile tests (uniaxial and biaxial). There are several constitutive equations for hyperelastic models, the most used models being the Yeoh, Mooney-Rivlin, Polynomial, and Gent models.

Yeoh's constitutive model is the most suitable for situations of an incompressible material, it was first presented in the early 1990s [28]. Moreover, the Yeoh model of hyperelastic materials has proved popular because it depends only on the first invariant deformation, (I1).

The Yeoh energy density function is given by [29]:

$$\Psi = \sum_{i=1}^{3} C_i \, (I_1 - 3)^i$$

(2.6)

where C_1, C_2 and C_3 are constants of the material that are determined from the experimental tests.

The Mooney-Rivlin model is one of the most known and used hyperelastic models, mainly in numerical simulations of rubbers and their derivates. This model is very widespread because it presents good convergence for a relatively large range of deformation [30].

Besides that, the classical Mooney-Rivlin stress-energy formula is used for incompressible hyperelastic materials and in the description of the behaviour of incompressible isotropic materials like soft tissue [31].

The constitutive law Mooney-Rivlin derived for hyperelastic incompressible material is described as follows [31]:

$$\Psi = C_{10}(I_1 - 3) + C_{01}(I_2 - 3) \tag{2.7}$$

where Ψ is the strain energy density function, I_1 and I_2 are the constant strain and C_{10} and C_{01} are the material constants.

The Ogden model is used to describe the nonlinear behaviour of complex materials such as rubber, polymers and biological tissues. This model is described by the following expression:

$$\Psi = \sum_{i=1}^{N} \frac{\mu_i}{\alpha_i}\left(\lambda_1^{\alpha_i} + \lambda_2^{\alpha_i} + \lambda_3^{\alpha_i} - 3\right) \tag{2.8}$$

where N is the total number of terms in the series and μ_i and α_i are material constants that can be positive, negative, integer or not.

The Polynomial model is also called the generalized Rivlin model [32,33]; this model was introduced by Rivlin & Saunders (1951). It was formulated in terms of two strain invariants, I_1 and I_2, of the left Cauchy-Green deformation tensor, with C_{ij} denoting material constants. The strain energy is given by [34]:

$$\Psi = -\frac{\mu}{2} J_m \ln\left(1 - \frac{I_1 - 3}{J_m}\right) \tag{2.9}$$

where μ is the initial shear modulus and J_m is the constant limiting value for $I_1 - 3$.

2.3 Materials and Methods

2.3.1 Experimental tests

It was necessary to manufacture two moulds in which the resin of the elastomeric polymer will be cast before polymerization to produce the tensile and shear specimens. The moulds to obtain tensile and shear specimens were manufactured in an aluminium alloy (2011-T3) by a CNC (computer numerical control) milling machine; each mould had three and two cavities for tensile and shear specimens, respectively. The geometry and dimensions of tensile specimens were chosen to match the American Society for Testing of Materials ASTM D412 TYPE C standard [35].

The polydimethylsiloxane (PDMS) used was Sylgard 184 ® from Dow Corning. To obtain the PDMS resin, it was necessary to mix the curing agent with the prepolymer; for each 10g of prepolymer, 1g of the curing agent was added (10: 1).

The mixture was placed under vacuum conditions for 40 minutes in a desiccator connected to a vacuum pump to eliminate air bubbles present in the uncured mixture. After removing all air bubbles, the mixture was poured into the tensile and shear moulds, and the moulds were placed back in the desiccator for approximately 30 minutes to ensure that all remaining bubbles were removed entirely. Was taken part of this PDMS mixture to measure the density, using the pycnometer method and was determined the value of 1059 [kg/m^3] which is very similar to other references [36].

At the end of the process, the tensile and shear moulds were taken to a temperature- and time-controlled oven, the mixture was cured at 80°C for 45 minutes. A total of 3 samples were prepared for the tensile tests and three samples for each thickness of the simple shear test.

To verify the absence of voids (bubbles), with sizes that could influence the experimental tests, a scan was made in different regions of the specimen to identify any bubbles present inside it. For this, an inverted microscope (CKX41. Olympus) with an objective lens (ZEISS, NCHROPLAN, 32X) was used. After the images obtained, the ImageJ software was used to check the bubble sizes found in the specimen, Figure 2.1 shows the microbubbles found. Through this test, it was found that the dimensions of the bubbles found were small (<5μm), not significantly influencing the results obtained in the tensile tests.

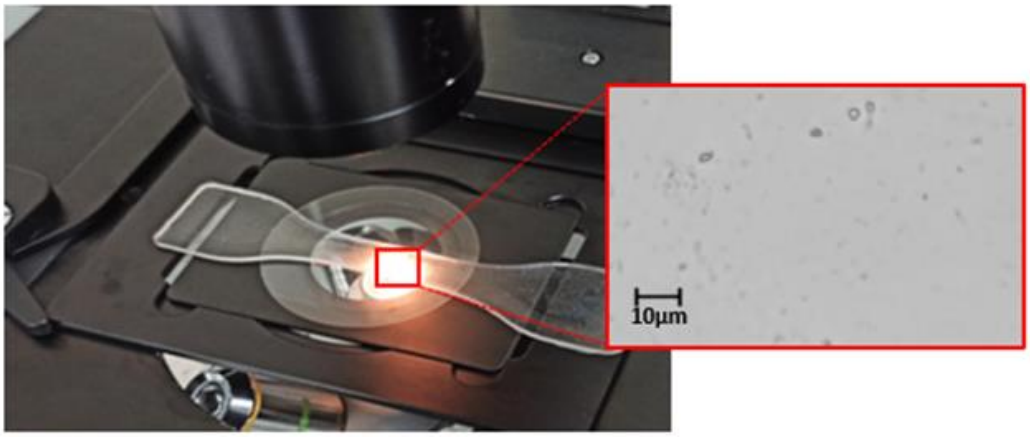

Figure 2.1 – Bubbles measurement in the specimen.

2.3.1.1 Tensile testing

Adequate deformation measurement techniques are required to identify the mechanical properties of the materials. This test aims to characterize the mechanical behaviour of the PDMS relative to the stress-strain curve and verify that it is non-linear and hyperelastic behaviour.

The tensile test was started by placing the test specimen in the holding grip on both sides of the universal INSTRON E1000 test machine, as shown in Figure 2.2 (a). The height was manually adjusted, ensuring that the test body was not drawn, that the claws were aligned, and that there was no force acting on the body. The test speed was 2mm/min. Three tensile tests were implemented and the average curve was used in the simulations, and a very similar trend was verified.

From the stress-strain curve analysis, the tested material (PDMS) has a high deformation at relatively low-stress levels (ex. 20000 Pa imposes 18.5% of strain), which corresponds to the characteristic behaviour of a hyperelastic material. Figure 2.2 (b) shows the stress-strain curve of one of the tensile tests.

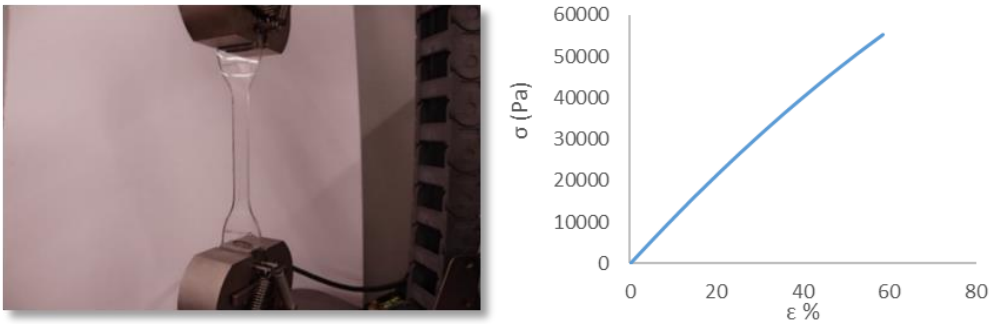

(a) **(b)**

Figure 2.2 - (a) specimen positioned on the tensile machine. (b) PDMS stress-strain curve.

The tensile test did not occur until rupture because the expected values of stress in shear tests were lower than the ultimate strength [20] and the most important reason to implement this test is to obtain the tensile stress-strain curve for use in numerical simulations of the shear test. Observing the curve shown in Figure 2.2 (b), it is possible to see the almost linear behaviour of the graph, which is not very similar to the typical hyperelastic curve; however, that curve is corroborated by other researchers [37, 38].

2.3.1.2 Shear testing

In preparing the shear test specimen, two steel (DIN-Ck45) bars with 100 x 20 x 1.5 mm^3 dimensions were used. The bars' surfaces were sanded and degreased with acetone to improve the adhesion of the PDMS to the steel. After the cleaning, the PDMS bonding was done using a cyanoacrylate structural adhesive (Locttice Super Glue 3), presenting the following configuration Figure 2.3.

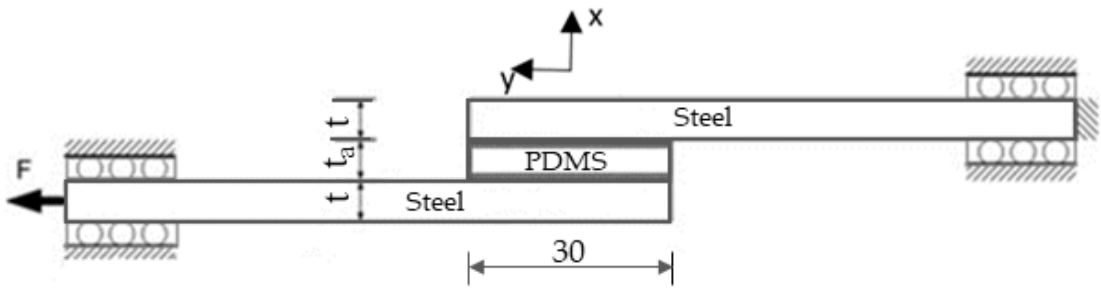

Figure 2.3 – The speciment used in the simple shear test.

The bonded region of the steel plates had a superficial treatment. The process consisted of abrading the steel plate surfaces at the overlap region with fine sandpaper and cleaning with acetone before the application of the cyanoacrylate adhesive. To control and guarantee adhesive thickness, the test specimen (single-lap joint) was manufactured in a mould. The applied cure cycle was 24h at room temperature.

For this test, two PDMS test samples with different thicknesses (2mm and 4mm) were tested. The equipment and procedure were like the tensile test, distinguished in that this test used different test pieces (simple lap joints). During the tensile test of the samples, a commercial Vic-3D (Correlated Solutions®) DIC system was used to measure the strain field in-plane and out-plane of the PDMS surface.

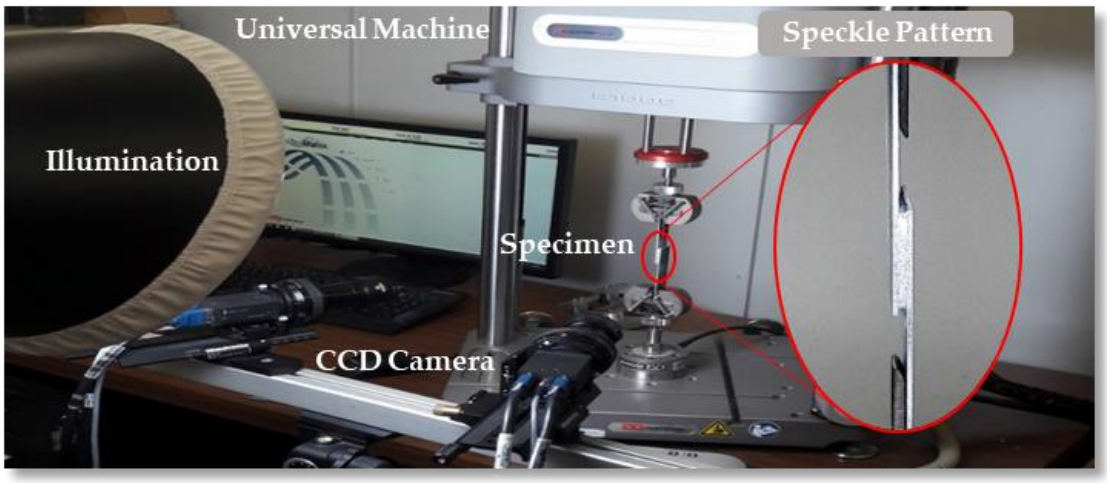

Figure 2.4 – Experimental setup of 3D Digital Image Correlation.

The DIC equipment used consisted of two high-resolution digital cameras (Point Gray GZL-CL-41C6M-C 2048 x 2048 pixels), using 80mm LINOS objective lenses, a computer with Vic- 3D and a cold lighting bulb. The experimental set up used in this assay is shown in Figure 2.4.

For a good use of the DIC method, the specimen must be covered with a speckle pattern [39]. A random speckle pattern was artificially created on the PDMS specimen surface. The speckle pattern was produced using an airbrush with an internal mixture of air and paint, connected to a low-pressure compressor. First, the specimen surface was

covered with white matte paint (the airbrush nozzle was adjusted to be approximately 0.3 meters from the specimen). After drying the first layer, a second fine layer of small black paint dots was applied with the airbrush to produce the high-contrast speckle pattern. The size and density of the speckle were defined to guarantee high fluctuation of the image intensity; thus, higher accuracy measurements could be obtained.

System calibration was done first; this procedure is necessary to provide numerical factors that will aid in the analysis of the data and to size the displacement unit. However, the calibration process of the VIC-3D system is direct and almost automatic. For 3D fields, it is necessary to use a standard calibration target, this target is positioned in front of the cameras in different positions, and several images are captured that will be used to calculate the intrinsic and extrinsic parameters of the cameras. This procedure removes distortions of the lenses and defines a three-dimensional coordinate system on the surface of the sample. These parameters will subsequently be used to determine the displacement values. The two CCD cameras were positioned at 341 millimetres and a 12.5° angulation of the specimen, and the correlation equipment was adjusted so that two photos of the sample were captured per second. Once the adjustment was made, the specimen was clamped between the universal machine claws. Two alignment guides were positioned to restrict lateral movement, thus ensuring that the deformation occurred only in the PDMS plane.

Then, the tensile test was carried out until specimen rupture occurred. The software that controls the universal test machine controlled the speed of the test (2 mm/min). The room temperature was 25°C. The DIC system was synchronized with the universal machine, the reference image was captured a few seconds before the shear test, and the cameras' triggers were initiated when the test began, at an acquisition rate of two images per second. The captured images were saved to the hard-disc of the DIC computer.

To analyse the influence of cyanoacrylate in rupture process was implemented a shear test using a similar specimen (simple overlap joint). The adherents have the same dimensions and material (steel) and the adhesive was the same type of cyanoacrylate (Locttice Super Glue 3) with a thickness of 0.3 mm. Was applied the speed test of 2mm/min and the test occurred until the rupture. Were implemented two tests.

2.3.2 Numerical Simulation

The numerical simulation was executed using a commercial finite element method (FEM) software ANSYS®.

A model with a geometry similar to the specimens, boundary conditions matching the experimental testing and a discretized domain finite element mesh were required to perform the numerical simulation. The loading and kinematic conditions were identical to those used in the experimental test. Nonlinear hyperelastic behaviours based on the constitutive models of Mooney-Rivlin, Yeoh, Polynomial and Gent were considered for the PDMS material. Many authors recommend these models for simulating PDMS materials [19,40]. The application of these models required determining several constants, which were identified from the experimental curves of the tensile tests. However, the steel bars were considered to have a linear elastic behaviour and the mechanical properties used were Young's modulus of 210 GPa and Poisson's ratio of 0.3. In the present simulation, the PLANE183 element considering the plane stress condition was used. PLANE183 is a higher-order 2-D, 8-node element with two degrees of freedom at each node and a quadratic displacement behaviour well suited for the hyperelastic application and modelling irregular meshes.

As with the previous equations, all the present constitutive models need to have specific constants and coefficients determined, and for that, the experimental stress-strain curve is used. The constants and coefficients of the material are estimated from hyperelastic curve-fitting. Figure 2.5 shows the curve-fitting for the constitutive models used in this work. The black circle represents the experimental data, and the others represent the constitutive models

The geometry of the specimen was experimentally tested to implement the numerical solution. With the same dimensions and conditions as the experimental study, the boundary conditions were the bottom edge clamped and constant displacements in the vertical direction on the upper edge of the model.

Table 2.1 presents the applied displacements in the numerical simulations for both geometries. Numerical simulation 1 corresponds to the 2mm PDMS thickness and numerical simulation 2 is 4mm PDMS thickness. The displacement values were the same that were used in experimental tests.

Table 2.1 Displacements for the numerical simulations

Numerical simulation	Displacement [mm]
1	0.5
2	0.2

For the shear-stress study, the four constitutive models presented before were used to describe the properties of the sample, Mooney-Rivlin 3 parameter, Yeoh 3rd Order, Polynomial 3rd Order, and Gent. All the models converged to a similar response.

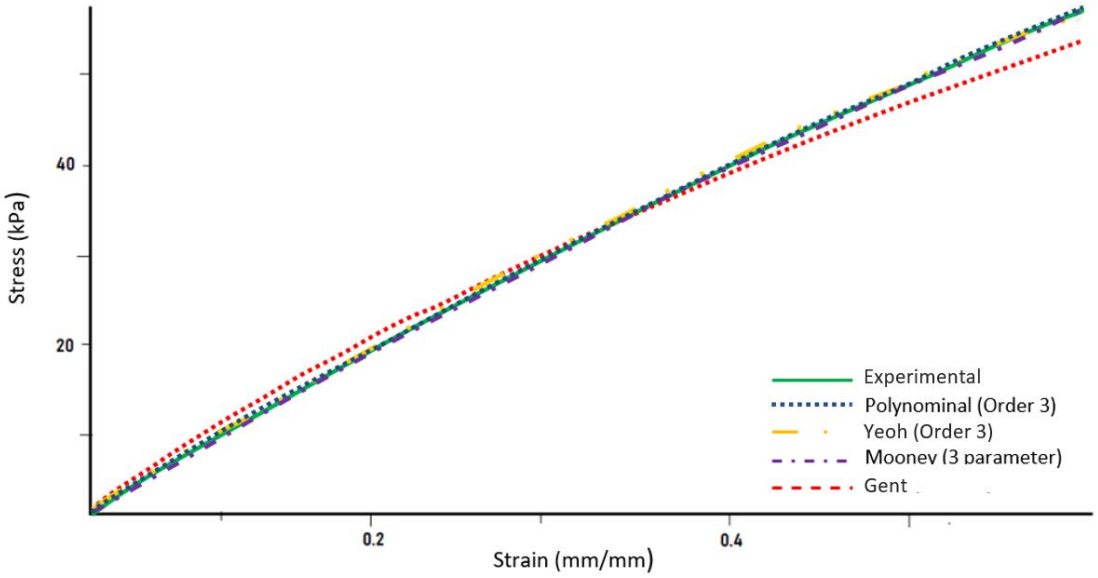

Figure 2.5 - Stress-Strain curve solution for different constitutive hyperelastic mathematical models.

For this study, as the focus is on the reaction of the central region of PDMS to the shear test, a path operation command was defined in the numerical simulation. This function makes it possible to trace a path and analyse the mechanical behaviour in a specific region. The defined path is shown in Figure 2.6, where XY shear strain was studied in both samples, on the 41 nodes selected.

The numerical simulations were used as a mesh divergence with 20 finite elements horizontally spaced equally in the PDMS region. Five different areas were created in the geometric model to obtain a better result refinement at the sample.

In the discretization of the areas adjacent to the PDMS, a 0.5 mm ratio was used for the elements to create a greater convergence in the model. The mesh has 1000 elements and 3161 nodes.

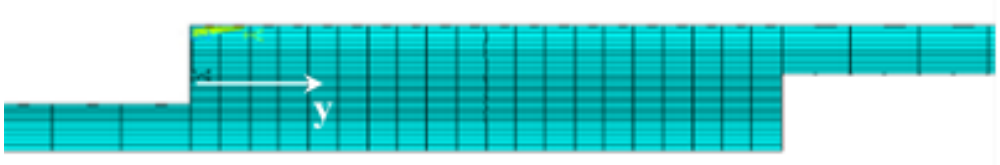

Figure 2.6 – Discretization of nodes and elements for Ansys APDL simulation.

In the analysis option, the large displacement static was chosen because the maximum number of sub-steps was defined as 150 and the minimum as 100.

It is necessary to define a convergence criterion to solve this type of nonlinear structural analysis. In the present study, convergence was met by combining the static modal forces through the Newton-Raphson method.

2.4 Results and Discussion

2.4.1 Experimental

Figure 2.7 shows the force-displacement curves obtained from the shear tests. The red line represents the results of the specimen with 4 mm PDMS thickness, and the blue one corresponds to the 2 mm thickness. From Figure 2.7, rupture of the specimen with 4 mm PDMS thickness occurred at higher values of force and displacement, 154 N and 2.8 mm, respectively. The specimen with 2 mm PDMS thickness, broke up for low values of force and displacement, 80 N and 0.8 mm, respectively. Despite the linear curve for both specimens, in the specimen with 2 mm, PDMS thickness an initial disruption happened before the complete rupture of the specimen.

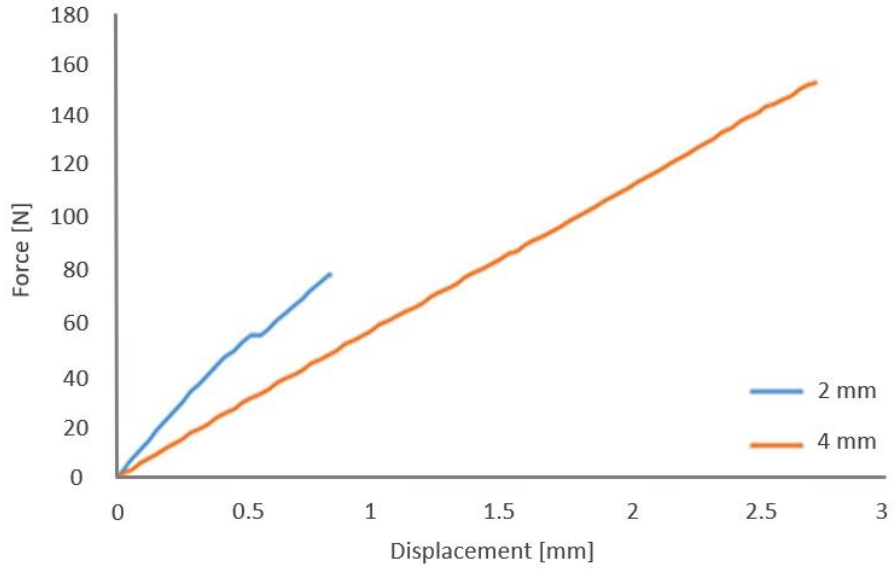

Figure 2.7 – Force displacement curve for the shear test.

Figures 2.8 and 2.9 show the details of the PDMS region of the specimens for different test phases. Figure 2.8 (a) and Figure 2.9 (a) are the images of the specimens before the deformation (reference image), Figure 2.8 (b) and Figure 2.9 (b) show the beginning of rupture and, finally, Figure 2.8 (c) and Figure 2.9 (c) present the specimen after rupture.

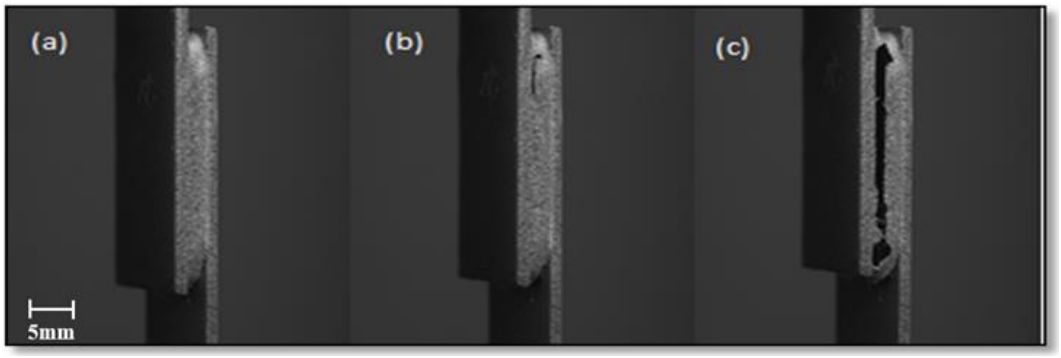

Figure 2.8 - Image of 2mm PDMS thickness: a) before deformation; b) beginning of rupture; c) after rupture.

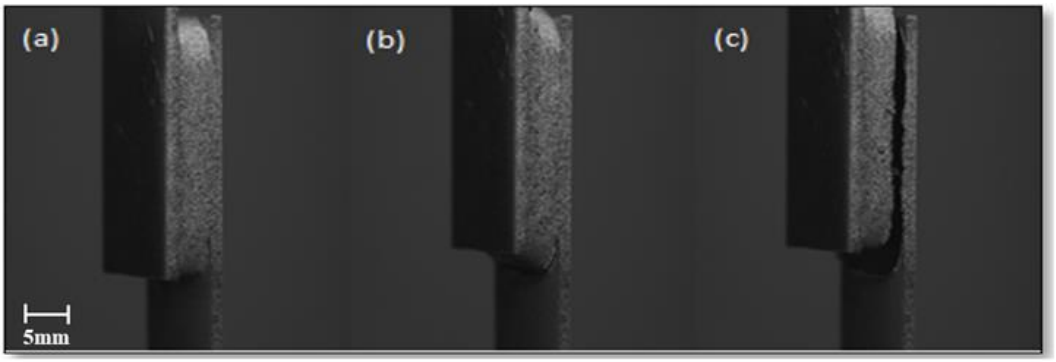

Figure 2.9 - Image of 4mm PDMS thickness: a) before deformation; b) beginning of rupture; c) after rupture.

For both specimens, the rupture happed in the interface between the metallic plate and the PDMS surface. That is, the rupture occurs in the adhesive region, which is the weakest element of the specimens. It was verified that all ruptures occurred in the interface between the PDMS and the cyanoacrylate. However, for cyanoacrylate shear tests the average of rupture force obtained was 1715 N which indicates that the cyanoacrylate strength is higher when the interface is the steel than when the interface is the PDMS. Another detail was that the rupture always happened in the PDMS surface that was in contact with air, not the surface in contact with the mould, probably because the surface roughness was lower. The authors believe that if they used a primer on the PDMS surface plate, the mechanical strength could improve. However, the goal of this work only analysed the displacement and shear strain before the rupture.

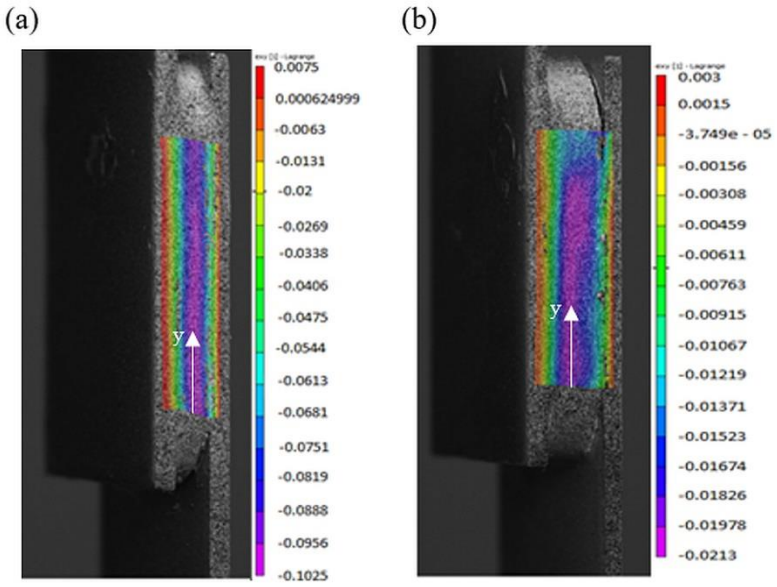

Figure 2.10 – (a) Shear strain field for a 2mm thickness PDMS plate; (b) Shear strain field for a 4mm thickness PDMS plate.

Figure 2.10 presents the shear strain field for the specimens with a 2 mm thickness PDMS plate (a) and with a 4 mm thickness PDMS plate (b). These two images were captured in two different moments of the shear test or, in other words, for two different values of displacement. Figure 2.10 (a) was obtained when the shear test reached 0.5 mm displacement, and Figure 2.10 (b) shows the shear test when the displacement value was 0.2 mm. From Figure 2.10, the maximum shear strain happened in the central region of PDMS for both thicknesses of PDMS plate. However, the maximum shear strain values are different. That is, on the specimen with the smallest thickness, the value was -0.1025 [mm/mm], while the values decreased to -0.0213 [mm/mm] for the specimen with a 4mm PDMS thickness.

2.4.1 Numerical

As previously mentioned, the four constitutive models presented were implemented in the numerical analysis. Although all the hyperelastic constitutive models present similarities in their results, it is essential to highlight the main differences. For example, Figure 2.11 shows the shear strain field determined numerically (Mooney Rivlin constitutive model) for both simulations (2 mm and 4 mm of PDMS thickness). The steel is much more rigid than PDMS, and for this reason, the values of shear strain in the steel plates are small when compared with the PDMS plate. The values of shear strain in the top and bottom of the PDMS plate are lower than in the central region due to the edge effect.

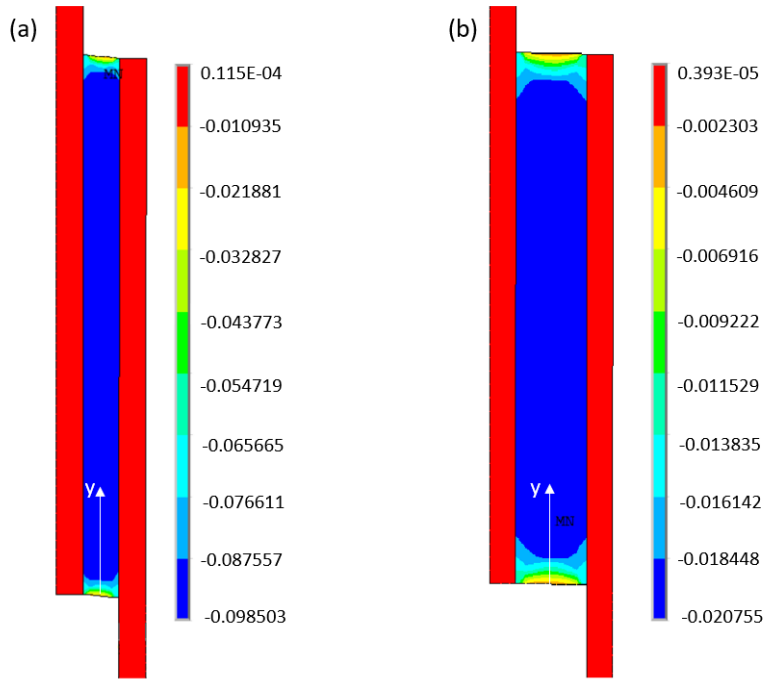

Figure 2.11 - Shear strain field obtained by numerical simulation using the Mooney Rivlin constitutive model. (a) 2mm and (b) 4mm of PDMS thickness.

Figure 2.12 shows the evolution of shear strain (Exy) along y-direction for 2 mm PDMS thickness. The average value for shear strain from the Yeoh, Polynomial, and Gent models presented the same result, -0.09680. However, the Mooney-Rivlin constitutive model resulted in -0.09684, a difference of 0.4e-3.

Figure 2.13 shows the results found of shear strain for a 4 mm thickness PDMS. The constitutive models of Yeoh, Polynomial and Gent presented the same result, -0.02060. While the Mooney-Rivlin Model gives -0.02056, again showing the same difference as the previous simulation.

The results of maximum, minimum, and average values found in the FEM simulation are shown in Table 2.2. For the simulation with 2 mm of PDMS, the highest and lowest values of shear strain were found for the Polynomial 3rd Order constitutive model.

In the case of the simulation involving 4 mm of PDMS, all constitutive models presented the same maximum and minimum value for the shear strain.

It is important to emphasize, as shown in Figure 2.5, the most suitable hyperelastic models are the Mooney-Rivlin and Polynomial models. The constitutive model of Gent

tends to move away at the end of the curve, which means that the values of shear strain found by the hyperelastic Gent model can be higher than the experimental ones, and some points are slightly above or below the experimental result at the end of the Yeoh curve. However, the results from in the Mooney-Rivlin and Polynomial hyperelastic models more adequately characterize the hyperelastic behaviour when compared with the experimental specimens. This statement is corroborated by other studies [40, 41].

Table 2.2 Average, maximum and minimum shear strain values obtained by simulation

Constitutive Model	Average	Minimum	Maximum	
Mooney-Rivlin 3 parameter	-0.09684	-0.04678	-0.10238	PDMS Thickness 2 mm
Yeoh 3rd Order	-0.09680	-0.04722	-0.10237	
Polynomial 3rd Order	-0.09680	-0.04362	-0.10514	
Gent	-0.09680	-0.04709	-0.10240	
Mooney-Rivlin 3 parameter	-0.02056	-0.00585	-0.02128	PDMS Thickness 4 mm
Yeoh 3rd Order	-0.02060	-0.00585	-0.02128	
Polynomial 3rd Order	-0.02060	-0.00585	-0.02128	
Gent	-0.02060	-0.00585	-0.02128	

2.4.2 Comparison

The comparison between the numerical and experimental results was made along the y-direction for the specimens (experimental) and the models (numerical), Figures 2.10 and 2.11, respectively. Figures 2.12 and 2.13 show that, qualitatively, the numerical and experimental results are close. However, the maximum relative error between the numerical and experimental results is very different for the two thickness values. For the 2 mm PDMS, the maximum relative error is 4.1%, and for the 4 mm thickness, it is 31.4%. This result shows that, for higher values of displacement and thicknesses, the numerical simulation results move further away from experimental values.

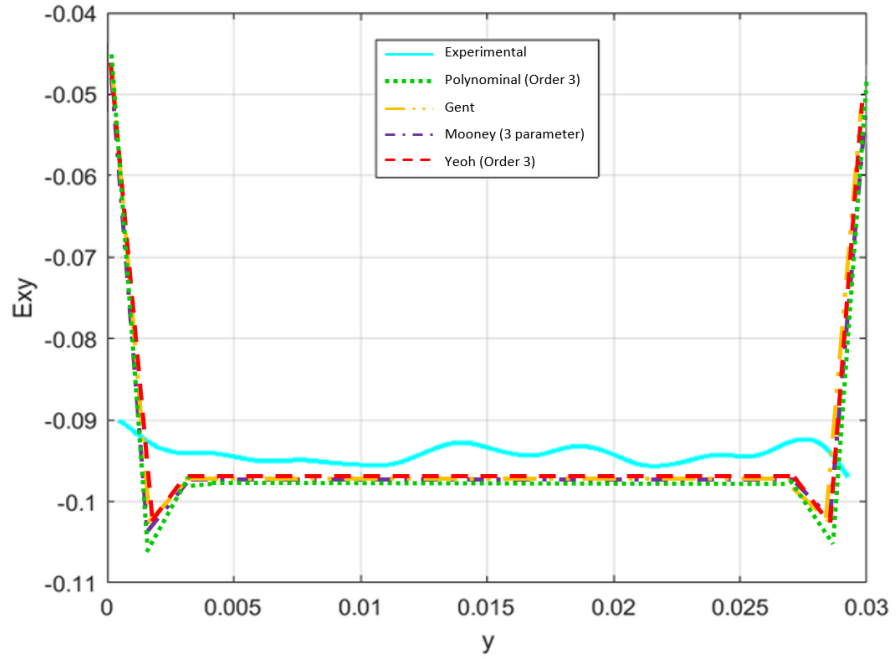

Figure 2.12 - Shear strain obtained numerically and experimentally along the y-direction for 2 mm of PDMS.

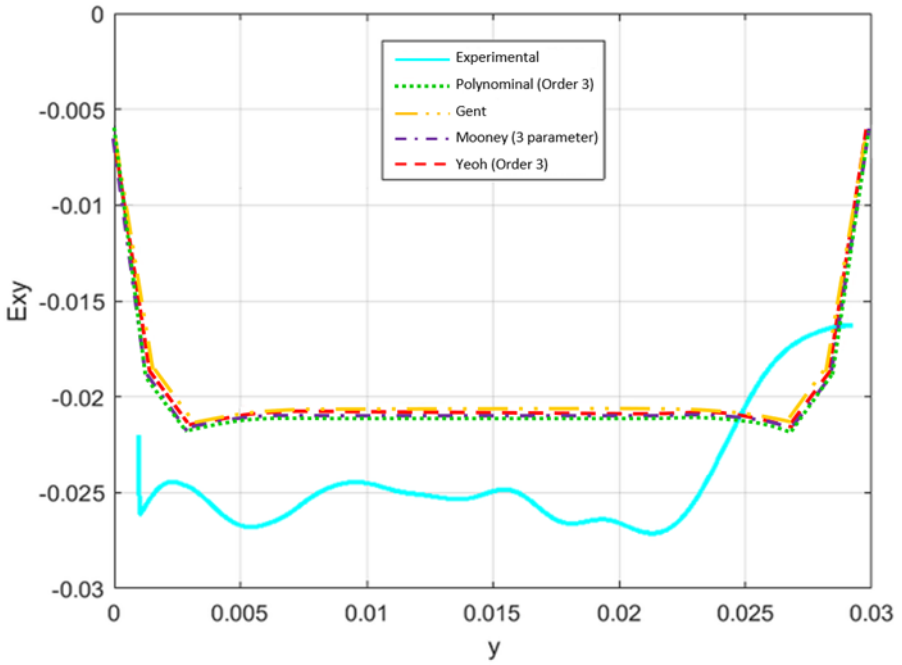

Figure 2.13 - Shear strain obtained numerically and experimentally along the y-direction for 4 mm of PDMS.

2.5 Conclusions

In this work, by the mechanical behaviour of PDMS was characterized through an experimental method associating 3D DIC and compared with numerical simulations using four different numerical constitutive models.

From experimental tests, the hyperelastic behaviour of PDMS was verified using a simple shear test. The DIC tests showed that the most significant shear strain occurred in the centre of the PDMS plate. These experimental tests also verified that the PDMS rupture occurred at the bonding interface between the steel and PDMS plates. The rupture happened for different PDMS thicknesses. For 4 mm rupture at a shear force of 80 N. For an equal value of shear force, a higher value of displacement happened for the higher PDMS thickness.

The numerical simulations were done using four hyperelastic constitutive models (Mooney-Rivlin, Yeoh, Gent and Polynomial). All the hyperelastic constitutive models presented similar results despite some critical differences. The main reason to obtain similar results in shear stress was due to the appliance of low displacement values and the constitutive models, for this displacement level, have identical behaviour. The values that show a greater difference in shear strain occurred for the Mooney-Rivlin constitutive model when compared with the other constitutive models (see Table 2). The numerical model with 2 mm of PDMS results in higher values of shear strain than with 4 mm. So, for low displacement levels is possible to use any of the hyperelastic constitutive to simulate the shear test.

Qualitatively, in the central region of the specimen, the numerical and experimental results have similar behaviour, and the values of shear strain are close. Nevertheless, the maximum relative error between the numerical and experimental results is very different for the two thickness values. It is possible to conclude that, for higher values of displacement and thicknesses, the numerical simulation results move further away from experimental values.

References

[1] Martin, S.; Bhushan, B. Transparent, wear-resistant, superhydrophobic and superoleophobic poly(dimethylsiloxane) (PDMS) surfaces. J. Coll. Int. Sci. 2017, 488, 118–126.

[2] Hassler, C.; Boretius, T.; Stieglitz, T. Polymers for neural implants. J. Polym. Sci. Part B Polym. Phys. 2011, 49, 18–33.

[3] Roh, C.; Lee, J.; Kang, C. Physical Properties of PDMS (Polydimethylsiloxane) Microfluidic Devices on Fluid Behaviors: Various Diameters and Shapes of Periodically-Embedded Microstructures. Mat. (MDPI) 2016, 9, 1–15.

[4] Kim, J.H.; Lau, K.T.; Shepherd, R.; Wu, Y.; Wallace, G.; Diamond, D. Performance characteristics of a polypyrrole modified polydimethylsiloxane (PDMS) membrane based microfluidic pump. Sens. Actua., A Phys. 2008, 148, 239–244.

[5] Lin, Y.H.; Kang, S.W.; Wu, T.Y. Fabrication of polydimethylsiloxane (PDMS) pulsating heat pipe. Appl. Therm. Eng. 2009, 29, 573–580.

[6] Casanova-Moreno, J.; To, J.; Tony Yang, C.W.; Turner, R.F.; Bizzotto, D.; Cheung, K.C. Fabricating devices with improved adhesion between PDMS and gold-patterned glass. Sens. Actua. B Chem. 2017, 246, 904–909.

[7] Jewkes, R.; Burton, H.; Espino, D. Towards Additive Manufacture of Functional, Spline-Based Morphometric Models of Healthy and Diseased Coronary Arteries: In Vitro Proof-of-Concept Using a Porcine Template. J. of Funct. Biomater. (MDPI) 2018, 9, 1–17.

[8] Teixeira, A.; Hernández-Rodríguez, J.; Wu, L.; Oliveira, K.; Kant, K.; Piairo, P.; Diéguez, L.; Abalde-Cela, S. Microfluidics-Driven Fabrication of a Low Cost and Ultrasensitive SERS-Based Paper Biosensor. Appl. Scien. (MDPI) 2019, 9, 1–14.

[9] Farfán-Cabrera, L.I.; Pascual-Francisco, J.B.; Gallardo-Hernández, E.A.; Susarrey-Huerta, O. Application of digital image correlation technique to evaluate creep degradation of sealing elastomers due to exposure to fluids. Polym. Test. 2018, 65, 134–141.

[10] Bashirzadeh, Y.; Qian, S.; Maruthamuthu, V. Non-intrusive measurement of wall

shear stress in flow channels. Sens. Actua. A. Phys. 2018, 271, 118–123.

[11] Rodrigues, R.O.; Pinho, D.; Bento, D.; Lima, R.; Ribeiro, J. Wall expansion assessment of an intracranial aneurysm model by a 3D Digital Image Correlation System. Measur. 2016, 88, 262–270.

[12] Huang, Y.M.; Tsai, N.C.; Lai, J.Y. Development of tactile sensors for simultaneous, detection of normal and shear stresses. Sens. Actua. A Phys. 2010, 159, 189–195.

[13] Unver, O.; Uneri, A.; Aydemir, A.; Sitti, M. Geckobot: A gecko inspired climbing robot using elastomer adhesives. Proc. - IEEE Int. Conf. Robot. Autom. 2006, 2006, 2329–2335.

[14] Xu, F.; Li, X.; Shi, Y.; Li, L.; Wang, W.; He L.; Liu, R. Recent Developments for Flexible Pressure Sensors: A Review. Micromach. (MDPI) 2018, 9, 1-17.

[15] Fallahi, H.; Zhang, J.; Phan, H.-P.; Nguyen, N.-T. Flexible Microfluidics: Fundamentals, Recent Developments, and Applications. Micromachines 2019, 10, 830.

[16] Banea, M.; Silva, L. The effect of temperature on the mechanical properties of adhesives for the automotive industry. Proceed. of the Instit. of Mecha. Engi. Part L J. of Mat. Des. and Applic. 2010, 224, 51-62.

[17] Moreira, D.; Nunes, L. Comparison of simple and pure shear for an incompressible isotropic hyperelastic material under large deformation. Polym. Test. 2013, 32, 240–248.

[18] Nunes, L.S. Shear modulus estimation of the polymer polydimethylsiloxane (PDMS) using digital image correlation. Mater. Des. 2010, 31, 583–588.

[19] Nunes, L.S. Mechanical characterization of hyperelastic polydimethylsiloxane by simple shear test. Mater. Sci. Eng. A 2011, 528, 1799–1804.

[20] Post, D.; Han, B.; Ifju, P. High Sensitivity Moiré: Experimental Analysis for Mechanics and Materials. Springer Verlag, Berlin 1997, ISBN 978-1-4612-4334-2.

[21] Wang, Y.; Gao, X.; Xie, X.; Wu, S.; Liu, Y.; Yang, L. Simultaneous dual

directional strain measurement using spatial phase-shift digital shearography. Opt. and Las. in Engin. 2016, 87, 197-203.

[22] Ribeiro, J.; Fernandes, C.S.; Lima, R. Numerical Simulation of Hyperelastic Behaviour in Aneurysm Models. Lecture Notes in Computational Vision and Biomechanics 2017, Springer, 937–944.

[23] Xue, L.; Pham, J.T.; Iturri, J.; Del Campo, A. Stick-Slip Friction of PDMS Surfaces for Bioinspired Adhesives. Lang. 2016, 32, 2428-2435.

[24] Besson, J.; Cailetaud, G.; Chaboche, J.; Forest, S.; Blétry, M. Non-Linear Mechanics of Materials. Springer, London, 2010.

[25] Ribeiro, J.; Lopes, H.; Martins, P. A hybrid method to characterize the mechanical behaviour of biological hyperelastic tissues. Comp. Meth. Biomech. and Biomed.: Eng. Imag. &Visual. 2017, 5,157–164.

[26] Holzapfel, G. Nonlinear Solid Mechanics: A Continuum Approach for Engineering. John Wiley & Sons, LTD, New York, 2000, ISBN: 978-0-471-82319-3.

[27] Wriggers, P. Nonlinear Finite Element Methods. Springer-Verlag, Berlin, 2008, ISBN: 978-3-540-71000-4.

[28] Yeoh, O.H. Some forms of the strain energy function for rubber. Rubber Chem. Technol. 1993, 66, 754–771.

[29] Bhowmick, A.K. Rubber products manufacturing technology. CRC Press, New York, 1994, ISBN: 9780824791124.

[30] Guo, Z.; Sluys, J. Application of a new constitutive model for the description of rubber-like materials under monotonic loading. Int. J. of Sol. and Struct. 2006, 43, 2799–2819.

[31] Proulx, T. Mechanics of Biological Systems and Materials. Proceed. Ann. Conf. on Experi. and App. Mech. 2011, 2. Springer Science & Business Media, ISBN: 9781461402183.

[32] Laksari, K.; Shafieian, M.; Darvish, K. Constitutive model for brain tissue under finite compression. J. Biomech. 2012, 45, 642–646.

[33] Hartmann, S.; Neff, P. Polyconvexity of generalized polynomial-type hyperelastic strain energy functions for near-incompressibility. Int. J. of Soli. and Strut. 2003, 40, 2767-2791.

[34] Ritto T.G.; Nunes, L.S. Bayesian model selection of hyperelastic models for simple and pure shear at large deformations. Comput. & Struct. 2015, 156, 101–109.

[35] ASTM D412-0:2011, "Standard Test Methods for Vulcanized Rubber and Thermoplastic Elastomers—Tension", 2016.

[36] López, M.; Rubio, M.; Sadek, S.H., Veja, E.J. A simple emulsification technique for the production of micro-sized flexible powder of polydimethylsiloxane (PDMS). Pow. Tecnh. 2020, 306, 610-616.

[37] Johnston I.D.; McCluskey, D.K.; Tan C.K.; Tracey M.C. Mechanical characterization of bulk Sylgard 184 for microfluidics and microengineering. J. Micromech. Microeng. 2014, 24, 035017 (7pp).

[38] Schneider F.; Lellner T.; Wilde J.; Wallrabe U. Mechanical properties of silicones for MEMS. J. Micromech. Microeng. 2008, 18, 065008 (9pp).

[39] Zhang, J.; Sweedy, A.; Gitzhofer, F.; Baroud, G. A novel method for repeatedly generating speckle patterns used in digital image correlation. Opt. Las. Eng. 2018, 100, 259–266.

[40] Cardoso, C.; Fernandes, C.; Lima, R.; Ribeiro, J. Biomechanical analysis of PDMS channels using different hyperelastic numerical constitutive models. Mech. Resea. Commun. 2018, 90, 26-33.

[41] Ribeiro, J.; Lopes, H.; Martins, P.; César, M.B. Mechanical analysis of PDMS material using biaxial test. AIMS Mate. Scie. 2019, 6, 97-110.

Chapter 3

Manufacturing process of a brain aneurysm bio model in PDMS using rapid prototyping [1]

Abstract

Cerebral aneurysm is an abnormal dilatation of the blood vessel into a saccular form. They can originate in congenital defects, weakening of the arterial wall with increasing age, atherosclerotic changes, trauma and infectious emboli.

The in vivo experiments are an effective way of investigating the appearance, validating new practices and techniques, but beyond ethical issues, these types of experiments are expensive and have low reproducibility. Thus, to better understand the pathophysiological and geometric aspects of an aneurysm, it is important to fabricate in vitro models capable of improving existing endovascular treatments, developing and validating theoretical and computational models. Another difficulty is in the preoperative period of the non-ruptured cerebral aneurysm, known for the success of the skilled acts because there is an anatomical structure of the aneurysm as its current position. Although there are technologies that facilitate three-dimensional video visualization in the case of aneurysms with complex geometries the operative planning is still complicated, so the development of the real three-dimensional physical model becomes advantageous. In this work, the entire process of manufacturing an aneurysm biomodel using polydimethylsiloxane (PDMS) is disassembled by rapid prototyping technology. The manufactured biomodels are able to perform different hemodynamic studies, validate theoretical data, numerical simulations and assist in the preoperative planning.

Keywords: PDMS biomodels; cerebral aneurysm; in vitro models.

[1] Souza, A. et al., 2019.Manufacturing process of a brain aneurysm biomodel in PDMS using rapid prototyping. VipIMAGE 2019. Lecture Notes in Computational Vision and Biomechanics, vol 34. Springer, Cham

3.1 Introduction

Cerebral aneurysm or intracranial aneurysm is the abnormal dilatation of the blood vessel in a saccular form [1]. It may originate in congenital defects, weakening of the arterial wall with increasing age [2], atherosclerotic changes, trauma and infectious emboli. Other factors may be related to the onset of the aneurysm, such as hypertension, smoking, and excessive alcohol use. It is estimated that intracranial aneurysm occurs in 2.6% of the population and the cause of 85% of subarachnoid hemorrhage is the rupture of a saccular intracranial aneurysm [3].

In vivo experimental methods are an effective way to validate new practices and techniques for diseases such as the aneurysm, but in addition to ethical issues, these kinds of experiments are expensive and have low reproductively [4]. Thus, in order to better understand the pathophysiological and geometric aspects of an aneurysm, it is important to manufacture *in vitro* models to improve existing endovascular treatments and to develop and validate theoretical and computational models [5-6].

Recently Pinho et al developed a model with geometry and dimensions based on clinical data of a common saccular intracranial aneurism. The model was fabricated with the help of a 3D printer and produced with the polydimethylsiloxane (PDMS) which is a biocompatible material [7]. The PDMS has an elastic behavior similar to arteries [8] and with numerous applications in biomedical [9-16]. The model was subsequently subjected to different experimental tests and numerical simulations [2,17].

In order to improve the existing model, in this work we propose a novel process of manufacturing a cerebral aneurysm biomodel obtained through an angiography. The image was processed by means of the Scanlp software and the mould was obtained by a three-dimensional printing process (TDP) combined with a PDMS gravity casting process. The biomodel fabricated in this work allows the performance of different hemodynamic studies, test different aneurysm repair techniques and validate numerical approaches.

3.2 Manufacturing Process

The first process used to obtain the biomodel of the cerebral aneurysm was the angiography of the anatomical zone where the aneurysm is located. For the image

treatment, it was performed the segmentation of the image with the objective to isolate the internal carotid artery from the other structures presented in the imaging examination.

The software used was Scanlp, which read and import the angiography images, translating to DICOM (Digital Imaging and Communications in Medicine) format, allowing the visualization of the 3D image. In order to isolate the structure of interest, we used the technique of binarization (Thresholding) and the thickness of the layer (Thickness layer) was 0.0889. Note that, it was the smallest available thickness and as a result it was obtained the best possible precision. In Figure 3.1 we can visualize the image after this treatment step.

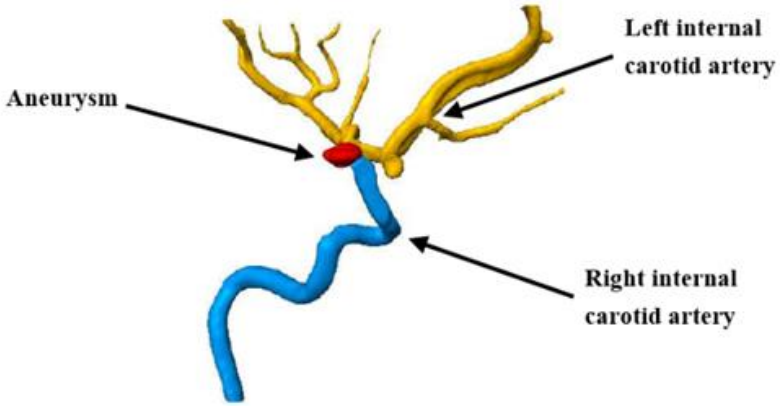

Figure 3.1 – Mask image processing step.

Finally, a mask was applied to the aneurysm and arteries. After this procedure the images were converted to STL format. The 3D model has been converted to sli. (slice) to be laminated into thin slices parallel to each other and perpendicular to the Z axis. The file was generated and sent to the three-dimensional printer.

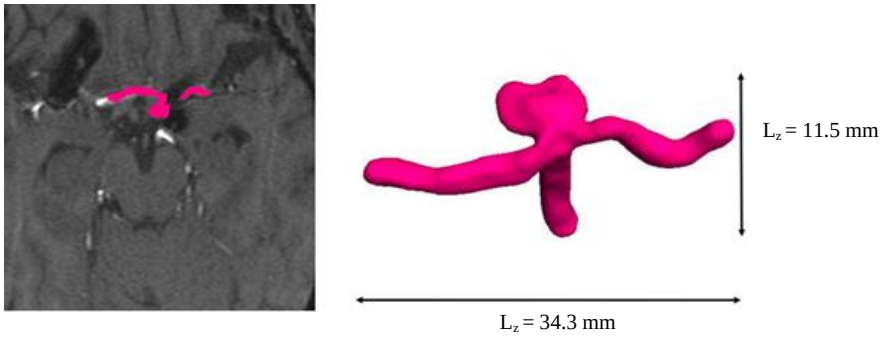

Figure 3.2 – Final model of the aneurysm.

3.3 Rapid Prototyping

Rapid Prototyping (RP) is a technology that builds physical structures layer by layer from a virtual model, these structures can be made of various materials and for a range of applications. This technology was initially developed for the manufacturing industry, designing components for automobiles, aircraft and computers. rapid prototyping was primarily used in the field of medicine in 1990 when a model of cranial bone anatomy was produced demonstrating complete internal details with computed tomography image data [18]. At the present moment, industrial and academic interest in three-dimensional (3D) prints has grown and 3D-printed products have been gaining space in pre-surgical planning and operative use [19].

In this study, this technology was used to generate the physical model of the aneurysm, manufactured by using the 3DSystems ProJet 1200 printer (3DSystems, USA). This 3D printer prints with a Visijet FTX Green cartridge, making it possible to obtain a aneurysm model with a good surface roughness.

Figure 3.3 – (a) STL format; (b) 3D Systems ProJet 1200 printer; (c) Mold matrix Visijet FTX Green.

3.4 *In Vitro* PDMS Biomodel

After obtaining the wax physical model, we have prepared 10:1 PDMS, i.e., 10 grams of the base polymer correspond to 1 gram of the curing agent. After, performing the mixture, it was used a vacuum pump for remove the bubbles and subsequently the liquid was poured into the mold by means of a gravity casting process. The curing process was performed at room temperature for about 24 hours. After this period the mold was placed in pure acetone and the matrix was removed, obtaining at the end the final biomodel as shown in Figure 3.4.

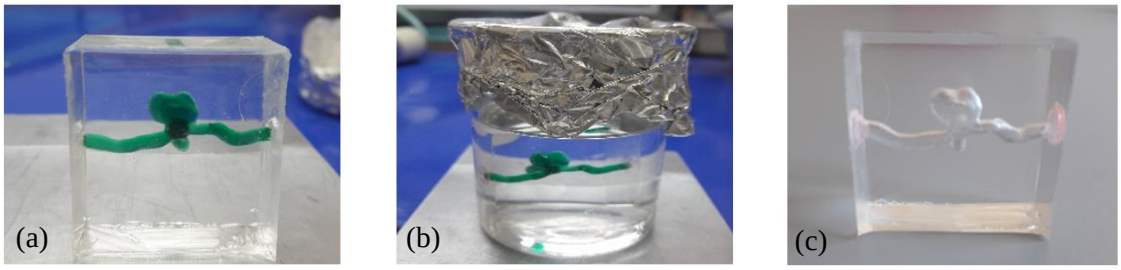

Figure 3.4- Biomodel in PDMS; (b) Biomodel immersed in pure acetone; (c) Final PDMS biomodel with a cerebral aneurism to perform fluid and pre-clinical experiments.

3.5 Conclusions

One of the major difficulties affecting the long-term success of aneurysm repair is the migration of the graft (stent), which may generate internal leakage and even rupture. To avoid this phenomenon and other problems related to the aneurysm treatment, there is the need to perform different kinds of tests, in order to improve techniques and materials, which are very difficult to be carried out in vivo due to the difficulty related to the organs authorization, high costs and reproducibility. The low cost of the *in vitro* model manufacturing process proposed in this study aims to help and simplify the tests in aneurysms. This process is a simple method able to replicate different configurations of aneurysms, which can be used not only for medical and preoperative diagnosis but also to perform in vitro flow experiments to validate and improve existent numerical models.

References

[1] Rodriguez-Régent C (2014) Non-invasive diagnosis of intracranial aneurysms. Diagn. Interv. Imaging 95: 1163–1174.

[2] Cardoso C, Fernandes CS, Lima R, Ribeiro J (2018) Biomechanical analysis of PDMS channels using different hyperelastic numerical constitutive models. Mech. Res. Commun 90: 26–33.

[3] Sathyan S (2014) Association of Versican (VCAN) gene polymorphisms rs251124 and rs2287926 (G428D), with intracranial aneurysm. Meta Gene 2: 651–660.

[4] Bosman WMPF (2010) Aortic customize: An in vivo feasibility study of a percutaneous technique for the repair of aortic aneurysms using injectable elastomer. Eur. J. Vasc. Endovasc. Surg 40: 65–70.

[5] Bosman WMPF(2010) The effect of injectable biocompatible elastomer (PDMS) on the strength of the proximal fixation of endovascular aneurysm repair grafts: An in vitro study. J. Vasc. Surg 52: 152–158.

[6] Nam SW, Choi S, Cheong Y, Kim YH, Park HK (2015) Evaluation of aneurysm-associated wall shear stress related to morphological variations of circle of Willis using a microfluidic device. J. Biomech 48: 348–353.

[7] Hassler C, Boretius T, Stieglitz T, (2011) Polymers for neural implants," J. Polym. Sci. Part B Polym. Phys 49: 18–33.

[8] Lima R (2008) In vitro blood flow in a rectangular PDMS microchannel: Experimental observations using a confocal micro-PIV system," Biomed. Microdevices 10: 153–167.

[9] Maitz MF (2015) Applications of synthetic polymers in clinical medicine. Biosurface and Biotribology 1: 161–176.

[10] Unger MA, Chou HP, Thorsen T, Scherer A, Quake SR (2000) Monolithic microfabricated valves and pumps by multilayer soft lithography. Science 288: 113–6.

[11] Bozukova D, Pagnoulle C, Jérôme R, Jérôme C (2010) Polymers in modern ophthalmic implants - Historical background and recent advances. Mater. Sci. Eng. R Reports 69: 63–83.

[12] Wang W, Fang J (2007) Variable focusing microlens chip for potential sensing applications. IEEE Sens. J 7: 11–17.

[13] Faustino V., Catarino S. O., Lima R. and Minas G., (2016) "Biomedical microfluidic devices by using low-cost fabrication techniques: A review", Journal of Biomechanics 49 (11), 2280–2292.

[14] Muñoz-Sánchez B. N:, Silva S. F., Pinho D., Vega E. J., and Lima R. (2016) "Generation of micro-sized PDMS particles by a flow focusing technique for biomicrofluidics applications" Biomicrofluidics 10, 014122.

[15] Pinho, D., Campo-Deano L., Lima R., Pinho F.T., (2017) "In vitro particulate analogue fluids for experimental studies of rheological and hemorheological behavior of glucose-rich RBCs suspensions", Biomicrofluidics. 11 (5), 054105.

[16] Bento, D., Rodrigues, R., Faustino, V., Pinho, D., Fernandes, C., Pereira, A., Garcia, V., Miranda, J., and Lima, R., (2018) "Deformation of Red Blood Cells, Air Bubbles, and Droplets in Microfluidic Devices: Flow Visualizations and Measurements." Micromachines, 9, 151.

[17] Rodrigues RO, Pinho D, Bento D, Lima R, Ribeiro J (2016) Wall expansion assessment of an intracranial aneurysm model by a 3D Digital Image Correlation System. Measurement 88: 262–270.

[18] Kim MS, Hansgen AR, Wink O, Quaife RA, Carroll JD (2008) Rapid prototyping: A new tool in understanding and treating structural heart disease. Circulation 117: 2388–2394.

[19] Jakus AE, Rutz AL, Shah RN (2016) Advancing the field of 3D biomaterial printing. Biomed. Mater 11: 14102.

Chapter 4

3D Manufacturing of intracranial aneurysm biomodels for flow visualizations: a low cost fabrication process [1]

Abstract

There is a continuous search for better and more complete *in vitro* models with mechanical properties closer to *in vivo* conditions. In this work a manufacturing process, based on a lost core casting technique, is herein reported to produce aneurysm biomodels to perform experimental hemodynamic studies. By using real artery images combined with a lost core casting technique, three materials were tested: paraffin, beeswax and glycerin-based soap. All *in vitro* biomodels were compared according to their transparency and final structure. Additionally, comparisons between experimental and numerical flow studies were also performed. The results have shown that the biomodels produced with beeswax and glycerine-based soap were the most suitable in vitro models to perform direct flow visualizations of particulate blood analogue fluids. The biomodels proposed in this works, have the potential to provide further insights into the complex blood flow phenomena happening at different kinds of pathologies and answer to important hemodynamics questions that otherwise cannot be tackled with the existing in vitro models.

Keywords: intercranial aneurysm; biomodels; manufacturing; experimental mechanics; numerical simulation

[1] Souza, A. et al., 2020. 3D Manufacturing of intracranial aneurysm biomodels for flow visualizations: a low cost fabrication process. Mechanics Research Communications Journal. Volume 107, July 2020.

4.1 Introduction

Intracranial aneurysm (IA) is an abnormal dilation of a cerebral blood vessel resulting usually in a saccular form [1]. Its rupture affects 2.6% of the population and it is the cause of 85% of subarachnoid hemorrhage. Although the scientific community commonly agrees that the main cause of IA onset is the weakening of the brain wall [2], the biological, physiological and biomechanical characteristics behind this weakening are still unknown [3]. Congenital disabilities such as aging, atherosclerotic changes, trauma, and infectious emboli may be the likely causes of this weakening [4]. Other factors related to the onset of the aneurysm are hypertension, smoking, and abuse of alcohol [5]. Moreover, internal blood flow pressure can also have an important effect on aneurysm rupture [6]. Kristian Valen-Sendstad et al. [7], using an IA, have demonstrated by direct numerical simulation that turbulence in blood flow increases the wall shear stresses to their maximum values.

The study of aneurysm local hemodynamics is crucial to understanding their growth and complications. It will help in the postoperative period and in the development of new treatment techniques [8]. As stated by previous research reports, introducing a stentimay distort local hemodynamics and their impact should be understood [9,10]. For this reason, it is common to use different experimental approaches such as numerical, *in vivo* and *in vitro*. Numerical studies always require experimental validation. On the other hand, *in vivo* testing is very efficient, but it is enormously costly and involves ethical and reproducibility issues [11]. Finally, the use of *in vitro* experimental techniques may overcome the issues set by the previous approaches. Manufacturing biomodels, which reproduce with high accuracy the arterial geometries, will allow experimental studies of fluid dynamics. This is mandatory to improve the clinical understanding of aneurysm growth, assisting in the preoperative treatment or improving the existing endovascular treatments.

Biomodeling is the ability to transform biological models into real solid models using rapid prototyping (RP). This technology has been applied in IA since 1999, D'Urso et al. [12] constructed ABS solid biomodels of intracranial aneurysms to prove its viability to help in surgical planning.With the passage of time, this technique has been optimized, applying different materials and 3D printing techniques [13-17]. The biomodels have become flexible, hollow and anatomically closer to reality [18-21]. Nowadays, they are effective in assisting surgery, by reducing surgical time and the risk

of death [22,23]. Nevertheless, they face serious limitations for the case of hemodynamic studies. As visualizing the inner flow is imperative, they must be transparent to white light, its thickness should be less than the focal length of the objective used for experimental testing [24] and the used material must have a refractive index as closest as possible to the fluid one [25].

Many researchers have developed *in vitro* techniques to enable experimental studies of blood flow in realistic configurations using direct rapid prototyping [26,27] or in the manufacture of negative molds [24,28]. However, it is difficult to choose the sacrificial mold material or to remove it, if one manufactures blood vessel biomodels using negative molds [25]. The coating properties can be changed in high melting point materials. Some of them leave debris on the channel wall (cerrolow [29]) or have restrictions on small diameters (wax [30]). Although wax and cerrolow are the most widely used materials, there are several studies with other different materials such as isomalt [30], gelatin [25], chocolate [31], and melted sucrose [24].

In this paper, it is described the manufacturing process for creating and replicating biomodels of an intracranial aneurysm in a millimeter scale range. The models were produced with different molding materials (paraffin, beeswax and glycerine-based soap), through lost core casting as the models must be suitable to conduct fluid flow analyses, the 3D fabricated core molds were coated with an optically transparent material (polydimethylsiloxane (PDMS)). This material is widely used in the construction of channels for hemodynamic studies [32,33]. Then the molds were removed increasing the temperature (paraffin), mechanically (beeswax) or by means of a water solution at ambient temperature (glycerine-based soap). Moreover, the quality of the manufactured PDMS biomodels was assessed dimensionally, optically and numerically. The model dimensions were measured and compared against the STL (stereolithography) format. Then, the transparency of three biomodels manufactured through different molds was tested. Finally, a numerical simulation employing CFD (Computational Fluid Dynamics) was conducted and the fluid particles trajectories were obtained. These ones were compared with experimental ones by visualizing injected PMMA (polymethylmethacrylate) particles in the biomodel.

4.2 Materials and Methods

As we have just mentioned our main objective is to manufacture an IA PDMS biomodel suitable for flow analysis. This biomodel is subjected to several restrictions:

1) Dimensions: The channels of the biomodel must reproduce the curves and surfaces of the real artery.

2) Optics: The manufacturing material must be transparent and its refractive index should be similar to the fluid used in the experiments.

3) Lost core material: Its geometry must match the STL geometry and it must be easily removable to avoid the presence of residuals in the biomodel.

4) Reproducibility: The manufacturing process should allow to build biomodels without any dimensional discrepancies.

We have imposed a final restriction using low cost materials and employing affordable processes in order reduce expenses and be economically viable.

A summary of the manufacturing process it is as follows: A set of angiographic medical images were acquired in the Hospital, then images were segmented with the ScanIP software from the company Synopsys® and a digital model of the aneurysm in STL format was obtained. This STL file was sent for prototyping stereolithography and a resin model was built. A bipartite silicone mold was produced using this model. Finally, that mold was used as cavity for three lost core materials: paraffin, beeswax and glycerin-based soap, which were destroyed at the end of the process. PDMS silicone is introduced as a final coating, giving rise to the transparent biomodel.

The whole process allowed us to construct IA biomodels on the real scale. We also manufactured them in a 30% reduced scale. This step is necessary as we needed to test if the sacrifice materials were viable to manufacture smaller diameter channels and to allow different visualization tests in optical microscopes. The following sections describe in detail the mentioned stages of the manufacturing process for IA PDMS biomodels.

4.2.1 Obtaining the digital model

Typical procedures to get non-invasive anatomical information for aneurysm are angiography, computed tomography or magnetic resonance. In this work, the anatomical area where the aneurysm is located was acquired by an angiography. The obtained images were imported using the software Scan IP and translated into DICOM (Digital Imaging and Communications in Medicine) format. The thresholding technique was employed to identify the different structures of interest. These structures were labeled with four colors. (Figure 4.1 a) shows the aneurysm and several arteries. The right internal carotid artery (ICA)-R, its branches and the aneurysm were isolated from other structures (Figure 4.1 b). Then it was cut along with the anterior cerebral artery (ACA) and middle cerebral artery (MCA), (Figure 4.1 c). Finally, the obtained model was transformed into STL format (Figure 4.1 d).

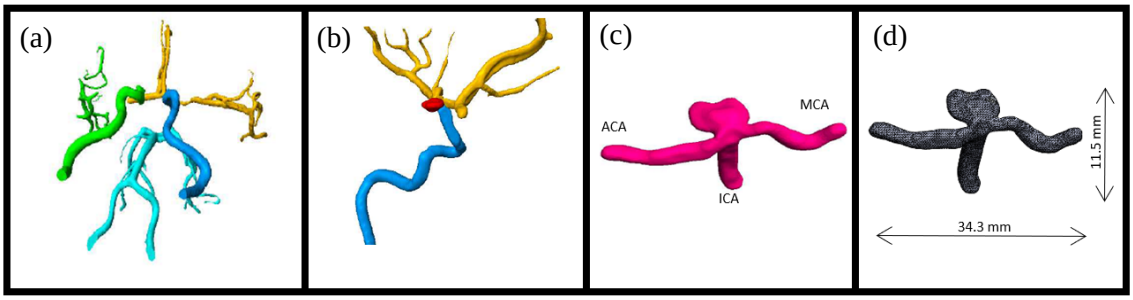

Figure 4.1 - Segmentation process of the arteries with an aneurysm to obtain the digital model. (a) Willys circle arteries; (b) aneurysm location; (c) vascular aneurysm anatomy obtained; (d) final aneurysm STL model.

4.2.2 Rapid prototyping of the 3D aneurysm mold

3D printing is capable of use different materials to produce molds, such as ABS, PLA, PVA, plaster powder, among others. However, latter changes in the mold geometry and its subsequent influence in the dimensions must be avoided. VisiJet FTX was chosen to prevent additional surface treatment with sandpaper, acetone, glue or varnishes. This material has a good surface finish, strength and can also be used directly as a sacrificial core [27].

Once the printing material was chosen, STL files were transferred to the 3D printer (ProJet 1200) and the master mold was printed by stereolithography. In this process, the printer uses a liquid photopolymer resin, which can be epoxy or acrylic and it is polymerized with the action of ultraviolet light or laser. The specifications of the 3D printer used are given in Table 4.1.

Table 4.1 Rapid prototyping specifications for the stereolithografy process

ProJet 1200	
Net Build Volume (xyz)	43x 27 x 150mm
Native Resolution (xy)	56 micron
Layer Thickness	0.03 mm
Vertical Build Speed up to	14mm/hour
Post-processing	Bult-in UV Curing Station

The master molds obtained, with real dimensions and 30% scale reduction, were used to construct the bipartite silicone mold that will be used to model the lost core materials of paraffin, beeswax and glycerine-based soap, as we can see in Figure 4.2.

Figure 4.2 - Models obtained by rapid prototyping and lost wax. (a) model obtained by rapid prototyping of VisiJet FTX Green resin (microsla); (b) bipartite silicone mold; (c) paraffin sacrifice mold, glycerin-based soap and beeswax, respectively (full scale).

4.2.3 Lost wax process and PDMS biomodels

4.2.3.1 Paraffin casting

In the process of lost wax casting, the paraffin is heated to 65º C and injected in its liquid state into the bipartite silicone mold with a 3 mL syringe. After curing, the paraffin pattern is carefully removed from the bipartite mold (Figure 4.3 a) and placed in an acrylic box, which is fixed to the wall using plasticine at its ends.

Polydimethylsiloxane (PDMS) elastomer (Sylgard 184, Dow Corning) was the last material needed to manufacture the millimeter scale flow biomodels. This material has low refractive index and it is optically transparent [26]. Prior to pouring PDMS into the acrylic box, where the mold is already positioned, the elastomer required an additional process. The elastomer was mixed with its curing agent in a ratio of 10:1 in a container. The resulting mixture was placed under vacuum conditions for 40 minutes to degas it and to eliminate the nucleated air bubbles present in the silicon. The result standed 48 h for its curation at room temperature (approximately 22º C) (Figure 4.3 b). Finally, the PDMS transparent mold was heated 20 minutes in the oven a 75ºC to dissolve the paraffin.

(Figure 4.3 c) shows the final transparent and hollow biomodel.

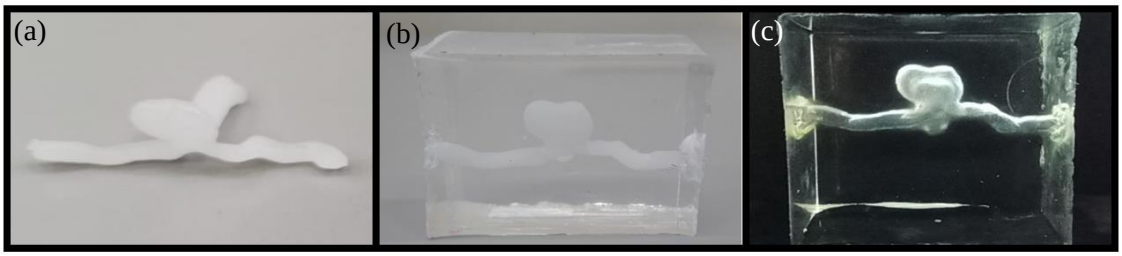

Figure 4.3 - Processing steps to obtain the final biomodel with paraffin. (a) Paraffin; (b) Biomodel after the cure of PDMS; (c) Final PDMS biomodel.

4.2.3.2 Beeswax

For the manufacture of the PDMS biomodels using beeswax as a lost core pattern, the following steps were carried out. Beeswax was melted at 68º C and injected at that temperature into the bipartite mold. After approximately 15 minutes, the pattern solidified and was removed from the split mold (Figure 4.4 a). Then, the same procedure as in the paraffin mold was followed to create the PDMS mold (Figure 4.4 b). The beeswax was removed mechanically (Figure 4.4 c)

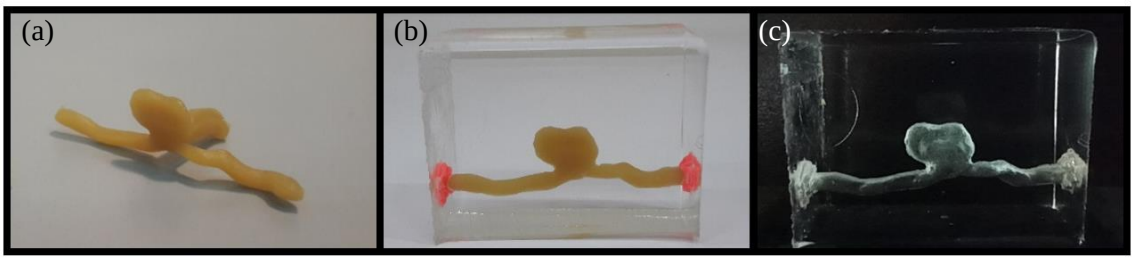

Figure 4.4 - Processing steps to obtain the final biomodel with beeswax. (a) Beewax; (b) Biomodel after the cure of PDMS; (c) Final PDMS biomodel.

4.2.3.3 Glycerin-based soap casting

The third lost core pattern is shown in (Figure 4.5 a). Glycerin-based soap was melted in an electric stove at 60ºC and injected into the bipartite mold where it remained for 30 minutes for solidification. The manufacturing and curing PDMS process was similar to the previous ones (Figure 4.5 b). After curing, the glycerine-based soap was dissolved in water at room temperature on a magnetic stirrer. Finally, the channels were cleaned with a water jet (Figure 4.5 c).

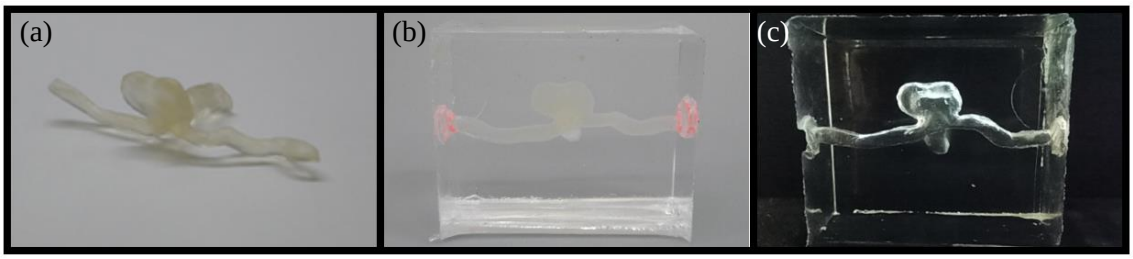

Figure 4.5 - Processing steps to obtain the final biomodel with glycerine-based soap. (a)glycerine-based soap; (b) Biomodel after the cure of PDMS; (c) Final PDMS biomodel.

4.2.4 Flow visualizations setup and numerical simulations

To perform flow visualizations, it was used a high-speed video apparatus consisting of an ultra-high-speed CMOS camera (Photron, FASTCAM SA5) equipped with a set of optical lenses of a 1× magnification zoom-objective (OPTEM Basic Module) and a system of lenses (Optem Zoom 70 XL) with variable magnification from 0.75× to 5.25×. The biomodel was illuminated from the back side by cool white light (Storz, Xenon Nova 300) and a frosted diffuser was positioned between the light and the biomodel to guarantee a field uniform illumination. The experimental setup was mounted on an anti-vibration table (Figure 4 6). Following the work of Pinho et al. [34] and Campo-Deaño [35] a particulate based fluid was developed and applied to perform the flow experiments. This working fluid is composed by glycerol and water at 61% and 39%, respectively (w/w) and with 0.1% of 60 μm (in diameter) suspended polymethylmethacrylate (PMMA) particles. This fluid will be characterized through density, refractive index and viscosity measurements. All experiments were performed at room temperature (T = 20 ± 2ºC).

The recorded images were processed using the ImageJ software and the particles trajectories were obtained using the Z Project plugin.

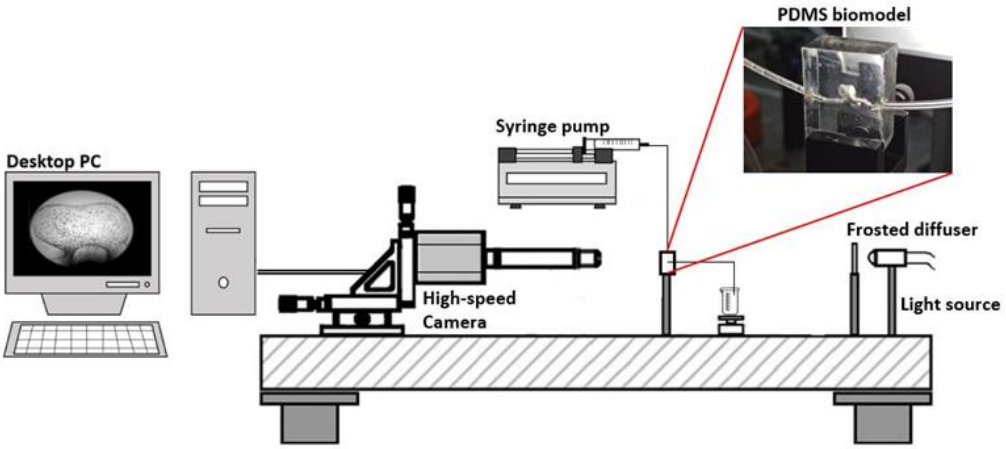

Figure 4.6 - Experimental setup to perform the flow experiments with the developed PDMS biomodels.

On the other hand, the fluid trajectories were obtained numerically. Both continuity and Navier-Stokes equations were solved using the commercial software Fluent, Ansys 2017. Stationary and uncompressible regime and rigid walls were prescribed. The working fluid was considered as a Newtonian fluid (Table 4.4).

Concerning the boundary conditions, the flow rate was imposed in the inlet section (MCA) and outflow in the outlet (ACA) (Figure 4.7). Four different flow rates were imposed to compare the experimental and numerical flows. The flow rates employed were: 5 mL/min, 10 mL/min, 15 mL/min and 20 mL/min. Low flow rates were considered as the recirculation appears and this allowed us to check properly the particles trajectories.

Once both the fluid and boundary conditions are studied, the following steps are followed: 1) The geometry is imported into Ansys Workbench, 2) an 83633 cells mesh is generated and 3) a pressure-based solver is used to solve the numerical integration.

It is important to note that: a) the velocity-pressure coupling was performed using the SIMPLE scheme, b) the spatial discretization of the pressure equation was conducted with the second order approximation, while the momentum equations were discretized with the second order upwind scheme, c) a number of iterations were imposed, but the simulation solutions converged earlier. Moreover, the residuals were set small enough and the stability of the streamlines was monitored with the number of iterations.

Finally, we analysed the results in a model whose cell number was twice the original one while keeping the same spatial distribution. A 3.5% deviation was observed when running this mesh test.

4.3 Results

Before conducting any experiment, the manufactured biomodels were subjected to several tests in order to check their accuracy both dimensionally and optically.

4.3.1 Comparison of geometric structure

Figure 4.7 - Flow inlet and outlet representation

The biomodels geometries must match the original STL model. Five different locations in this model were chosen to be compared with the biomodels (Figure 4.8 a). The air contained within the inner channels provides optimum contrast to measure the biomodels dimensions from images acquired with an inverted microscope (Figure 4.8 b)

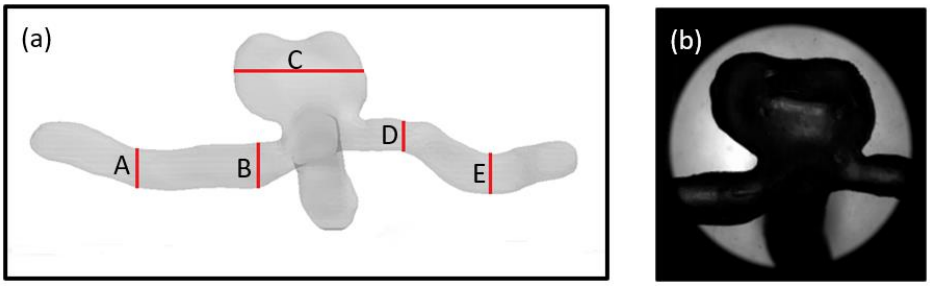

Figure 4.8 - Schematic representation of the locations analysed: (a) in the STL model; (b) microscope image obtained to measure the location C.

Image J software allowed us to perform measurements at the different locations. The average value was then compared with the dimensions of the original STL model.

Tables 4.2 and 4.3 show the values of the dimensions and average errors calculated for the real and reduced biomodels, respectively.

Table 4.2 Dimensions and the average error of real PDMS biomodel (mm) obtained with the three different lost core materials

	STL	BEESWAX	GLYCERIN	PARAFFIN
A	2.587	2.390	2.425	2.364
B	2.897	2.725	2.784	2.756
C	8.392	8.775	8.877	8.817
D	2.122	1.947	2.005	1.875
E	2.693	2.505	2.522	2.460
Average Error		6.67%	5.56%	7.76%

Table 4.3 Dimensions and average error of the reduced PDMS biomodel (mm) obtained with the three different lost core materials.

	STL	BEESWAX	GLYCERIN	PARAFFIN
A	1.811	1.691	1.731	1.624
B	2.028	1.883	1.878	1.879
C	5.875	5.605	5.628	5.621
D	1.485	1.373	1.398	1.403
E	1.885	1.772	1.796	1.762
Average Error		6.38%	5.33%	6.80%

Analyzing the obtained values, it can be observed that the differences between the transparent biomodels and the respective STL format are approximately 0.21 mm for the regions A, B, D and E and 0.42 mm for the region C, in the paraffin biomodel. For the beeswax biomodel the differences were approximately 0.18 mm for A, B, D and E regions and 0.39 mm in C, and for the glycerin-based soap biomodel, the difference was 0.14mm for A, B, D and E and 0.48mm for C.

The reduced biomodels presented the differences in the channels of approximately 0.14 mm in A, B, D and E, and 0.25 in C in the case of the paraffin biomodel. For the beeswax biomodel the differences were approximately 0.12 mm for A, B, D and E and 0.27 mm in C, and for the glycerin-based soap biomodel, the difference was 0.10 mm for A, B, D and E and 0.25 mm for C.

Furthermore, it can be observed that for both biomodels, real and the 30% reduced size, those that showed a smaller error in general, were the ones made with glycerin-based soap as a sacrifice material, followed by the biomodels beeswax, and finally those made with paraffin. It can also be observed that the reduced size biomodels presented a lower percentage of errors than the biomodels manufactured in real size, however this difference is very small, which allows saying that the manufacturing process used permits to make reliable copies of the STL model and with good reproducibility.

4.3.2 Comparison of optical channel transparency

The second restriction is the need to perform flow visualizations in the developed PDMS biomodels. Both the refractive index of the PDMS and the fluid used in the experiments must be as close as possible. If the fluid refractive index is much lower than the PDMS, it appears a black distorted region next to the channel walls [35]. This distortion affects the particle visualization and it disappears completely when the refractive index of the fluid is similar to the PDMS.

In this work, the refractive indices of PDMS and working fluids were measured using an Abbemat 500 refractometer. The fluid that matches the PDMS refractive index is composed by glycerol at 61% diluted (w / w) in water. The density of the mixture was measured with an Anton Paar 5000M densimeter and its viscosity a Cannon-Fenske viscometer. All the physical properties were measured at 25ºC. Table 4.4 shows the values obtained.

Table 4.4 Physical properties of the materials used in this study.

Fluids	Refractive index	Viscosity Pa.s	Density g/cm^3
Water	1.333	0.920 x 10^{-3}	0.997
Water/glycerol	1.412	1.290 x 10^{-2}	1.153
PDMS	1.412	____	____

Once the liquid refractive index matches the PDMS one, it is injected into the channels and a graph paper is placed on the back of the biomodel to visualize the optical distortions caused by the solid-liquid interaction in the gridlines. The result of applying this technique, proposed by Hopkins et al. [36], is shown in (Figure 4.9). Two different

tests were conducted. The first one checked if it was possible to see particles in the IA (Figure 4.9 a). It is quite difficult to see the particles when paraffin is employed in the manufacturing process (Fig 4.9 a1). To remove the paraffin in the PDMS biomodel, is necessary to melt it. The melted paraffin interacts with the PDMS and this process alters the biomodel optical properties. Nevertheless, the particles can be seen without problems when the mold is made of beeswax (Figure 4.9 a2) and glycerine based soap (Figure 4.9 a3). As it is not necessary to increase the temperature of the biomodel to withdraw these materials, the biomodel optics is not altered.

This is clearly seen in the second test. The fluid mixture is injected in the channels (Figure 4.9 b) and matches the PDMS biomodel refractive index except in the paraffin nuclei. The increase of temperature of the biomodel causes the refractive index alteration and the walls are clearly seen. In contrast, the biomodel disappear when the beeswax and glycerine are employed. If water is employed as fluid (Figure 4.9 c), the fluid refractive index is lower than the PDMS one and the walls can be seen. Moreover, the straight gridlines (Figures 4.9 b1 and 4.9 b2) are distorted and a curvature appears (Figs. 4.9 c1 and 4.9 c2).

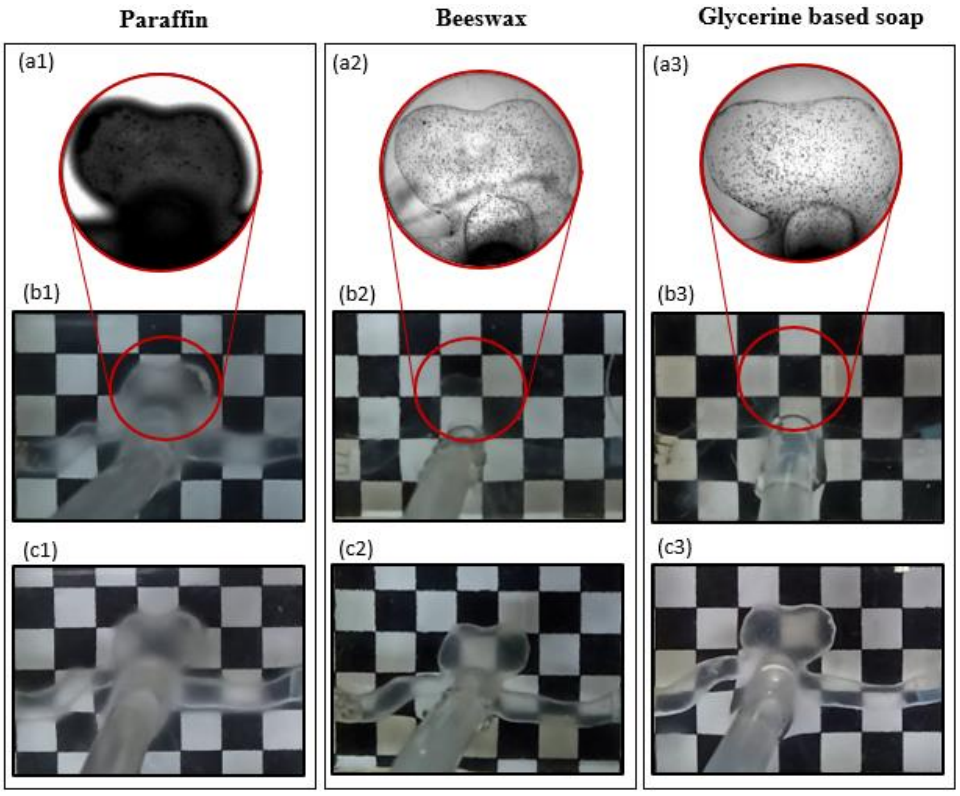

Figure 4.9 - Distortion of the grid lines (a) detail of the particle visualization test; (b) distortion when the channel is filled with water/glycerol solution and PMMA particles; (c) when it is filled with only water.

4.4 Experimental and Numerical Comparison of the Biomodels

The previous section has shown that the biomodels manufactured using beeswax and glycerin-based soap are the ones suitable to perform optical hemodynamic studies. Experiments and CFD analysis were also performed. The numerical simulation is a widely used tool to perform hemodynamic studies [37]. This tool has allowed us to perform qualitative comparisons of the streamlines obtained numerically with the experimental results [38,39].

4.4.1 Experimental procedure

As mentioned in section 2.4, the reduced version of the PDMS biomodel was fixed, and a syringe pump with a 50 mL syringe was used to pump the working fluid at a constant flow rate within the channels of the biomodel. The PMMA trajectories resulting from the image process are shown in Figure 4.10 (a)-(d).

4.4.2 Numerical simulation and qualitative comparison with the experimental

Once the particles trajectories were obtained, the STL format model dimensions were scaled down a 30% in SolidWorks and exported to Parasolid format. This format was imported in the CFD analysis software and the numerical trajectories were obtained as it is described in section 2.4.

In order to compare the results obtained in the experimental analysis with the numerical analysis, it was established as a criterion to observe the behaviour of the streamlines in both cases. The results obtained in both cases can be seen in Figure 4.10 and Figure 4.11.

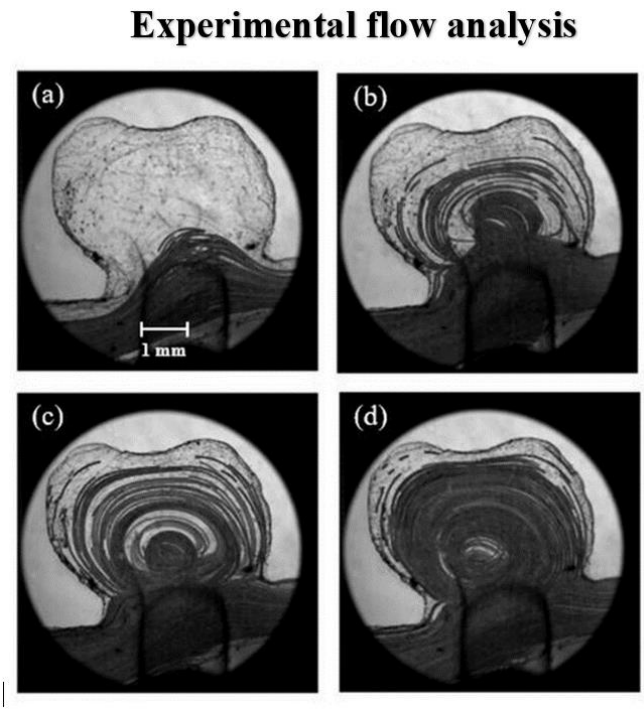

Figure 4.10 Experimental flow analysis with flow rate of: (a) Q = 5 mL/min; (b) Q = 10 mL/min; (c) Q = 15 mL/min; (d) Q = 20 mL/min.

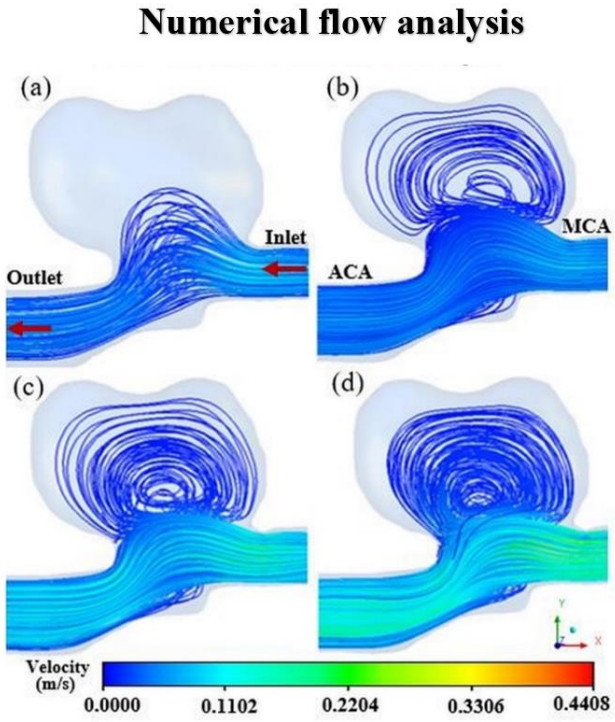

Figure 4.11 - Numerical flow analysis with flow rate of: (a) Q = 5 mL/min; (b) Q = 10 mL/min; (c) Q = 15 mL/min; (d) Q = 20 mL/min.

Figure 4.10 and 4.11, shows both the experimental and numerical trajectories. If a qualitative comparison is performed, the behavior of the fluid flow is nearly identical. A good agreement is shown in the regions close to the channel inlet and outlet where

laminar flows were observed. Furthermore, the agreement remains when the flow behavior changed. If the trace particles get closer to the neck of the aneurysm, the flow bends towards the aneurysm and vortices are observed for the tested flow rates (except the lowest one (5mL/min)). This recirculation increases its intensity for the higher velocities. All these structures are pretty similar in both the experiments and numerical simulations.

4.5 Conclusions

To improve our understanding about the blood flow behavior in blood vessels, *in vitro* flow studies have a crucial role. Hence, the main objective of this study was to propose a fabrication method from real flow biomodels, at the millimeter scale and suitable for hemodynamic studies. Generally, these kinds of biomodels use a lost core casting method for their creation and one of the difficulties is to find the appropriate sacrificial material for each application.

The fabrication of the biomodels was made by using three lost core materials, paraffin, beeswax and glycerin-based soap that can be removed without high temperatures and can be modeled in silicone molds. The materials used were beeswax and glycerine-based soap, which are removed manually and in water at room temperature, respectively, reproducing biomodels with optimum optical characteristics and no residues, however, the biomodels produced using the paraffin have low optical transparency at room temperature. Overall, all the lost core material shows an adequate geometrical replication from the DICOM images and the average relative error of the main dimensions are less than 8%, being the reduced model with smaller error, less than 7%.

The developed PDMS biomodels were able to mimic the real artery geometry and could be easily replicated with high enough transparency to perform flow visualization studies. The flow measurements performed with the biomodel were in good agreement with CFD numerical simulations. Hence, this work shows that the proposed biomodels have the potential to be used as *in vitro* models to study complex hemodynamics phenomena happening in different kinds of pathologies such as aneurysms and stenotic blood vessels.

References

[1] C. Rodriguez-Régent et al., “Non-invasive diagnosis of intracranial aneurysms,” Diagn. Interv. Imaging, vol. 95, no. 12, pp. 1163–1174, 2014, doi: 10.1016/j.diii.2014.10.005.

[2] S. Sathyan et al., “Association of Versican (VCAN) gene polymorphisms rs251124 and rs2287926 (G428D), with intracranial aneurysm,” Meta Gene, vol. 2, pp. 651–660, 2014, doi: 10.1016/j.mgene.2014.07.001.

[3] D. Pinho, D. Bento, J. Ribeiro, and R. Lima, “An in vitro experimental evaluation of the displacement field in an intracranial aneurysm model,” Mech. Mach. Sci., vol. 24, no. June, pp. 261–268, 2015, doi: 10.1007/978-3-319-09411-3.

[4] F. Caranci, F. Briganti, L. Cirillo, M. Leonardi, and M. Muto, “Epidemiology and genetics of intracranial aneurysms,” Eur. J. Radiol., vol. 82, no. 10, pp. 1598–1605, 2013, doi: 10.1016/j.ejrad.2012.12.026.

[5] G. Tromp, S. Weinsheimer, A. Ronkainen, and H. Kuivaniemi, “Molecular basis and genetic predisposition to intracranial aneurysm,” Ann. Med., vol. 46, no. 8, pp. 597–606, 2014, doi: 10.3109/07853890.2014.949299.

[6] C. Cardoso, C. S. Fernandes, R. Lima, and J. Ribeiro, “Biomechanical analysis of PDMS channels using different hyperelastic numerical constitutive models,” Mech. Res. Commun., vol. 90, pp. 26–33, 2018, doi: 10.1016/j.mechrescom.2018.04.007.

[7] K. Valen-Sendstad, K. A. Mardal, M. Mortensen, B. A. P. Reif, and H. P. Langtangen, “Direct numerical simulation of transitional flow in a patient-specific intracranial aneurysm,” J. Biomech., vol. 44, no. 16, pp. 2826–2832, 2011, doi: 10.1016/j.jbiomech.2011.08.015.

[8] H. Baek, M. V. Jayaraman, P. D. Richardson, and G. E. Karniadakis, “Flow instability and wall shear stress variation in intracranial aneurysms,” J. R. Soc. Interface, vol. 7, no. 47, pp. 967–988, 2010, doi: 10.1098/rsif.2009.0476.

[9] E. Doutel, J. Carneiro, J. B. L. M. Campos, and J. M. Miranda, “Experimental and numerical methodology to analyze flows in a coronary bifurcation,” Eur. J. Mech. B/Fluids, vol. 67, pp. 341–356, 2018, doi: 10.1016/j.euromechflu.2017.09.009.

[10] B. B. Lieber, A. P. Stancampiano, and A. K. Wakhloo, “Alteration of hemodynamics in aneurysm models by stenting: Influence of stent porosity,” Ann. Biomed. Eng., vol. 25, no. 3, pp. 460–469, 1997, doi: 10.1007/BF02684187.

[11] W. M. P. F. Bosman et al., “Aortic customize: An in vivo feasibility study of a percutaneous technique for the repair of aortic aneurysms using injectable elastomer,” Eur. J. Vasc. Endovasc. Surg., vol. 40, no. 1, pp. 65–70, 2010, doi: 10.1016/j.ejvs.2010.02.019.

[12] P. S. D’Urso et al., “Cerebrovascular biomodelling: a technical note,” Surg Neurol, vol. 52, pp. 490–500, 1999, doi: 10.1080/713842980.

[13] G. Wurm, B. Tomancok, P. Pogady, K. Holl, and J. Trenkler, “Cerebrovascular stereolithographic biomodeling for aneurysm surgery: Technical note,” J. Neurosurg., vol. 100, no. 1, pp. 139–145, 2004, doi: 10.3171/jns.2004.100.1.0139.

[14] G. Wurm, M. Lehner, B. Tomancok, R. Kleiser, and K. Nussbaumer, “Cerebrovascular biomodeling for aneurysm surgery: Simulation-based training by means of rapid prototyping technologies,” Surg. Innov., vol. 18, no. 3, pp. 294–306, 2011, doi: 10.1177/1553350610395031.

[15] A. Scerrati et al., “A workflow to generate physical 3D models of cerebral aneurysms applying open source freeware for CAD modeling and 3D printing,” Interdiscip. Neurosurg. Adv. Tech. Case Manag., vol. 17, no. December 2018, pp. 1–6, 2019, doi: 10.1016/j.inat.2019.02.009.

[16] A. Leal, M. Souza, and P. Nohama, “Additive Manufacturing of 3D Biomodels as Adjuvant in Intracranial Aneurysm Clipping,” Artif. Organs, vol. 43, no. 1, pp. E9–E15, 2019, doi: 10.1111/aor.13303.

[17] T. Acar, A. B. Karakas, M. A. Ozer, A. M. Koc, and F. Govsa, “Building Three-Dimensional Intracranial Aneurysm Models from 3D-TOF MRA: a Validation Study,” J. Digit. Imaging, vol. 32, no. 6, pp. 963–970, 2019, doi: 10.1007/s10278-019-00256-6.

[18] T. Kimura et al., “Simulation of and training for cerebral aneurysm clipping with 3-dimensional models,” Neurosurgery, vol. 65, no. 4, pp. 719–725, 2009, doi: 10.1227/01.NEU.0000354350.88899.07.

[19] T. Mashiko et al., “Development of three-dimensional hollow elastic model for cerebral aneurysm clipping simulation enabling rapid and low cost prototyping,” World Neurosurg., vol. 83, no. 3, pp. 351–361, 2015, doi: 10.1016/j.wneu.2013.10.032.

[20] Y. Kang et al., “Three-dimensional printing technology for treatment of intracranial aneurysm,” Chinese Neurosurg. J., vol. 2, no. 1, pp. 1–10, 2016, doi: 10.1186/s41016-016-0046-3.

[21] J. R. Ryan, K. K. Almefty, P. Nakaji, and D. H. Frakes, “Cerebral Aneurysm Clipping Surgery Simulation Using Patient-Specific 3D Printing and Silicone Casting,” World Neurosurg., vol. 88, pp. 175–181, 2016, doi: 10.1016/j.wneu.2015.12.102.

[22] B. O. Erbano et al., “Rapid prototyping of three-dimensional biomodels as an adjuvant in the surgical planning for intracranial aneurysms,” Acta Cir. Bras., vol. 28, no. 11, pp. 756–761, 2013, doi: 10.1590/S0102-86502013001100002.

[23] C. H. A. Tam, Y. C. Chan, Y. Law, and S. W. K. Cheng, “The Role of Three-Dimensional Printing in Contemporary Vascular and Endovascular Surgery: A Systematic Review,” Ann. Vasc. Surg., vol. 53, pp. 243–254, 2018, doi: 10.1016/j.avsg.2018.04.038.

[24] E. Doutel, J. Carneiro, M. S. N. Oliveira, J. B. L. M. Campos, and J. M. Miranda, “Fabrication of 3d mili-scale channels for hemodynamic studies,” J. Mech. Med. Biol., vol. 15, no. 1, pp. 1–21, 2015, doi: 10.1142/S0219519415500049.

[25] S. G. Yazdi, P. H. Geoghegan, P. D. Docherty, M. Jermy, and A. Khanafer, “A Review of Arterial Phantom Fabrication Methods for Flow Measurement Using PIV Techniques,” Ann. Biomed. Eng., vol. 46, no. 11, pp. 1697–1721, 2018, doi: 10.1007/s10439-018-2085-8.

[26] P. H. Geoghegan, N. A. Buchmann, C. J. T. Spence, S. Moore, and M. Jermy, “Fabrication of rigid and flexible refractive-index-matched flow phantoms for flow visualisation and optical flow measurements,” Exp. Fluids, vol. 52, no. 5, pp. 1331–1347, 2012, doi: 10.1007/s00348-011-1258-0.

[27] A. V. Souza, J. E. Ribeiro, and R. Lima, “Manufacturing Process of a Brain Aneurysm Biomodel in PDMS Using Rapid Prototyping,” Lect. Notes Comput.

Vis. Biomech., vol. 34, pp. 671–676, 2019, doi: 10.1007/978-3-030-32040-9_69.

[28] J. R. Sherman et al., “Investigation of new flow modifying endovascular image-guided interventional (EIGI) techniques in patient-specific aneurysm phantoms (PSAPs) using optical imaging,” Med. Imaging 2008 Vis. Image-guided Proced. Model., vol. 6918, no. 69181, p. 69181V, 2008, doi: 10.1117/12.772583.

[29] R. F. Smith, B. K. Rutt, and D. W. Holdsworth, “Anthropomorphic carotid bifurcation phantom for MRI applications,” J. Magn. Reson. Imaging, vol. 10, no. 4, pp. 533–544, 1999, doi: 10.1002/(SICI)1522-2586(199910)10:4<533::AID-JMRI6>3.0.CO;2-Z.

[30] L. Allard, G. Soulez, B. Chayer, F. Treyve, Z. Qin, and G. Cloutier, “Multimodality vascular imaging phantoms: A new material for the fabrication of realistic 3D vessel geometries,” Med. Phys., vol. 36, no. 8, pp. 3758–3763, 2009, doi: 10.1118/1.3171692.

[31] M. Stoiber, T. Schlöglhofer, P. Aigner, C. Grasl, and H. Schima, “An alternative method to create highly transparent hollow models for flow visualization,” Int. J. Artif. Organs, vol. 36, no. 2, pp. 131–134, 2013, doi: 10.5301/ijao.5000171.

[32] L. V. Boas et al., “Assessment of the deformability and velocity of healthy and artificially impaired red blood cells in narrow polydimethylsiloxane (PDMS) microchannels,” Micromachines, vol. 9, no. 8, pp. 1–16, 2018, doi: 10.3390/mi9080384.

[33] K. R. Partola, B. Andemariam, and G. Lykotrafitis, “Microfluidic experimental setup for adhesion and recovery measurements of red blood cells in sickle cell disease,” J. Mech. Behav. Biomed. Mater., vol. 71, no. December 2016, pp. 80–84, 2017, doi: 10.1016/j.jmbbm.2017.02.031.

[34] D. Pinho, L. Campo-Deaño, R. Lima, and F. T. Pinho, “In vitro particulate analogue fluids for experimental studies of rheological and hemorheological behavior of glucose-rich RBC suspensions,” Biomicrofluidics, vol. 11, no. 5, 2017, doi: 10.1063/1.4998190.

[35] L. Campo-Deaño, R. P. A. Dullens, D. G. A. L. Aarts, F. T. Pinho, and M. S. N. Oliveira, “Viscoelasticity of blood and viscoelastic blood analogues for use in polydymethylsiloxane in vitro models of the circulatory system,”

Biomicrofluidics, vol. 7, no. 3, 2013, doi: 10.1063/1.4804649.

[36] L. M. Hopkins, J. T. Kelly, A. S. Wexler, and A. K. Prasad, “Particle image velocimetry measurements in complex geometries,” Exp. Fluids, vol. 29, no. 1, pp. 91–95, 2000, doi: 10.1007/s003480050430.

[37] K. M. Saqr et al., “What does computational fluid dynamics tell us about intracranial aneurysms? A meta-analysis and critical review,” J. Cereb. Blood Flow Metab., 2019, doi: 10.1177/0271678X19854640.

[38] A. C. Marin, T. Grossi, E. Bianchi, G. Dubini, and D. Lacroix, “μ-Particle tracking velocimetry and computational fluid dynamics study of cell seeding within a 3D porous scaffold,” J. Mech. Behav. Biomed. Mater., vol. 75, no. August, pp. 463–469, 2017, doi: 10.1016/j.jmbbm.2017.08.003.

[39] R. Agujetas, C. Ferrera, A. C. Marcos, J. P. Alejo, and J. M. Montanero, “Numerical and experimental analysis of the transitional flow across a real stenosis,” Biomech. Model. Mechanobiol., vol. 16, no. 4, pp. 1447–1458, 2017, doi: 10.1007/s10237-017-0898-2.

Chapter 5

Analysis of fluid flow inside an intracranial aneurysm: an *in vitro* and *in silico* approach[1]

5.1 Introduction

Cardiovascular diseases are the leading cause of death in the world. Ischemic heart diseases and cerebrovascular diseases are the origin of 85.6% of the total cardiovascular deaths. Global statistics show that cerebrovascular diseases are the second cause worldwide and the leading one in Southeast and East Asia [1].

One of the responsible for the cerebrovascular deaths is the intracranial aneurysms (IA). IAs are local dilations of intracranial arteries [2]. Early reports [3,4], based in angiographic studies and autopsies, ranged the IAs occurrence from 0.5% to 6%. The improvement of the imaging techniques has limited this range to 3.2% of the population [5]. A 0.25% of these IAs will rupture and present subarachnoid hemorrhage [6]. The mortality rate of these hemorrhages reaches up to 60% and the dependence rate, among the survivors, is below 40% [7]. Multiple devices have been developed to exclude IAs [8] or to divert the flow [9,10]. All these treatments not only involve serious risks but also important expenses for the health system [11] that are going to increase as the population is aging.

Therefore, it is quite important the mechanisms that trigger IAs creation. Scientists claim that a combination of multiple factors may lead to an IA appearance and development: genetic disorders, mycotic infection, hypertension, cigarette smoke inhalation, alcohol ingestion and just aging [12,13]. These factors result in an alteration of the original arterial wall properties and the flow behavior. The endothelial cells sense those changes and start different biological processes [14-18] which lead to a dynamic cycle of wall degeneration and posterior remodeling plus additional changes in the flow.

[1] Souza, A. et al., 2020. Analysis of fluid flow inside an intracranial aneurysm: an *in vitro* and *in silico* approach. Article in preparation for submission to the International Journal of Mechanical Sciences.

Depending on the wall status, the location of the lesion, the hemodynamic loads, the adjacent structures and possible inflammation processes, a new geometry will progress. This new geometry wall (aneurysm) will evolve and could be stabilized or ruptured [19].

These complex processes need to be understood [20] and different sources must be employed to understand the underlying IA mechanisms [19] but it seems that the most prominent role is on hemodynamics.

Several techniques can perform non-invasive *in vivo* flow measurements: phase-contrast magnetic resonance imaging (PC-MRI), magnetic resonance angiography (MRA), 4D computed tomography angiography (4D-CTA) and transcranial Doppler (TCD) ultrasounds. TCD could be a reasonable solution but its measurements are indirect and it does not apply to every artery and patient [21-23]. 4D-CTA is evolving and has a good potential [24,25] and MR techniques are the most widely used. Recently, the laminar Wall Shear Stress (WSS) was measured in the vessel wall using quantitative MRA [26]. This study showed that if the laminar WSS is measured in the parent vessel, its values are higher in growing IAs than in the stable ones. Using MR techniques, a reasonably consistent relative distribution of WSS can be achieved if the measured values are compared with numerical ones [27]. Nevertheless, MR techniques underestimate WSS values [27,28] and lack of enough resolution for small vessels [28].

While *in vivo* techniques are evolving, substantial progress has been done employing *in silico* and *in vitro* techniques. Computational Fluid Dynamics (CFD) applied to IAs can provide physicians valuable knowledge from non-invasive measurements. Early works calculated the WSS in the locations with the highest probability of aneurysm formation (e. g. bifurcations or highly curved arteries) [29]. These innovative studies involving 2D steady simulations in simple geometries coming from radiographs quickly evolved. Different aspects were gradually introduced: 2D idealized IAs geometries [30], 3D real geometries [31], pulsatile flow [32], patient specific inflow conditions [33], elastic walls [34].

This development has allowed the simulation of the presence of multiple aneurysms [35], the effect of surface blebs [36], the analysis of thrombus appearance [37], the inclusion of coils [38,39] and stents or flow diverters considering them as porous media [40,41]. Such is the emphasis to improve the simulations that different challenges have been organized. In those challenges, different research groups test their

methodologies in identical geometries to predict the aneurysm rupture degree [42,43]. Nevertheless, a reasonable percentage of predictions are not correct and the most recent studies have shown, that, in addition to morphological and hemodynamic aspects, it is necessary an improved knowledge in the biological aspects of the wall, to integrate advanced rupture models and clinical metadata [43]. In fact, it is mandatory an experimental validation when performing a simulation [44].

The development in manufacturing techniques has been simultaneous to the CFD. This development has allowed the improvement of *in vitro* vascular models. The first models were glass made aneurysms [45]. Then silicone models appeared [46] and recently, we have developed low cost PDMS models [47]. Different techniques have been applied to those models: Magnetic Resonance (MR), Laser Doppler, Anemometry (LDA) and Particle Image Velocimetry (PIV). PIV is the most used experimental technique to validate numerical simulations.

Nevertheless, most *in vitro* studies can only obtain the velocity field in 2D and 3D vortex structures cannot be captured. Recent studies have demonstrated the importance of analysing the 3D vortex structures [48,49]. In the present work we study a patient specific intracranial aneurysm located in the Internal Carotid Artery. We performed a numerical simulation which was validated experimentally. For this reason, we manufactured a patient specific aneurysm biomodel and injected a fluid whose physical characteristics are quite close to the blood ones. Then we add different size particles and studied, employing dimensional analysis, which ones would be the best option to track the fluid trajectories without any interference. Finally, we employed digital image processing to resolve the trajectories and to compare them with the numerical ones. The proposed method can capture the 3D flow behaviour at different instants of the entire cardiac cycle and its results are in agreement with the simulations. This method will allow us to get different hemodynamical factors related with the aneurysm cycle appearance-growth-rupture.

The paper is organized as follows. The patient geometry, the details of the numerical and experimental methods are described in Section 5.2. Section 5.3 shows and discusses both numerical and experimental results. The paper closes in Section 5.4 with the conclusions.

5.2 Materials and Methods

The present study comprises an analysis performed in an aneurysm. We numerically simulated the aneurysm and validated the simulation by applying the Particle Track Velocimetry technique to an aneurysm biomodel. In this section, we will describe both the experimental and the numerical methods. First, we present the patient specific geometry acquisition process. Then we show the details of the numerical simulation. Finally, we explain the fluid particle selection process and the details of the experiments conducted to validate those simulations.

5.2.1 Patient Geometry

We selected a patient whose aneurysm was diagnosed in the Hospital Universitario de Badajoz (HUB). Computed Tomography Angiography (CTA) were performed with a single 64-detector CT scanner (LightSpeed VCT; GE Healthcare, Milwaukee, Wisconsin). Scanning parameters were: 64 × 0.625 collimation, 0.9 pitch, 0.5-second rotational time, 120 kVp and 335 mA). The source images were reformatted as maximum intensity projection (MIP) and volume-rendered images.

The aneurysm is located in the bifurcation of the Internal Carotid Artery (ICA) into the Anterior Cerebral Artery (ACA) and the Middle Cerebral Artery (MCA) (Fig. 5.1).

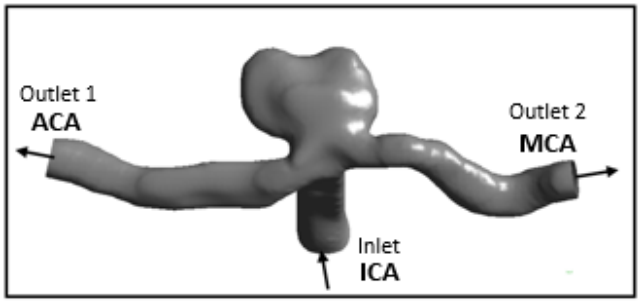

Figure 5.1 - ICA aneurysm.

The DICOM (Digital Imaging and Communications in Medicine) images were imported into the 3D Slicer software (Fedorov et al. 2012). Then, a segmentation procedure was conducted: (i) A lower threshold (170 Hounsfield Units) was applied to the first slide of the complete set to select the region of interest, (ii) the selected region underwent a growing process by applying the same threshold to the rest of the slides of the set, and (iii) a 3D model was obtained. Finally, the 3D geometry was optimized

(wrapped and smoothed) and exported in STL format for both numerical simulation and manufacturing processes.

5.2.2 Numerical method

In the present work, the commercial software Fluent [50] was employed to resolve the RANS equations [51]. Those equations were integrated in the steady and incompressible regime following the finite volume method [51]. Rigid walls were assumed and the non-slip condition was activated. The fluid considered was the same employed in the experiments and its properties will be described in the section 5.2.3.

The specific hemodynamics parameters of the patient were not available, hence we selected as ICA boundary conditions a velocity profile reported in the scientific literature [23]. In that study, the velocity profile was measured by Transcranial Doppler (TCD) ultrasonography in a similar aneurysm, located at our anatomical location.

We chose three points representing the whole cardiac cycle (diastole (minimum flow), systole (maximum flow) and an intermediate point) (Table 1). Those points correspond to different Reynolds numbers: 395, 857 and 639, respectively. The characteristic length, D, for the Reynolds number, $Re = \rho vD/\mu$, was the ICA entrance hydraulic diameter (3.78 mm) [52], being v the velocity at that entrance and □ and μ the fluid's density and viscosity, respectively. These three points allowed us to analyse the influence of Re number in the different phases of the cardiac cycle. Nevertheless, two additional points for lower Re, 11 and 50 (Table 1), were added to cover the range where the flow does not present any vortex. We understand that these points do not correspond to a real flow, but vortex absence allowed us to select precisely the particle size for the experiments.

Concerning the fluid behaviour, we are aware of references supporting the use of a non-newtonian fluids because of the impact of a Newtonian behaviour in the simulation results [49]. Nevertheless, accurate simulations claim that this impact is lower than the one caused by the solver election [53] or can have a negligible effect in the velocity field [14]. In this study, the shear rates of the main points analysed were 82.0 s-1 (diástole), 132.3 s-1 (intermediate) and 177.25 s-1 (systole). According to those values, the blood's viscosity were 5 mPas, 4.1 mPas and 3.9 mPas, respectively. The change in the viscosity was practically negligible for more than a half of the cardiac cycle. This supported assuming a Newtonian behaviour.

We performed five different steady simulations for patient 1 and experiments were conducted to validate them. According to the Reynolds numbers for the whole range of values (11-857), the laminar regime was chosen. The boundary conditions at the inlet were uniform velocity profile and outflow for the outlets in each one of those simulations. Preliminary experiments were conducted in patient 1's geometry to get the outflow boundary conditions. We imposed different inlet flow rates and obtained the flow percentage that circulates for each branch (51% for the ACA and 49% for the MCA).

Concerning the geometry meshing, we spatially discretized the aneurysm with an automatic algorithm and obtained tethraedrons whose size was 0.18 mm. The mesh generated consisted of 555147 cells and 161491 nodes (Fig 5.2). The pressure at outlets was the control parameter employed as convergence criterion. The value changed less than a 5% when we doubled the number of cells.

Finally, we integrated the hydrodynamic equations with the pressure-based solver. The gradients in the cell centers were calculated with the Least Squares Cell Based scheme. A second-order and second-order upwind approximations were conducted for the spatial discretization of the pressure and momentum equations, respectively. The SIMPLE procedure was employed to couple the velocity and the pressure.

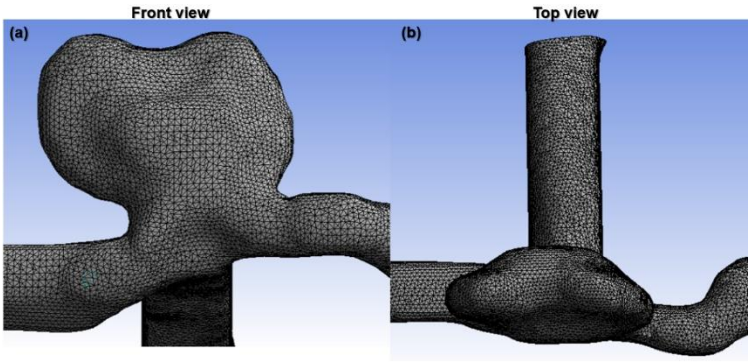

Figure 5.2 -- Details of the grid employed in the numerical simulations (Frontal (Left) and Top (Right)).

Table 1. Inlet flow parameters

	V (m/s)	**Flow rate (mL/s)**	**Reynolds Number**
Extra point 1	0.01	0.10	11
Extra point 2	0.12	1.31	150
Diastole	0.31	3.45	395
Intermediate	0.50	5.58	639
Systole	0.67	7.49	857

5.2.3 Experimental Method

We conducted experiments in the steady regime to validate the numerical method. A polydimethylsiloxane (PDMS) biomodel (Fig. 5.3) was manufactured combining rapid prototyping and lost core casting processes and a glycerine-based soap [47].

Figure 5.3 - Aneurysm biomodel.

The fluid mixture flowing through the biomodel was dimethyl sulfoxide (DMSO) at 52% diluted (w /w) in water. This proportion is necessary to equal the PDMS refractive index (1.412) in order to avoid introducing any visual distortion [54]. Both PDMS and fluid mixture refractive indexes were carefully measured in an Abbemat 500 refractometer. Additionally, the fluid density (1072 kg/m^3) and viscosity (3.15×10^{-3} Pa) were measured at 25 ºC with an Anton Paar 5000M densimeter and a Cannon-Fenske viscosimeter, respectively. These properties are close to the human blood ones measured under high shear rates (1060 kg/m^3 and 4×10^{-3}Pa) [55]. Polymethyl methacrylate (PMMA) particles were added to that fluid up to a 100-ppm concentration to get the fluid trajectories. Their diameter was carefully selected according to the procedure that will be described in this section.

The equipment necessary to perform the experiments is depicted in Fig. 5.4. It consisted of a 2 l pressurized tank (A) connected to the lab pneumatic net. The air pressure inside the tank was regulated by a check valve (B) and a manometer (C) (DIGITRON 2027P). The tank was connected to a vacuum flask (D) filled with the particles-liquid mixture. A magnetic stirrer (E) operated continuously to prevent the particle settle during the experiments. The mixture flow rate leaving the flask was controlled by a hydraulic speed control valve (F) connected to the flask output. Then, the mixture circulated to the aneurysm model (G) (Fig. 5.1) and the flow rate through both the ACA and MCA could

be controlled by two additional hydraulic speed control valves (H) installed far away from the artery outlets and two beakers placed over two weighing scales (I).

A set of digital images of the particles inside the model (1024 x 1024 pixel) were recorded at 7000 frames per second (4000 fps for the two extra flow rates) with an exposure time of 142.6 µs using an ultra-high-speed CMOS camera (Photron, FASTCAM SA5) (J). The camera was equipped with a set of optical lenses (K) which consisted of a 1× magnification zoom-objective (OPTEM Basic Module) and a system of lenses (Optem Zoom 70 XL) with variable magnification from 0.75× to 5.25×. The camera could be displaced both horizontally and vertically using a triaxial translation stage (L) to focus the particles inside the aneurysm. The model (G) was illuminated from the backside by cool white light provided by an optical fiber (M) connected to a light source (Storz, Xenon Nova 300) (N). A frosted diffuser (O) was positioned between the optical fiber and the fluid configuration to provide a uniformly lit background. All this equipment was mounted on an optical table with a pneumatic anti-vibration isolation system (P) to prevent movements in the particles inside the aneurysm

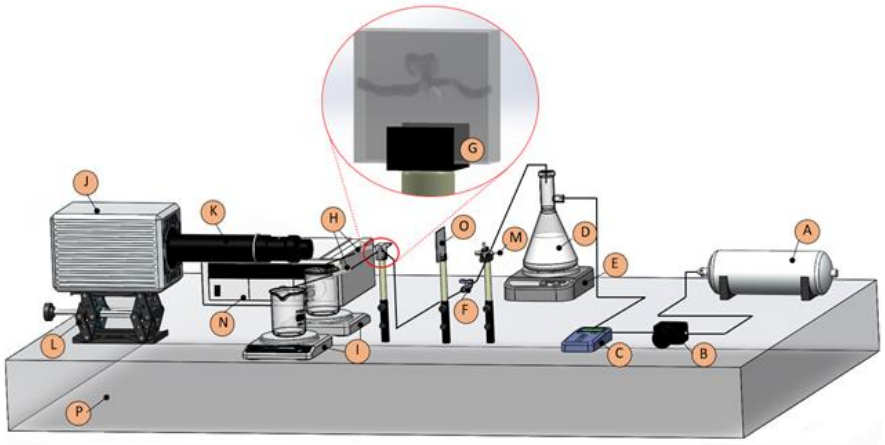

Figure 5.4 - Experimental setup.

The central part of this setup was modified to get aneurysm zenithal images (Fig. 5.5). The frosted diffuser (O) was placed under the model (G). The optical fiber (M) was repositioned to provide nadir light and a mirror (Q) inclined 45 degrees was installed to obtain images of the top of the aneurysm.

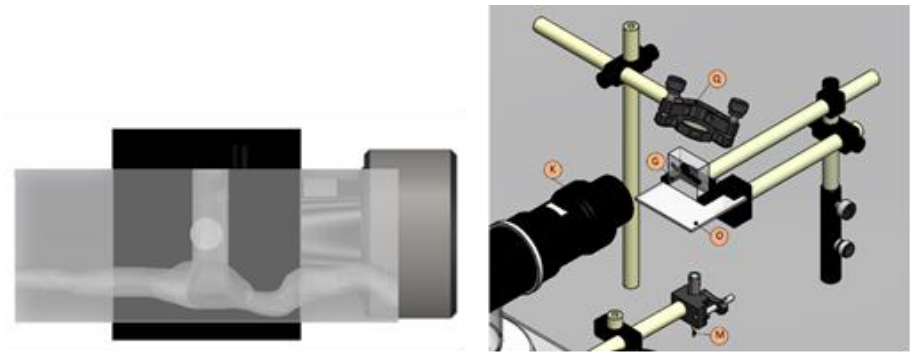

Figure 5.5 - Aneurysm top view. Experimental setup to get high angle shots.

Before starting any experiment, we calibrated the pressurized tank (A) with the check valve (B) and the manometer (C). Each tank pressure corresponds to a different flow rate at ICA. That flow rate is the sum of the flow rates measured at each outlet with two weighting scales (I). Once the pressure required to obtain the flow rates in Table was obtained, we run each experiment as follows: 1) set the tank pressure, 2) open the check valve, 3) wait 15 s to stabilize the flow, 4) record a video of 3000 frames.

A set of frames (400 for the two slowest flow rates and 800 for the rest) for each video was processed with the software ImageJ (Bethesda, MD, EUA) [56]. The minimum intensity Z-projection method was applied to get the particles trajectories and to allow its comparison with the numerical results.

5.2.4 Particle selection process

The previous experimental method could conduct to erroneous trajectories if a wrong particle diameter is selected. It is mandatory to check the tracers fidelity using the dimensionless Stokes number (Stk). Stokes number is obtained as the ratio between the time a tracer needs to response to a stepwise variation in the flow velocity, τ, and the characteristic flow time scale, τ_p. The tracer response time, τ, can be obtained from the Basset-Boussinesq-Oseen equation [57] and the characteristic flow time, τ_p, is the ratio between the flow characteristics length, L_f, and velocity, v_p. Therefore, Stokes number can be obtained by the equation 5.1 which is:

$$Stk = \frac{d_p^2(\rho_p - \rho_f)}{18\mu}\frac{v_f}{L_f} \quad (5.1)$$

Where d_p is the particle diameter, ρ_p and ρ_f are the particle and fluid densities respectively and μ is the fluid viscosity.

The term ρ_f is usually neglected as gas is the surrounding fluid in many experiments ($\rho_p/\rho_f>>1$) and the equation 5.2 [58,59] can be easily obtained:

$$Stk = \frac{d_p^2 \rho_p}{18\mu} \frac{v_f}{L_f} \quad (5.2)$$

According to equation 5.2, if Stk<0.1 the particles accurately trace the fluid with errors below 1% [57].

We calculated Stokes number considering the less favourable conditions, i.e., the highest particle diameter and flow rate and the lowest characteristic length (hydraulic diameter). As we have different size particles ranging from 20 μm and 60 μm, we selected 60 μm. According to equation 5.2, the value at ICA is Stk=0.013 and those particles trace the flow accurately. Additionally, we calculated Stk value in other locations as the ACA, the MCA and the aneurysm entrance. The highest value in those conditions was located in MCA (Stk=0.055) but in our experiment, ρ_p cannot be neglected as ρ_p=1200 kg/m^3 and ρ_f=1072 kg/m^3. If we take into account the equation 5.1, we obtain Stk=0.0045 for the worst conditions, which is two orders of magnitude below 0.1. Nevertheless, experiments were repeated for 20 μm particles to check any deviation when the same conditions are applied. Fig 5.6 shows the comparison for both particles for Re=11 and Re=150. 20 μm particles reproduce the same trajectories as 60 μm particles and only the thickness of the lines is noticed due to the size difference. As 60 μm particles are easier to visualize and to process we employed this size in our experiments.

5.3 Results and discussion

In this section, we confront the trajectories calculated numerically with the ones obtained experimentally. Fig. 5.7 shows both the top, intermediate and the bottom sections of the ICA which facilitate the flow description. For the non-realistic flow rates, we consider only two main sections (the top and the bottom) as there is not a relative movement related to the intermediate part.

Non-realistic flow rates

In the previous section, we selected two extra points (Table 1) to check the particles trajectories in the absence of vortexes. We reduced the diastole flow rate to avoid any vortex in the aneurysm. That non-realistic flow rate allowed us to get the simplest trajectories (Re=11).

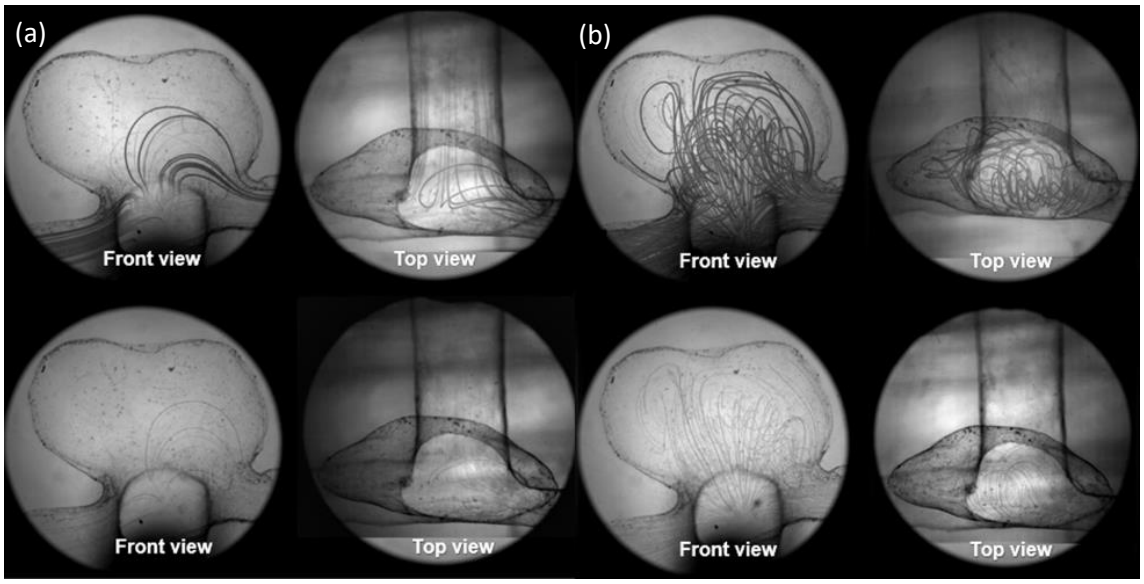

Figure 5.6 - Flow trajectories for different particle size (Top (60 µm), Bottom (20 µm)). (a) Re=11(Left); (b)Re=150 (Right).

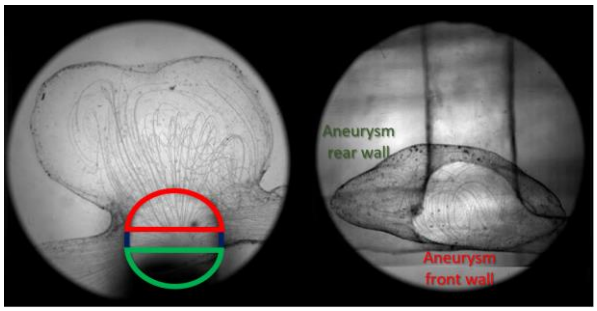

Figure 5.7 - Top (red), intermediate (blue) and bottom (green) ICA sections.

Then, we increased the flow rate to the onset of the vortex appearance (Re=150). Fig. 5.8 shows the flow evolution of both cases where the experimental results reproduce the numerical ones. Fig. 5.8a shows the results for the lowest Reynolds number. In that case, the flow shows a different behaviour depending on the ICA section. The flow circulating through the top enters in the aneurysm and deviates through the MCA. This flow neither touches the wall in front of the ICA nor the top of the aneurysm. Therefore, it does not exert an extra hydrostatic pressure on the wall. On the contrary, the aneurysm is not reached by the flow circulating through the lCA lowest section and it deviates through both the ACA and the MCA. A different behaviour can be found for the higher flow rate (Re=150) (Fig. 5.8b). The flow circulating through the ICA lowest section deviates mainly through the ACA and there is a substantial change in the flow circulating through the ICA upper section. The flow impinges on the wall in front of the ICA (Fig 5.7) before entering into the aneurysm and leaves it through the MCA. Two different recirculation structures appear inside the aneurysm: a vortex ring and a simple

recirculation cell [60]. The flow that enters directly into the aneurysm creates a vortex ring. This part of the flow does not touch any wall. On the other hand, the flow that impinges the wall in front of the ICA, ascends next to that wall, then moves to the rear wall (Fig. 5.7) and finally, directs itself to the MCA.

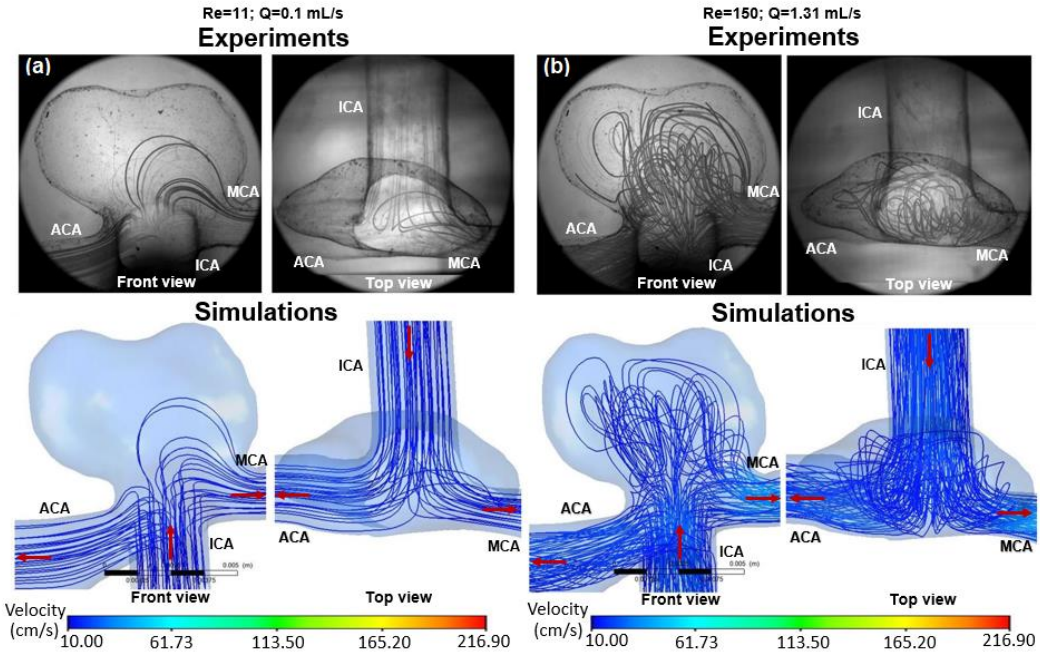

Figure 5.8 - Numerical and experimental results for non-realistic flow rates.

Realistic flow rates

As mentioned in Sec. 5.2.2, we have selected three different ICA flow rates (Table 1) according to the cardiac cycle of a patient with an aneurysm in our location [23]: diastole, intermediate and systole. Fig. 5.9 depicts the diastole results (Re=395). The flow rate is nearly three times the flow rate in extra point 2 (Fig. 5.8b and Table 2). The logical consequence is a significant increase in the flow movement inside the aneurysm. The trajectories cover a larger area inside the aneurysm and the flow reaches the aneurysm top wall. In this case, not only the flow coming from the ICA top (Fig. 5.7) enters the aneurysm but also the one coming from the intermediate part of the ICA. The liquid flowing through the bottom part of the ICA exits through the ACA and MCA as in the previous cases. We also observe the appearance of recirculation cells in the left and right sides of the aneurysm top wall. These cells had not been observed in the previous cases (Re = 11 and Re = 150).

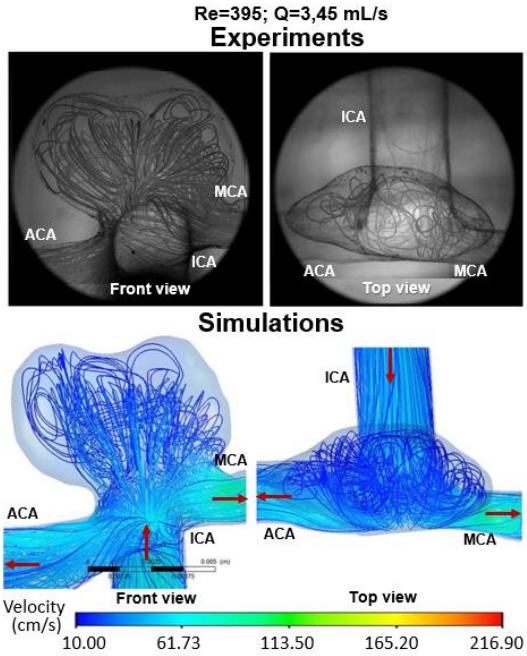

Figure 5.9- Numerical and experimental results for diastolic flow rate.

Regarding the intermediate flow rate case (Re=639, Fig. 5.10), while the size it is increasing due to the flow rate growth, the overall structure does not change with respect to the diastolic one. Fig. 5.10 show how the area inside the aneurysm where the fluid moves has growth and so every cell inside the aneurysm (the central one and the left and right ones at the top). It is obvious that the magnitude of the velocity is higher and also the vorticity. Fig 5.10 front view shows in the central part how the vortex concentration is higher. The vortexes are also closer to the top wall.

Finally, the systole case (Re=857) shows the highest concentration of lines on the left side of the central part of the aneurysmal sac. The vortexes formed in the center of the aneurysm, present with a smaller spacing between them, when compared with the previous cases. That concentration also appears in the vortex close to the wall. In fact, the vortexes are closer to the wall and can have relation with the rupture mechanism [48]. Varble et al. correlated the hemodynamical and morphological properties of ruptured intracranial aneurysms with vortexes occupating large areas inside the aneurysm. Another cause of rupture can be the impact in small wall zones just our case. We have observed how the the liquid flowing through the ICA impinges the front wall and disperses quickly. Our resulting flow can be classified according to Cebral et al. [60] as a complex pattern flow with more than one recirculation zone and the vortexes appearing inside the simulation have experimental correspondence with a quite good agreement between

structures. In fact, figures 5.8-5.11 show almost the same trajectories comparing experiments and numeric.

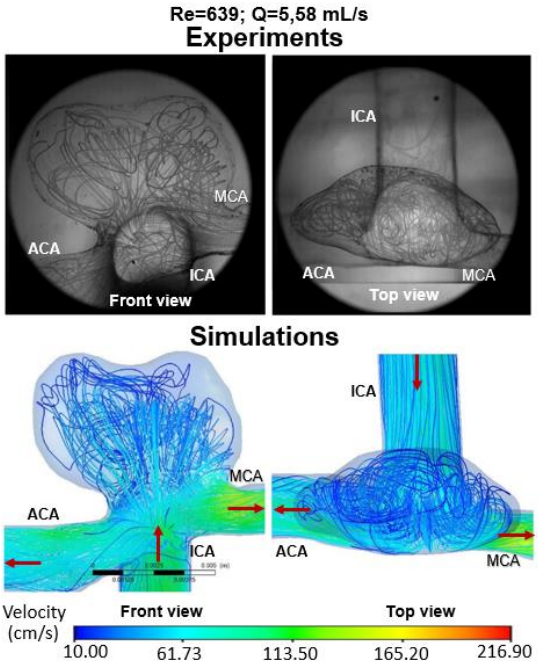

Figure 5.10 - Numerical and experimental results for the intermediate flow rate.

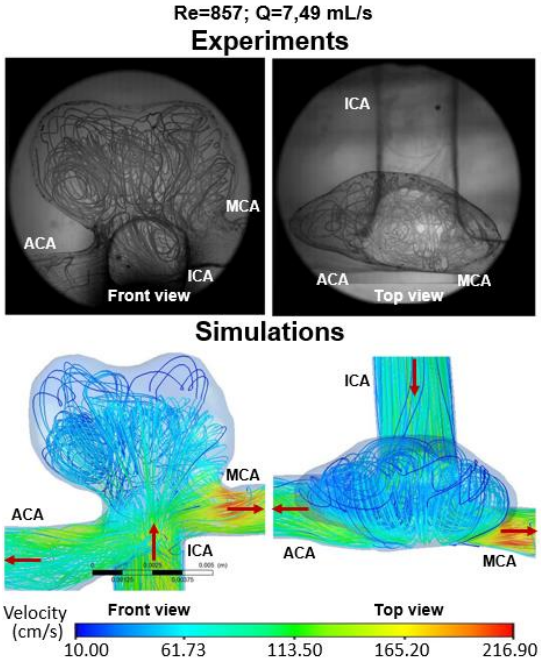

Figure 5.11 - Numerical and experimental results for the systolic flow rate.

5.4 Conclusions

The main objective of the present study was to visualize and characterize the flow inside an intracranial aneurysm in 3D. We performed steady numerical simulations corresponding to five different flow rates circulating through ICA. Simultaneously we conducted the corresponding experiments to validate those calculations. The images obtained were processed to obtain the trajectories which allowed us to validate qualitatively the 3D flow behaviour. The increase of the inlet flow rate has an impact on the vortex size inside the aneurysm. As the flow rate rises, these vorticial structures growth closer to the wall and become more complex. The 3D visualization allowed us also to identify a small area where the flow impinges to the wall. This area and the vortexes can be related to rupture mechanisms [60]. The employed technique broadens the comparison field to the analysis of three-dimensional structures such as the vortexes appearing in complex flows. That will have an immediate impact in the models which take into account the wall remodelling as the areas where the flow impinges, and the vortex exert stronger wall shear stresses are prone to be worn.

References

[1] G. B. D. 2016 C. of D. Collaborators, "Global, regional, and national age-sex specific mortality for 264 causes of death, 1980-2016: a systematic analysis for the Global Burden of Disease Study 2016," *Lancet (London, England)*, vol. 390, no. 10100, pp. 1151–1210, Sep. 2017.

[2] C. Rodriguez-Régent *et al.*, "Non-invasive diagnosis of intracranial aneurysms," *Diagn. Interv. Imaging*, vol. 95, no. 12, pp. 1163–1174, 2014.

[3] S. C. Johnston *et al.*, "Recommendations for the endovascular treatment of intracranial aneurysms: A statement for healthcare professionals from the Committee on Cerebrovascular Imaging of the American Heart Association Council on Cardiovascular Radiology," *Stroke*, vol. 33, no. 10, pp. 2536–2544, 2002.

[4] W. I. Schievink, "Intracranial Aneurysms," *N. Engl. J. Med.*, vol. 336, no. 1, pp. 28–40, Jan. 1997.

[5] M. H. M. Vlak, A. Algra, R. Brandenburg, and G. J. E. Rinkel, "Prevalence of unruptured intracranial aneurysms , with emphasis on sex , age , comorbidity ,

country , and time period : a systematic review and meta-analysis," *Lancet Neurol.*, vol. 10, no. 7, pp. 626–636, 2011.

[6] B. G. Thompson *et al.*, *Guidelines for the Management of Patients With Unruptured Intracranial Aneurysms: A Guideline for Healthcare Professionals From the American Heart Association/American Stroke Association*, vol. 46, no. 8. 2015.

[7] P. S. Amenta *et al.*, "Analysis of Nonmodifiable Risk Factors for Intracranial Aneurysm Rupture in a Large, Retrospective Cohort," *Neurosurgery*, vol. 70, no. 3, pp. 693–701, 2011.

[8] H. Henkes and W. Weber, "The Past, Present and Future of Endovascular Aneurysm Treatment," *Clin. Neuroradiol.*, vol. 25, pp. 317–324, 2015.

[9] H. Nishi *et al.*, "Biodegradable Flow Diverter for the Treatment of Intracranial Aneurysms: A Pilot Study Using a Rabbit Aneurysm Model," *J. Am. Heart Assoc.*, vol. 8, no. 20, pp. 1–13, 2019.

[10] S. Schob *et al.*, "Flow diversion beyond the circle of Willis: Endovascular aneurysm treatment in peripheral cerebral arteries employing a novel low-profile flow diverting stent," *J. Neurointerv. Surg.*, vol. 11, no. 12, pp. 1227–1234, 2019.

[11] A. Malhotra *et al.*, "Management of unruptured intracranial aneurysms in older adults: A cost-effectiveness analysis," *Radiology*, vol. 291, no. 2, pp. 411–417, 2019.

[12] J. C. Lasheras, "The Biomechanics of Arterial Aneurysms," *Annu. Rev. ofFluid Mech.*, vol. 39, pp. 293–321, 2007.

[13] G. Tromp, S. Weinsheimer, A. Ronkainen, and H. Kuivaniemi, "Molecular basis and genetic predisposition to intracranial aneurysm," *Ann. Med.*, vol. 46, no. 8, pp. 597–606, 2014.

[14] S. V. Frolov, S. V. Sindeev, D. Liepsch, and A. Balasso, "Experimental and CFD flow studies in an intracranial aneurysm model with Newtonian and non-Newtonian fluids," *Technol. Heal. Care*, vol. 24, no. 3, pp. 317–333, 2016.

[15] S. Baratchi, K. Khoshmanesh, O. L. Woodman, S. Potocnik, K. Peter, and P. McIntyre, "Molecular Sensors of Blood Flow in Endothelial Cells," *Trends Mol. Med.*, vol. 23, no. 9, pp. 850–868, 2017.

[16] J. M. Dolan, J. Kolega, and H. Meng, "High wall shear stress and spatial gradients in vascular pathology: a review," *Ann. Biomed. Eng.*, vol. 41, no. 7, pp. 1411–1427, Jul. 2013.

[17] P. R. Hoskins, P. V. Lawford, and B. J. Doyle, *Cardiovascular Biomechanics*. 2017.

[18] Y. S. J. Li, J. H. Haga, and S. Chien, "Molecular basis of the effects of shear stress on vascular endothelial cells," *J. Biomech.*, vol. 38, no. 10, pp. 1949–1971, 2005.

[19] J. R. Cebral and M. Raschi, "Suggested connections between risk factors of intracranial aneurysms: A review," *Ann. Biomed. Eng.*, vol. 41, no. 7, pp. 1366–1383, 2013.

[20] G. Zhou, Y. Zhu, Y. Yin, M. Su, and M. Li, "Association of wall shear stress with intracranial aneurysm rupture : systematic review and meta- analysis," *Sci. Rep.*, vol. 7, pp. 1–8, 2017.

[21] D. Tousoulis and C. Stefanadis, "Biomarkers in cardiovascular diseases," in *Biomarkers in Cardiovascular Diseases*, 2013, pp. 1–440.

[22] M. L. Bøthun, Ø. A. Haaland, N. Logallo, F. Svendsen, L. Thomassen, and C. A. Helland, "Cerebrovascular reactivity after treatment of unruptured intracranial aneurysms — A transcranial Doppler sonography and acetazolamide study," *J. Neurol. Sci.*, vol. 363, pp. 97–103, 2016.

[23] M. Jahed, F. Ghalichi, and M. Farhoudi, "Comparison of blood velocity between Transcranial Doppler and numerical method in the patient-specific Circle of Willis with aneurysm," *Biomed. Mater. Eng.*, vol. 30, no. 4, pp. 427–438, 2019.

[24] H. G. J. Kortman, E. J. Smit, M. T. H. Oei, R. Manniesing, M. Prokop, and F. J. A. Meijer, "4D-CTA in neurovascular disease: A review," *Am. J. Neuroradiol.*, vol. 36, no. 6, pp. 1026–1033, 2015.

[25] P. Bouillot *et al.*, "Robust cerebrovascular blood velocity and flow rate estimation from 4D-CTA," *Med. Phys.*, vol. 46, no. 5, pp. 2126–2136, 2019.

[26] D. Brunozzi, P. Theiss, A. Andrews, S. Amin-Hanjani, F. T. Charbel, and A. Alaraj, "Correlation Between Laminar Wall Shear Stress and Growth of Unruptured Cerebral Aneurysms: In Vivo Assessment," *World Neurosurg.*, vol. 131, pp. e599–e605, 2019.

[27] J. Szajer and K. Ho-Shon, "A comparison of 4D flow MRI-derived wall shear stress with computational fluid dynamics methods for intracranial aneurysms and carotid bifurcations — A review," *Magn. Reson. Imaging*, vol. 48, pp. 62–69, 2018.

[28] C. Roloff, D. Stucht, O. Beuing, and P. Berg, "Comparison of intracranial aneurysm flow quantification techniques : standard PIV vs stereoscopic PIV vs

tomographic PIV vs phase- contrast MRI vs CFD," pp. 1–8, 2018.

[29] M. H. Friedman and L. W. Ehrlich, "Numerical simulation of aortic bifurcation flows: The effect of flow divider curvature," *J. Biomech.*, vol. 17, no. 12, 1984.

[30] A. C. Burleson, C. M. Strother, and V. T. Turitto, "Computer Modeling of Intracranial Saccular and Lateral Aneurysms for the Study of Their Hemodynamics," *Neurosurgery*, vol. 37, no. 4, pp. 774–784, Oct. 1995.

[31] L. Antiga, B. Ene-Iordache, and A. Remuzzi, "Computational geometry for patient-specific reconstruction and meshing of blood vessels from MR and CT angiography," *IEEE Trans. Med. Imaging*, vol. 22, no. 5, pp. 674–684, 2003.

[32] D. A. Steinman, J. S. Milner, C. J. Norley, S. P. Lownie, and D. W. Holdsworth, "Image-based computational simulation of flow dynamics in a giant intracranial aneurysm," *Am. J. Neuroradiol.*, vol. 24, no. 4, pp. 559–566, 2003.

[33] T. Hassan *et al.*, "Hemodynamic analysis of an adult vein of Galen aneurysm malformation by use of 3D image-based computational fluid dynamics," *Am. J. Neuroradiol.*, vol. 24, no. 6, pp. 1075–1082, 2003.

[34] T. Hassan *et al.*, "Computational replicas: Anatomic reconstructions of cerebral vessels as volume numerical grids at three-dimensional angiography," *Am. J. Neuroradiol.*, vol. 25, no. 8, pp. 1356–1365, 2004.

[35] S. Saalfeld, S. Voß, O. Beuing, B. Preim, and P. Berg, "Flow-splitting-based computation of outlet boundary conditions for improved cerebrovascular simulation in multiple intracranial aneurysms," *Int. J. Comput. Assist. Radiol. Surg.*, vol. 14, no. 10, pp. 1805–1813, 2019.

[36] J. E. Hippelheuser, A. Lauric, A. D. Cohen, and A. M. Malek, "Realistic non-Newtonian viscosity modelling highlights hemodynamic differences between intracranial aneurysms with and without surface blebs," *J. Biomech.*, vol. 47, no. 15, pp. 3695–3703, 2014.

[37] E. L. Leemans *et al.*, "Impact of Intracranial Aneurysm Morphology and Rupture Status on the Particle Residence Time," *J. Neuroimaging*, vol. 29, no. 4, pp. 487–492, 2019.

[38] T. Otani, S. Ii, M. Hirata, and S. Wada, "Computational study of the non-Newtonian effect of blood on flow stagnation in a coiled cerebral aneurysm," *Nihon Reoroji Gakkaishi*, vol. 45, no. 5, pp. 243–249, 2017.

[39] A. Y. Usmani and S. Patel, "Hemodynamics of a cerebral aneurysm under rest and exercise conditions," *Int. J. Energy a Clean Environ.*, vol. 19, no. 1–2, pp. 119–

136, 2018.

[40] H. Yadollahi-Farsani, E. Scougal, M. Herrmann, W. Wei, D. Frakes, and B. Chong, “Numerical study of hemodynamics in brain aneurysms treated with flow diverter stents using porous medium theory,” *Comput. Methods Biomech. Biomed. Engin.*, vol. 22, no. 11, pp. 961–971, 2019.

[41] Y. Li, D. I. Verrelli, W. Yang, Y. Qian, and W. Chong, “A pilot validation of CFD model results against PIV observations of haemodynamics in intracranial aneurysms treated with flow-diverting stents,” *J. Biomech.*, no. xxxx, p. 109590, 2019.

[42] P. Berg *et al.*, “The Computational Fluid Dynamics Rupture Challenge 2013 - Phase II: Variability of Hemodynamic Simulations in Two Intracranial Aneurysms,” *J. Biomech. Eng.*, vol. 137, no. 12, 2015.

[43] P. Berg *et al.*, “Multiple Aneurysms AnaTomy CHallenge 2018 (MATCH)—phase II: rupture risk assessment,” *Int. J. Comput. Assist. Radiol. Surg.*, vol. 14, no. 10, pp. 1795–1804, 2019.

[44] P. Berg, S. Saalfeld, S. Voß, O. Beuing, and G. Janiga, “A review on the reliability of hemodynamic modeling in intracranial aneurysms: Why computational fluid dynamics alone cannot solve the equation,” *Neurosurg. Focus*, vol. 47, no. 1, pp. 1–9, 2019.

[45] G. G. Ferguson, “Physical factors in the initiation, growth, and rupture of human intracranial saccular aneurysms.,” *J. Neurosurg.*, vol. 37, no. 6, pp. 666–677, 1972.

[46] H. J. Steiger, D. W. Liepsch, A. Poll, and H. J. Reulen, “Hemodynamic stress in terminal saccular aneurysms: A laser-doppler study,” *Heart Vessels*, vol. 4, no. 3, pp. 162–169, 1988.

[47] A. Souza *et al.*, “3D manufacturing of intracranial aneurysm biomodels for flow visualizations: Low cost fabrication processes,” *Mech. Res. Commun.*, vol. 107, p. 103535, 2020.

[48] N. Varble, G. Trylesinski, J. Xiang, K. Snyder, and H. Meng, “Identification of vortex structures in a cohort of 204 intracranial aneurysms,” *J. R. Soc. Interface*, vol. 14, no. 130, 2017.

[49] K. M. Saqr *et al.*, “What does computational fluid dynamics tell us about intracranial aneurysms? A meta-analysis and critical review,” *J. Cereb. Blood Flow Metab.*, vol. 40, no. 5, pp. 1021–1039, 2019.

[50] ANSYS, “ANSYS Fluent theory guide.” Canonsburg, 2015.

[51] H. K. Versteeg and W. Malalasekera, *An Introduction to Computational Fluid Dynamics*, vol. 2. 2007.

[52] A. Y. Usmani and K. Muralidhar, "Flow in an intracranial aneurysm model: effect of parent artery orientation," *J. Vis.*, vol. 21, no. 5, pp. 795–818, 2018.

[53] M. O. Khan and D. A. S. K. V. Sendstad, "Non - Newtonian versus numerical rheology : Practical impact of shear - thinning on the prediction of stable and unstable flows in intracranial aneurysms," no. September 2016, pp. 1–10, 2017.

[54] L. Campo-Deaño, R. P. A. Dullens, D. G. A. L. Aarts, F. T. Pinho, and M. S. N. Oliveira, "Viscoelasticity of blood and viscoelastic blood analogues for use in polydymethylsiloxane in vitro models of the circulatory system," *Biomicrofluidics*, vol. 7, no. 3, 2013.

[55] L. Campo-Deano, M. S. N. Oliveira, and F. T. Pinho, "A review of computational hemodynamics in middle cerebral aneurysms and rheological models for blood flow," *Appl. Mech. Rev.*, vol. 67, no. 3, pp. 1–16, 2015.

[56] M. D. Abràmofff, P. J. Magalhães, and S. J. Ram, "Image processing with ImageJ," *Biophotonics Int.*, vol. 11, no. 7, pp. 36–43, 2005.

[57] J. F. F. Cameron Tropea and A. L. Yarin, *Springer Handbook of Experimental Fluid Mechanics*. 2007.

[58] O. Amili, J. Golzarian, and F. Coletti, "In Vitro Study of Particle Transport in Successively Bifurcating Vessels," *Ann. Biomed. Eng.*, vol. 47, no. 11, pp. 2271–2283, 2019.

[59] A. Ostadfar, *Biofluid Mechanics Principles and Applications*. London: Elsevier, 2016.

[60] J. R. Cebral, F. Mut, J. Weir, and C. M. Putman, "Association of hemodynamic characteristics and cerebral aneurysm rupture," *Am. J. Neuroradiol.*, vol. 32, no. 2, pp. 264–270, 2011.

Chapter 6

Conclusion and Future Directions

6.1 Conclusions

In this work was studied, experimentally and numerically, the hemodynamic of blood analogues in intracranial aneurysms (IA). To achieve this goal was proposed and manufactured IA biomodels, from medical images, using low cost materials and implemented fluid flow numerical simulations in models of real aneurysms.

To choose the most adequate material was determined the mechanical properties of the used material. From the literature knows that the blood vessel had hyperelastic behavior, so, the material of the biomodel must have similar properties, for this reason was chosen the PDMS. On the other hand, many studies had demonstrated the importance of shear stress on the blood vessel walls, therefore, was characterized the shear strain on PDMS. This characterization was realized using two different approaches, numerical and experimental, and was verified the importance of the wall thickness in the shear stress strength. In this study was also determined the most accurate hyperelastic numerical model that could be used to simulate the PDMS deformation which is the Mooney-Rivlin.

To manufacture the biomodels was used the lost core technique with low-cost materials. The real model of IA used to manufacture the PDMS biomodel was obtained from an angiographic medical image acquired in the hospital, then images were segmented with an image processing software and a digital model of the aneurysm in STL format was obtained. This STL file was sent for prototyping stereolithography and a resin model was built. A bipartite silicone mold was produced using this model. The mold was used as cavity for three lost core materials: paraffin, beeswax and glycerin-based soap, which were destroyed at the end of the process. The obtained biomodels were evaluated by their optical transparency, geometry and dimensions. The used materials, beeswax and glycerine-based soap were removed manually and in water at room temperature, respectively, reproducing biomodels with optimum optical characteristics and no residues, however, the biomodels produced using the paraffin have low optical transparency at room temperature. All the lost core materials show an adequate geometrical replication from the DICOM images and the average relative error of the main dimensions are less than 7%.

Were tested different fluids with rheological properties close to the blood and with a refractive index similar to the material used in the biomodels. The fluid that matches the PDMS refractive index is composed by DMSO at 52% diluted (w / w) in water. To implement the experimental tests which characterize the hemodynamics inside the IA was developed an experimental configuration to visualize the high-speed flow. This set-up is composed by pressurized tank connected to the lab pneumatic net. The air pressure inside the tank was regulated by a check valve and a manometer. The tank was connected to a vacuum flask filled with the particles-liquid mixture. A magnetic stirrer operated continuously to prevent the particle settle during the experiments. The mixture flow rate leaving the flask was controlled by a hydraulic speed control valve connected to the flask output. Then, the mixture circulated to the aneurysm model and the flow rate could be controlled by two hydraulic speed control valves installed far away from the artery outlets and two beakers placed over two weighing scales. A set of digital images of the particles inside the model set of frames for each video was processed with the software ImageJ were recorded at 7000 frames per second using an ultra-high-speed CMOS camera. The images obtained were processed to obtain the trajectories which allowed to validate qualitatively the 3D flow behaviour. The developed PDMS biomodels were able to mimic the real artery geometry and could be easily replicated with high enough transparency to perform flow visualization studies. The flow measurements performed with the biomodel were in good agreement with CFD numerical simulations. Hence, this work shows that the proposed biomodels have the potential to be used as *in vitro* models to study complex hemodynamics phenomena happening in different kinds of pathologies such as aneurysms and stenotic blood vessels.

The work developed int this dissertation resulted in a list of publications that are presented in the Appendix A.

6.2 Future Directions

Established low-cost, semi-rigid and flexible biomodel manufacturing techniques, with good reproducibility. It will be possible to develop a new generation of *in vitro* models with the ability to measure, not only the fluid flow, but also wall deformability by the integration of sensors within the PDMS model. Evaluate the efficiency of these models through experimental and numerical tests. Improve the understanding regarding

the interaction of the fluid-structure, as the research about this topic still scarce and there is a lot of controversy in the scientific community about the influence of wall shear stress and pressure on the deformability vessel wall. Thus, the new generation of biomodels proposed in future works are intended to be applied in the research community and in training of young medical doctors, treatment diagnostics and decrease the price of tests for the development of new devices such as stents.

Appendix A

List of Publications

The development of this dissertation resulted in: book chapters, publications in indexed journals, publications in international journals, publications in national and international conferences and oral communications.

Book Chapters

A. Souza et al. “Manufacturing process of a brain aneurysm biomodel in PDMS using rapid prototyping”. VipIMAGE 2019. Lecture Notes in Computational Vision and Biomechanics, vol 34. Springer, Cham.

A. Souza et al. “Numerical Characterization of a Hyperelastic Material to Shear Stress”. VipIMAGE 2019. Lecture Notes in Computational Vision and Biomechanics, vol 34. Springer, Cham.

Publications in Indexed Journals

A. Souza et al. “3D Manufacturing of intracranial aneurysm biomodels for flow visualizations: low cost fabrication processes”. Journal Mechanics Research Communications vol. 107, 2020, 103535.

A. Souza et al. “Characterization of Shear Strain on PDMS: Numerical and Experimental Approaches”. Applied Sciences, 2020, *10*(9), 3322.

V. Carvalho and A. Souza et al. “In vitro stenotic arteries to perform blood analogues flow visualizations and measurements: A Review”. Paper under review in The Open Biomedical Engineering Journal.

Publications in International Journals

A. Souza et al. “Study of PDMS characterization and its applications in biomedicine: A review”. Journal of Mechanical Engineering and Biomechanics, 2019, vol. 4.

Publications in International Conferences

A. Souza et al. “Manufacturing process of a brain aneurysm biomodel in PDMS using rapid prototyping”. VipIMAGE 2019. Lecture Notes in Computational Vision and Biomechanics, vol 34. Springer, Cham.

A. Souza et al. “Numerical Characterization of a Hyperelastic Material to Shear Stress”. VipIMAGE 2019. Lecture Notes in Computational Vision and Biomechanics, vol 34. Springer, Cham.

Oral Communications

A. Souza et al. “Manufacturing process of a brain aneurysm biomodel in PDMS using rapid prototyping”. VipIMAGE 2019. Lecture Notes in Computational Vision and Biomechanics, vol 34. Springer, Cham.

A. Souza et al. “Numerical Characterization of a Hyperelastic Material to Shear Stress”. VipIMAGE 2019. Lecture Notes in Computational Vision and Biomechanics, vol 34. Springer, Cham.

A. Souza and J. Ribeiro. “Estudo do PDMS aplicado em aneurisma cerebrais”. 2ª Escola de Verão & Simpósio de Dupla Diplomação DD2019. 2019.